Reionization era bright emission line survey: selection and characterization of luminous interstellar medium reservoirs in the z > 6.5 universe

Bouwens, R.J.; Smit, R.; Schouws, S.T.M.; Stefanon, M.; Bowler, R.; Endsley, R.; ... ; Witstok, J.

The Astrophysical Journal, 931:160 (28pp), 2022 June 1 https://doi.org/10.3847/1538-4357/ac5a4a

Reionization Era Bright Emission Line Survey: Selection and Characterization of Luminous Interstellar Medium Reservoirs in the $z > 6.5$ Universe

R. J. Bouwens[1], R. Smit[2], S. Schouws[1], M. Stefanon[1], R. Bowler[3], R. Endsley[4], V. Gonzalez[5,6], H. Inami[7], D. Stark[4], P. Oesch[8,9], J. Hodge[1], M. Aravena[10], E. da Cunha[11], P. Dayal[12], I. de Looze[13,14], A. Ferrara[15], Y. Fudamoto[16,17], L. Graziani[18,19], C. Li[20,21], T. Nanayakkara[22], A. Pallottini[15], R. Schneider[18,23], L. Sommovigo[15], M. Topping[4], P. van der Werf[1], H. Algera[7,17], L. Barrufet[8], A. Hygate[1], I. Labbé[22], D. Riechers[24], and J. Witstok[25,26]

[1] Leiden Observatory, Leiden University, NL-2300 RA Leiden, The Netherlands
[2] Astrophysics Research Institute, Liverpool John Moores University, 146 Brownlow Hill, Liverpool L3 5RF, UK
[3] Astrophysics, The Denys Wilkinson Building, University of Oxford, Keble Road, Oxford, OX1 3RH, UK
[4] Steward Observatory, University of Arizona, 933 N Cherry Avenue, Tucson, AZ 85721, USA
[5] Departmento de Astronomia, Universidad de Chile, Casilla 36-D, Santiago 7591245, Chile
[6] Centro de Astrofisica y Tecnologias Afines (CATA), Camino del Observatorio 1515, Las Condes, Santiago, 7591245, Chile
[7] Hiroshima Astrophysical Science Center, Hiroshima University, 1-3-1 Kagamiyama, Higashi-Hiroshima, Hiroshima 739-8526, Japan
[8] Observatoire de Genève, 1290 Versoix, Switzerland
[9] Cosmic Dawn Center (DAWN), Niels Bohr Institute, University of Copenhagen, Jagtvej 128, Kø benhavn N, DK-2200, Denmark
[10] Nucleo de Astronomia, Facultad de Ingenieria y Ciencias, Universidad Diego Portales, Av. Ejercito 441, Santiago, Chile
[11] International Centre for Radio Astronomy Research, University of Western Australia, 35 Stirling Hwy, Crawley,26WA 6009, Australia
[12] Kapteyn Astronomical Institute, University of Groningen, PO Box 800, NL-9700 AV Groningen, The Netherlands
[13] Sterrenkundig Observatorium, Ghent University, Krijgslaan 281—S9, B-9000 Gent, Belgium
[14] Dept. of Physics & Astronomy, University College London, Gower Street, London WC1E 6BT, UK
[15] Scuola Normale Superiore, Piazza dei Cavalieri 7, I-56126 Pisa, Italy
[16] Research Institute for Science and Engineering, Waseda University, 3-4-1 Okubo, Shinjuku, Tokyo 169-8555, Japan
[17] National Astronomical Observatory of Japan, 2-21-1, Osawa, Mitaka, Tokyo, Japan
[18] Dipartimento di Fisica, Sapienza, Universita di Roma, Piazzale Aldo Moro 5, I-00185 Roma, Italy
[19] INAF/Osservatorio Astrofisico di Arcetri, Largo E. Fermi 5, I-50125 Firenze, Italy
[20] Department of Astronomy & Astrophysics, The Pennsylvania State University, 525 Davey Lab, University Park, PA 16802, USA
[21] Institute for Gravitation and the Cosmos, The Pennsylvania State University, University Park, PA 16802, USA
[22] Centre for Astrophysics & Supercomputing, Swinburne University of Technology, PO Box 218, Hawthorn, VIC 3112, Australia
[23] INAF/Osservatorio Astronomico di Roma, via Frascati 33, I-00078 Monte Porzio Catone, Roma, Italy
[24] Cornell University, 220 Space Sciences Building, Ithaca, NY 14853, USA
[25] Kavli Institute for Cosmology, Cambridge, University of Cambridge, Madingley Road, Cambridge, CB3 0HA, UK
[26] Cavendish Laboratory, University of Cambridge, 19 JJ Thomson Avenue, Cambridge CB3 0HE, UK
Received 2021 June 25; revised 2022 February 12; accepted 2022 March 1; published 2022 June 7

Abstract

The Reionization Era Bright Emission Line Survey (REBELS) is a cycle-7 ALMA Large Program (LP) that is identifying and performing a first characterization of many of the most luminous star-forming galaxies known in the $z > 6.5$ universe. REBELS is providing this probe by systematically scanning 40 of the brightest UV-selected galaxies identified over a 7 deg^2 area for bright [C II]$_{158\ \mu m}$ and [O III]$_{88\ \mu m}$ lines and dust-continuum emission. Selection of the 40 REBELS targets was done by combining our own and other photometric selections, each of which is subject to extensive vetting using three completely independent sets of photometry and template-fitting codes. Building on the observational strategy deployed in two pilot programs, we are increasing the number of massive interstellar medium (ISM) reservoirs known at $z > 6.5$ by ~4–5× to >30. In this manuscript, we motivate the observational strategy deployed in the REBELS program and present initial results. Based on the first-year observations, 18 highly significant $\geqslant 7\sigma$ [C II]$_{158\ \mu m}$ lines have already been discovered, the bulk of which (13/18) also show $\geqslant 3.3\sigma$ dust-continuum emission. These newly discovered lines more than triple the number of bright ISM-cooling lines known in the $z > 6.5$ universe, such that the number of ALMA-derived redshifts at $z > 6.5$ rival Lyα discoveries. An analysis of the completeness of our search results versus star formation rate (SFR) suggests an ~79% efficiency in scanning for [C II]$_{158\ \mu m}$ when the SFR$_{UV+IR}$ is >28 $M_\odot$ yr^{-1}. These new LP results further demonstrate ALMA's efficiency as a "redshift machine," particularly in the Epoch of Reionization.

Unified Astronomy Thesaurus concepts: High-redshift galaxies (734); Dust continuum emission (412); Far infrared astronomy (529); Far infrared interferometry (528)

1. Introduction

The first galaxies are thought to have started forming in the first 200–300 Myr of the universe (Bromm & Yoshida 2011; Wise et al. 2012) and then rapidly built up their stellar mass. With existing telescopes, it has been possible to obtain a glimpse of galaxies forming close to this time (e.g., Zheng et al. 2012; Ellis et al. 2013; Oesch et al. 2014; Bouwens et al. 2015, 2016; Bowler et al. 2015; Finkelstein et al. 2015; Stefanon et al. 2017a; Dayal & Ferrara 2018; Ono et al. 2018), with galaxies identified as far back as $z \sim 11$ (e.g., Coe et al. 2013; Oesch et al. 2016), ~400 Myr after the Big Bang.

The discovery of impressively massive galaxies in the first 1–2 billion years of the universe, including an especially massive $2 \times 10^{11}\ M_{\odot}$ passive galaxy at z = 3.717 (Glazebrook et al. 2017), a $\sim 3 \times 10^{11}\ M_{\odot}$ star-forming galaxy at $z = 6.9$ (Strandet et al. 2017; Marrone et al. 2018), a $z = 7.54$ quasar with a supermassive black hole of mass $8 \times 10^{8}\ M_{\odot}$ (Bañados et al. 2018), and even a $10^{9}\ M_{\odot}$ galaxy at $z \sim 11$ (Oesch et al. 2016; Jiang et al. 2021), have reignited long-standing questions about how rapidly galaxies could have begun forming large numbers of stars. Besides these few well-known examples of $z > 3$ galaxies with particularly high masses (and other work by, e.g., Díaz-Santos et al. 2016 and Tanaka et al. 2019), other evidence for significant early star formation includes a few $z > 6$ galaxies with apparently older stellar populations (e.g., Hashimoto et al. 2018; Roberts-Borsani et al. 2020) and evidence for lower-mass $z \sim 4$–8 galaxies with elevated stellar-mass-to-halo-mass ratios (e.g., Behroozi et al. 2013).

Until just recently, the only physical information we had on the early epochs of star formation for most massive galaxies is from sensitive near-IR observations from Hubble Space Telescope (HST), mid-IR observations from Spitzer, and some rest-UV spectroscopy from the ground. HST provides us with high spatial resolution images revealing newly formed stars not obscured by dust, while Spitzer probes line emission and the stellar population age in galaxies through features like the Balmer break. Quantifying the masses in $z > 6$ galaxies has proven to be particularly challenging due to the limited information in Spitzer/IRAC imaging observations and degeneracy between the impact of older stellar populations and strong nebular emission lines (e.g., Schaerer & de Barros 2009; Raiter et al. 2010; Roberts-Borsani et al. 2020). Rest-UV spectroscopy has resulted in the detection of Lyα and some high-ionization UV lines in select $z > 6$ galaxies (e.g., Zitrin et al. 2015; Stark et al. 2017), suggestive of very young stellar populations with moderately hard radiation fields (Stark et al. 2015; Mainali et al. 2017; Schmidt et al. 2017; Mainali et al. 2018; Hutchison et al. 2019). While such radiation fields are likely important in driving the reionization of the universe at $z > 6$, determining the typical stellar population properties of $z > 6$ galaxies has remained very challenging.

Fortunately, thanks to the improving capabilities of the Atacama Large Millimeter Array (ALMA), we can make significant progress characterizing the physical properties of massive star-forming sources in the early universe (e.g., Hodge & da Cunha 2020). ALMA efficiently allows for a probe of the redshift and dynamical state of galaxies in the reionization epoch using bright interstellar medium (ISM)-cooling lines like 157.74 μm [C II] and 88.36 μm [O III] (e.g., Smit et al. 2018; Hashimoto et al. 2019; Tamura et al. 2019; Jones et al. 2021), while simultaneously probing the far-IR dust-continuum radiation (e.g., Capak et al. 2015; Bowler et al. 2018; Fudamoto et al. 2020; Schouws et al. 2022a). This provides us with an essential measure of the star formation in galaxies obscured by dust. The effectiveness of ALMA in probing the physical properties of galaxies has been demonstrated by a few particularly noteworthy observational programs with ALMA, e.g., the ASPECS ALMA Large Program in cycle 4 probing the dust and gas in $z > 0.5$ galaxies over the Hubble Ultra Deep Field (e.g., Aravena et al. 2020; Bouwens et al. 2020; Decarli et al. 2020; González-López et al. 2020; Walter et al. 2020) and the ALPINE ALMA Large Program in cycle 5 targeting >110 $z = 4$–6 sources (Béthermin et al. 2020; Faisst et al. 2020; Le Fevre et al. 2020). By contrast, the number of sources in the reionization epoch that have been characterized in detail with ALMA has been modest (e.g., Maiolino et al. 2015; Watson et al. 2015; Inoue et al. 2016; Pentericci et al. 2016; Knudsen et al. 2017; Laporte et al. 2017, 2019; Matthee et al. 2017, 2019; Hashimoto et al. 2018, 2019; Smit et al. 2018; Tamura et al. 2019; Bakx et al. 2020; Schouws et al. 2022a).

Until recently, the ALMA view of galaxies in the $z > 6$ universe has been restricted to those galaxies that show prominent Lyα emission, whether these sources be QSOs (e.g., Venemans et al. 2019, 2020) or simply massive star-forming galaxies, e.g., B14-65666 at $z = 7.15$ (Bowler et al. 2018; Hashimoto et al. 2019) or CR7 at $z = 6.59$ (Matthee et al. 2017). This is especially a concern for more massive galaxies ($\gtrsim 10^{9}\ M_{\odot}$), which frequently do not show Lyα in emission at all (e.g., Stark et al. 2010; Schenker et al. 2014; Pentericci et al. 2018; Jung et al. 2020; Endsley et al. 2021b), giving us a potentially biased view of the characteristics of luminous galaxies at early times. Given such, it is clearly desirable for us to have an alternate strategy of selecting massive galaxies in the $z > 6$ universe.

Recently, it has been shown that scanning UV-bright galaxies for prominent ISM-cooling lines like $[\mathrm{C\,II}]_{158\ \mu\mathrm{m}}$ or $[\mathrm{O\,III}]_{88\ \mu\mathrm{m}}$ can be a very efficient way to identify luminous galaxies in the $z > 6$ universe. This strategy appears to be most efficient (1) when targets are especially UV bright and (2) when the redshift of targets is particularly well-constrained, e.g., from the position of the Lyman break or the position of strong nebular emission lines within the Spitzer/IRAC bands (Smit et al. 2015). Smit et al. (2018) used just an hour of ALMA observations to identify what were then two of the most luminous $[\mathrm{C\,II}]_{158\ \mu\mathrm{m}}$ lines known at $z > 6.5$. Employing a similar spectral scan strategy to observe six more luminous $z \sim 7$ galaxies with well-constrained redshifts, Schouws et al. (2022b) found bright $[\mathrm{C\,II}]_{158\ \mu\mathrm{m}}$ lines in three more $z \sim 7$ galaxies with an 11 hr program (2018.1.00085.S). The Smit et al. (2018) and Schouws et al. (2022b) programs demonstrated how effective ALMA could be in scanning for extremely bright $[\mathrm{C\,II}]_{158\ \mu\mathrm{m}}$ lines in UV-bright sources at $z > 6.5$, and they effectively served as pilots for the ALMA Large Program we introduce here.

In parallel with these $[\mathrm{C\,II}]_{158\ \mu\mathrm{m}}$ studies, there were simultaneous efforts exploring the use of the $[\mathrm{O\,III}]_{88\ \mu\mathrm{m}}$ line for spectral scans at $z > 8$, taking advantage of both the brightness of the line and its greater accessibility in band 7 at $z > 8$. The first detection of the $[\mathrm{O\,III}]_{88\ \mu\mathrm{m}}$ line in the $z > 7$ universe was by Inoue et al. (2016) at $z = 7.21$ in a Lyα-emitting galaxy. Hashimoto et al. (2018) then demonstrated the first successful scan for $[\mathrm{O\,III}]_{88\ \mu\mathrm{m}}$ at $z > 8$, securing a 7.4σ detection of line in the $z = 9.1096 \pm 0.0006$ source MACS1149-JD (Zheng et al. 2012). Tamura et al. (2019) similarly made use of ALMA to successfully scan for the $[\mathrm{O\,III}]_{88\ \mu\mathrm{m}}$ line in a magnified Lyman-break galaxy behind MACS0416, MACS0416_Y1, finding a redshift of 8.3118 ± 0.0003 based on a 6.3σ detection.

With multiple ALMA programs demonstrating the feasibility of using spectral scans to search for especially luminous ISM reservoirs at $z > 6.5$, the necessary preparatory work had been done to consider executing a much more significant survey program with ALMA for luminous ISM reservoirs in the $z > 6.5$ universe. It was in this environment that the Reionization Era Bright Emission Line Survey (REBELS) program (2019.1.01634.L) was approved for execution in cycle 7 as an

extragalactic ALMA Large Program. The goal of the REBELS program is to create the first significant sample of especially luminous ISM reservoirs in the Reionization Epoch. REBELS is doing so by scanning for bright ISM-cooling lines on a large sample of UV-bright ($-23.0 < M_{\rm UV,AB} <= 21.5$) galaxies at $z > 6.5$, while simultaneously probing the dust-continuum flux of sources.

In this paper, we summarize the observational strategy employed by the REBELS ALMA Large Program and highlight some first results demonstrating the effectiveness of this strategy. This includes an overview of the target selection and major scientific goals. The standard concordance cosmology $\Omega_0 = 0.3$, $\Omega_\Lambda = 0.7$, and $H_0 = 70\,{\rm km\,s^{-1}\,Mpc^{-1}}$ is assumed for consistency with previous studies. SFR and stellar masses are quoted assuming a Chabrier (2003) IMF. All magnitudes are in the AB system (Oke & Gunn 1983).

2. UV-Bright Sample Selection

In this section, we motivate our use of a UV-bright selection for the REBELS ALMA LP, and then discuss procedurally how we identify the most robust set of targets for the program.

Briefly, the REBELS LP selects 40 UV-bright galaxies at $z > 6.5$ for spectral scan observations, drawing from a 7 deg^2 area with the deepest wide-area optical, near-IR, and Spitzer/IRAC imaging observations, and features the 2 deg^2 COSMOS/UltraVISTA field, the 5 deg^2 VIDEO/XMM-LSS + UKIDSS/UDS fields, and an 0.2 deg^2 area composed of various HST legacy fields including CANDELS (Grogin et al. 2011; Koekemoer et al. 2011), CLASH (Postman et al. 2012), RELICS (Coe et al. 2019; Salmon et al. 2020), and various BoRG/HIPPIES pure parallel fields (Trenti et al. 2011; Yan et al. 2011; Bradley et al. 2012; Schmidt et al. 2014; Morishita et al. 2020; Roberts-Borsani et al. 2022). Sources are chosen both because of their UV luminosities (Figure 1) and because of the tight constraints we have on their redshifts from the available imaging data (Figure 2).

Figure 3 illustrates the search fields used for constructing the REBELS sample as well as the distribution of the REBELS targets over the sky. Figure 4 illustrates the distribution of UV luminosities and redshifts for targets in the REBELS program and compares this distribution against those sources in the REBELS pilot programs, in the ALPINE program, galaxies with confirmed Lyα emission at $z > 6.5$, and sources in various HST legacy fields. A complete list of the targets in the program is provided in Table 1.

2.1. Prevalence of Massive Star-forming Galaxies among UV-bright Galaxies at z > 4

Over the last few years, it has become increasingly clear that many of the brightest known ISM-cooling lines at $z \gtrsim 5.5$ are found in especially UV-bright galaxies ($M_{\rm UV,AB} \lesssim -22$ mag: $\geqslant 2\,L^*_{\rm UV}$). Examples include the 10 $z \sim 5.5$ sources targeted by Capak et al. (2015), two $z \sim 6.1$ galaxies targeted by Willott et al. (2015), CR7 by Matthee et al. (2017), B14-65666 by Hashimoto et al. (2019), VR7 by Matthee et al. (2019), and the three $z \sim 6.1$–6.2 galaxies targeted by Harikane et al. (2020). All show bright ($\gtrsim 2$ mJy km s^{-1}) [C II]$_{158\,\mu{\rm m}}$ lines. Meanwhile, follow-up of $z \geqslant 6$ galaxies with redshifts from Lyα have frequently revealed only moderate- to low-luminosity ($\lesssim 1$ mJy km s^{-1}) [C II]$_{158\,\mu{\rm m}}$ lines (Ouchi et al. 2013; Ota et al. 2014; Pentericci et al. 2016; Bradač et al. 2017; Carniani et al. 2018, 2020), strongly suggesting that there may be an inverse correlation between Lyα equivalent width (EW) and the mass of the ISM reservoirs (Figure 18 from Harikane et al. 2020). Given such, it seems the best way to obtain a representative sample of massive galaxies at $z > 6$ is to identify galaxies on the basis of their UV luminosity (rather than Lyα emission alone).

To quantify the relationship between the UV luminosity $M_{\rm UV}$ of galaxies and their $L_{\rm [C\,II]_{158\,\mu m}}$, we present a compilation of some recent results at $z > 4$ (Capak et al. 2015; Smit et al. 2018; Matthee et al. 2019; Béthermin et al. 2020; Schouws et al. 2022b) in Figure 1. A conversion factor of $7.1 \times 10^{-29} L_\nu[M_\odot\,{\rm yr^{-1}}/({\rm erg\,s^{-1}\,Hz^{-1}})]$ (M. Stefanon et al. 2022, in preparation) is used to transform the UV luminosities of galaxies into SFRs. What is particularly striking here is the strong correlation we observe between $L_{\rm [C\,II]_{158\,\mu m}}$ and the unobscured SFR$_{\rm UV}$, with a particularly clear correlation around 10 $M_\odot\,{\rm yr^{-1}}$. The fraction of sources with [C II]$_{158\,\mu{\rm m}}$ luminosities in excess of $2 \times 10^8 L_\odot$, the typical sensitivity limit achieved in REBELS observations, increases from 35% at 10 $M_\odot\,{\rm yr^{-1}}$ to 80% at 20 $M_\odot\,{\rm yr^{-1}}$.

Because of the strong correlation between $L_{\rm [C\,II]_{158\,\mu m}}$ and $M_{\rm UV}$, one can very efficiently derive redshifts for galaxies that are bright in the UV by scanning for the [C II]$_{158\,\mu{\rm m}}$ ISM-cooling line with ALMA, as demonstrated in the introduction by both pilot programs to REBELS (Smit et al. 2018; Schouws et al. 2022b).

2.2. Search Fields

In constructing a sample of 40 UV-bright galaxies to follow up with the REBELS LP, we made use of deep wide-area optical + near-IR observations over the $\sim$2 deg^2 COSMOS/UltraVISTA field (Scoville et al. 2007; McCracken et al. 2012), the $\sim$5 deg^2 UKIDSS/UDS + VIDEO/XMM-LSS fields (Lawrence et al. 2007), and a wide range of HST search fields, including CANDELS, CLASH, and the BoRG/HIPPIES pure parallel fields.

A significant fraction of the UV-bright targets for REBELS are drawn from the $\sim$2 deg^2 COSMOS/UltraVISTA field. In constructing our source catalogs for this field, we made use of the very sensitive Y, J, H, and K_s near-IR observations (both data release 3 and 4) from the UltraVISTA program (McCracken et al. 2012), the deep optical Subaru Suprime-Cam *BgVriz* observations from Taniguchi et al. (2005), the deep optical *ugriyz* observations from the CFHT Deep Legacy survey (Erben et al. 2009; Hildebrandt et al. 2009), and the *ugrizy* Subaru Hyper Suprime-Cam (HSC) observations (Aihara et al. 2018b, 2018a). Use of the Spitzer/IRAC 3.6 μm and 4.5 μm observations from SCOSMOS (Sanders et al. 2007), Spitzer Large-Area Survey with HSC (SPLASH: Steinhardt et al. 2014), SMUVS (Caputi et al. 2017; Ashby et al. 2018), COMPLETE (Labbé et al. 2016), and COMPLETE2 (Stefanon et al. 2018) programs were also made.

The bulk of the remaining targets are drawn from the $\sim$5 deg^2 UKIDSS/UDS and VIDEO/XMM-LSS area. The UDS/XMM-LSS area includes sensitive near-IR observations from both the UKIDSS/UDS (Lawrence et al. 2007; J, H, and K bands) and VISTA Deep Extragalactic Observations (VIDEO) programs (Jarvis et al. 2013; Y, J, H, and K_s), sensitive optical observations from the Subaru Hyper Suprime-Cam deep and wide-area programs (Aihara et al. 2018a, 2018b), and Spitzer/IRAC observations from the SPLASH and Spitzer Extragalactic

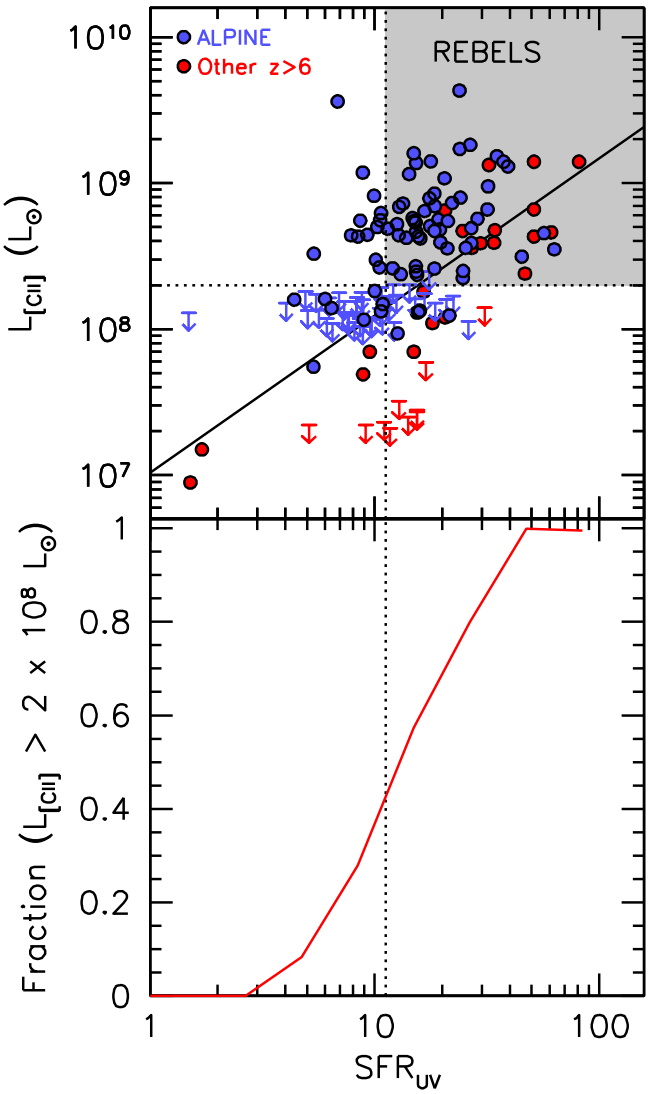

Figure 1. (upper) Observed luminosity of the $[C\,II]_{158\,\mu m}$ cooling line seen in galaxies at $z \sim 6$–7 versus the observed star formation rate of galaxies in the rest-UV. The plotted results are drawn from the ALPINE (Béthermin et al. 2020; Le Fevre et al. 2020; Faisst et al. 2020) and Capak et al. (2015) $z = 4$–6 samples (blue circles) as well as the REBELS pilots (Smit et al. 2018; Schouws et al. 2022b) and other $z > 6$ sources (red circles: Matthee et al. 2019). The black solid line shows the $z \sim 0$ $[C\,II]_{158\,\mu m}$–SFR_{UV+IR} De Looze et al. (2014) relation. Particularly noteworthy is the increase in the $[C\,II]_{158\,\mu m}$ luminosities of galaxies as rest-UV SFRs increase from 5 to 30 $M_\odot$ yr^{-1}. REBELS only includes sources with rest-UV SFRs in excess of 11 $M_\odot$ yr^{-1} (dotted vertical line). The horizontal dotted line shows the approximate 5σ sensitivity limit adopted in the REBELS program. (lower) The fraction of galaxies with $[C\,II]_{158\,\mu m}$ luminosities in excess of 2×10^8 $L_\odot$ (the typical sensitivity limit for observations taken as part of REBELS) versus the unobscured SFR of galaxies at $z > 6$. A significant fraction of galaxies with rest-UV SFRs in excess of 10 $M_\odot$ yr^{-1} and especially 20 $M_\odot$ yr^{-1} have $[C\,II]_{158\,\mu m}$ luminosities in excess of 2×10^8 $L_\odot$ (Section 2.1). It is these high SFR sources at $z > 6.5$ that the REBELS large program particularly targets in scanning for bright ISM-cooling lines.

Representative Volume Survey (SERVS; Mauduit et al. 2012) programs.

We also considered including UV-bright $z > 6.5$ galaxies from the CANDELS, CLASH, and BoRG/HIPPIES fields as targets in the REBELS program. In total, the CANDELS, CLASH, and BoRG/HIPPIES fields that we used for selecting targets covered an area of 0.2 deg^2 (excluding those HST CANDELS fields within COSMOS and UDS).

2.3. Selection of the Targets for REBELS

From each of these search fields, we considered a range of different catalogs in arriving at our final target list. Here, we provide a brief summary of each sample we consider:

Bowler et al. (2014, 2017) ($z \sim 7$): The Bowler et al. (2014) $z \sim 7$ selection was constructed based on deep z, Y, J, H, and K_s observations obtained over the COSMOS/UltraVISTA and UKIDSS/UDS fields with Subaru Suprime-Cam + VISTA and Subaru, VISTA, and UKIRT, respectively. The deep $Y + J$ and J band images over UltraVISTA/COSMOS and the UKIDSS/UDS fields, respectively, were used as the detection image in constructing source catalogs for the search. Then, after removing all sources detected at 2σ in the optical imaging data, the LEPHARE photometric redshift software (Arnouts et al. 1999; Ilbert et al. 2006) was run, using Bruzual & Charlot (2003) models with a range of exponentially declining star formation histories, metallicities of 0.2 $Z_\odot$ and $Z_\odot$, a range of dust attenuation ($A_V < 4$), Lyα EWs to 240 Å, and Madau (1995) IGM absorption. Then, Bowler et al. (2014) compared their LEPHARE fit results with similar fits to stars from the SpecX library (Burgasser 2014) to identify and exclude any possible low-mass stars from their selection. Bowler et al. (2017) refined the Bowler et al. (2014) selection, taking advantage of subsequent WFC3/IR F140W imaging they obtained over the fields with HST, identifying two additional and fainter $z \sim 7$ galaxies in the neighborhood of their bright candidates and removing three crosstalk artifacts from their catalogs (Section 3.2 of Bowler et al. 2017). In total, 22 bright $z \sim 7$ galaxies were identified as part of the Bowler et al. (2014) and Bowler et al. (2017) studies, with M_{UV} luminosities ranging from -20.7 to -23.2 mag.

Stefanon et al. (2017b, 2019a) ($z \sim 8$–9): The selection of $z \sim 8$–9 galaxies in Stefanon et al. (2017b, 2019a) was performed by first creating a large parent catalog over the COSMOS/UltraVISTA fields based on the Y, J, H, and K_s images and then applying an optical nondetection and two-color Lyman-break galaxy-like criteria. Stefanon et al. (2019a) then made use of the MOPHONGO package (Labbé et al. 2006, 2013, 2015) to do careful optical, near-IR, and Spitzer/IRAC photometry for each source in the parent catalog, modeling and subtracting the flux from nearby neighbors to improve the robustness of the flux measurements. Candidate $z \sim 8$–9 galaxies were then selected by running the EAZY photometric redshift code (Brammer et al. 2008) on the optical +near-IR+Spitzer/IRAC photometry that had been derived. Eighteen $z \sim 8$–9 candidate galaxies were identified by Stefanon et al. (2017b, 2019a) over the ~2 deg^2 COSMOS field. Through similar fits of the source photometry to the SpecX dwarf star spectral libraries (Burgasser 2014), Stefanon et al. (2019a) explicitly verified that all sources were better fit ($\Delta\chi^2 > 1$) by galaxy SED templates than dwarf star templates.

Bowler et al. (2020): Candidate $z \sim 8$–11 galaxies were identified using the very deep ground-based optical and near-IR observations over ~6 deg^2 in the COSMOS/UltraVISTA and VIDEO/XMM-LSS + UKIDSS/UDS fields. Candidate $z \sim 8$ galaxies were required to be detected at 5σ in either than J or H bands, while candidate $z \sim 9$ galaxies were required to show a 5σ detection in either the H or K_s/K bands. No detection ($<2\sigma$) was allowed for sources in any of the deep optical bands, as well as the Y band for $z \sim 9$ candidates. The reality of sources showing 5σ detections in the UDS JHK data was tested by looking for similar 2σ detections in the VISTA data. The

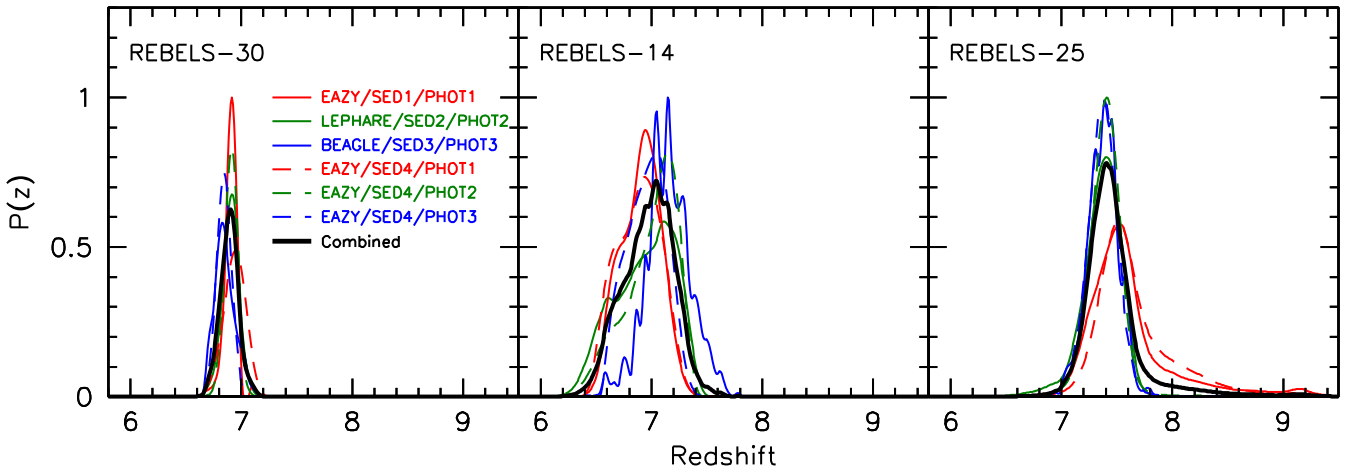

Figure 2. Redshift likelihood distributions derived for three different sources in the REBELS program REBELS-30 (left), REBELS-14 (center), and REBELS-25 (right) by team members Rebecca Bowler, Ryan Endsley, and Mauro Stefanon (shown as the red, green, and blue lines, respectively) by applying the LEPHARE, BEAGLE, and EAZY photometric redshift codes, respectively, to their own independent photometry PHOT1, PHOT2, and PHOT3, respectively. Three additional redshift likelihood distributions have been derived on the basis of each set of photometry by using the EAZY photometric redshift code, and a separate set of SED templates SED4 are shown as the dashed red, green, and blue lines, respectively. The thick black lines show the redshift likelihood distributions derived by averaging the results of the six separate likelihood distributions.

redshift likelihood distributions for candidate $z\sim 8$–11 galaxies were then computed using a range of exponentially declining star formation histories, metallicities of 0.2 $Z_{\odot}$ and $Z_{\odot}$, a range of dust attenuation ($A_V<6$), and the Madau (1995) IGM absorption. Bowler et al. (2020) identified 27 $z\sim 8$–10 galaxies with UV luminosities $M_{\rm UV}$ ranging from −23.7 to −21.2 mag.

Endsley et al. (2021a): Candidate $z\sim 7$ galaxies were identified over the deep ∼2 deg^2 COSMOS/UltraVISTA and ∼1 deg^2 UKIDSS UDS fields. Sources were detected from χ^2 detection images (Szalay et al. 1999) constructed from the deep $yYJHK_s$ HSC/UltraVISTA and $yYJHK$ HSC/VIDEO/UKIDSS imaging observations. Endsley et al. (2021a) then applied the following color criteria: (1) $z-y>1.5$, (2) $z-Y>1.5$, (3) $NB_{921}-Y>1.0$, and (4) $y-Y<0.4$. Sources were required to be detected at 5σ in at least one of the y, Y, and J bands and detected at 3σ in all three and undetected at $<2\sigma$ in the HSC g and r bands. Possible T dwarf contaminants were removed by requiring either $Y-J<0.45$ or both $J-H>0$ and $J-K_s>0$. Endsley et al. (2021a) identified 50 sources over the COSMOS/UltraVISTA and UDS fields.

Schouws et al. (2022b): Candidate $z\sim 7$ galaxies in Schouws et al. (2022b) were selected from the ∼2 deg^2 UltraVISTA observations over the COSMOS field and required to show a $>6\sigma$ detection in a stack of the Y, J, H, and K_s images and a $\chi^2_{\rm opt}<4$ (Bouwens et al. 2011). Best-fit photometric redshifts and redshift likelihood distributions were then derived with EAZY using photometry of sources derived from the available CFHT + Subaru optical imaging data, UltraVISTA $YJHK_s$ near-IR observations, and Spitzer/IRAC observations from SCOSMOS, SPLASH, and SMUVS programs. For inclusion in the Schouws et al. (2022b) $z>6.5$ sample, sources were required to have an integrated $z>6$ probability of >50% and to be better fit by a galaxy SED template than one of the SED templates from the SpecX dwarf star spectral library. Schouws et al. (2022b) identified some 30 bright $z\sim 7$ galaxies as part of their study, with $M_{\rm UV}$ ranging from −23.0 mag to −21.4 mag.

This Paper (see also M. Stefanon et al. 2022, in preparation): Finally, we considered separate selections of $z\sim 7$–8 galaxies drawn from the ∼5 deg^2 VIDEO/XMM-LSS + UKIDSS/UDS fields generated using procedures similar to those described in Stefanon et al. (2019a). The detection was performed on the combination of the J, H, and $K_{\rm S}$ mosaics, either from the UKIDSS/UDS or VIDEO programs. Candidates at $z\sim 7$ were selected through the $z-Y>0.7$ mag and $\langle YJ\rangle-\langle JH\rangle<0.5$ mag color criteria, where $\langle..\rangle$ denotes the average flux density in the two indicated bands. To identify the samples at $z\sim 8$, we imposed $Y-J>0.7$ mag and $\langle JH\rangle-\langle HK_{\rm S}\rangle<0.5$ mag for $z\sim 8$. These criteria were coupled with the requirement of nondetection ($<2\sigma$) in all bands (CFHTLS, HSC, and SUBARU) bluer than the nominal Lyman break, together with a 5σ detection in the combined J, H, and $K_{\rm S}$ bands, to increase the robustness of the detection. The selection was refined computing the photometric redshifts with EAZY (Brammer et al. 2008), after adding the flux densities in the 3.6μm and 4.5μm Spitzer/IRAC bands from the SWIRE, SpUDS, and SEDS programs. Finally, the image stamps of the candidates were visually inspected, to remove contaminants and sources whose flux measurements are contaminated by poorly subtracted neighbors. Sources with better χ^2 from the templates of Burgasser (2014) were excluded as likely brown dwarf contaminants. This led to the identification of ∼40 candidates at $z\sim 7$ and ∼25 at $z\sim 8$ brighter than $J\sim 25-26$ mag.

We then created a master list of 60 UV-bright $z=6.5$–10 candidates from the above analyses, as well as five other particularly bright $z>6.5$ galaxies that had been identified over various HST legacy fields (MACS0429Z-9372034910, BORG2229-0945-394, Super8-1, Super8-4, and Super8-5; see Bradley et al. 2012; Smit et al. 2014, 2015; Bouwens et al. 2015, 2019, Morishita et al. 2018; Bridge et al. 2019; Salmon et al. 2020). Combining the above analyses, the approximate area probed in the COSMOS/UltraVISTA field, UKIDSS/UDS + VIDEO/XMM-LSS fields, and various HST archival fields (not included in the COSMOS or the UDS fields) is 1.82 deg^2, 4.97 deg^2, and 0.2 deg^2, respectively, or 6.99 deg^2 in total.

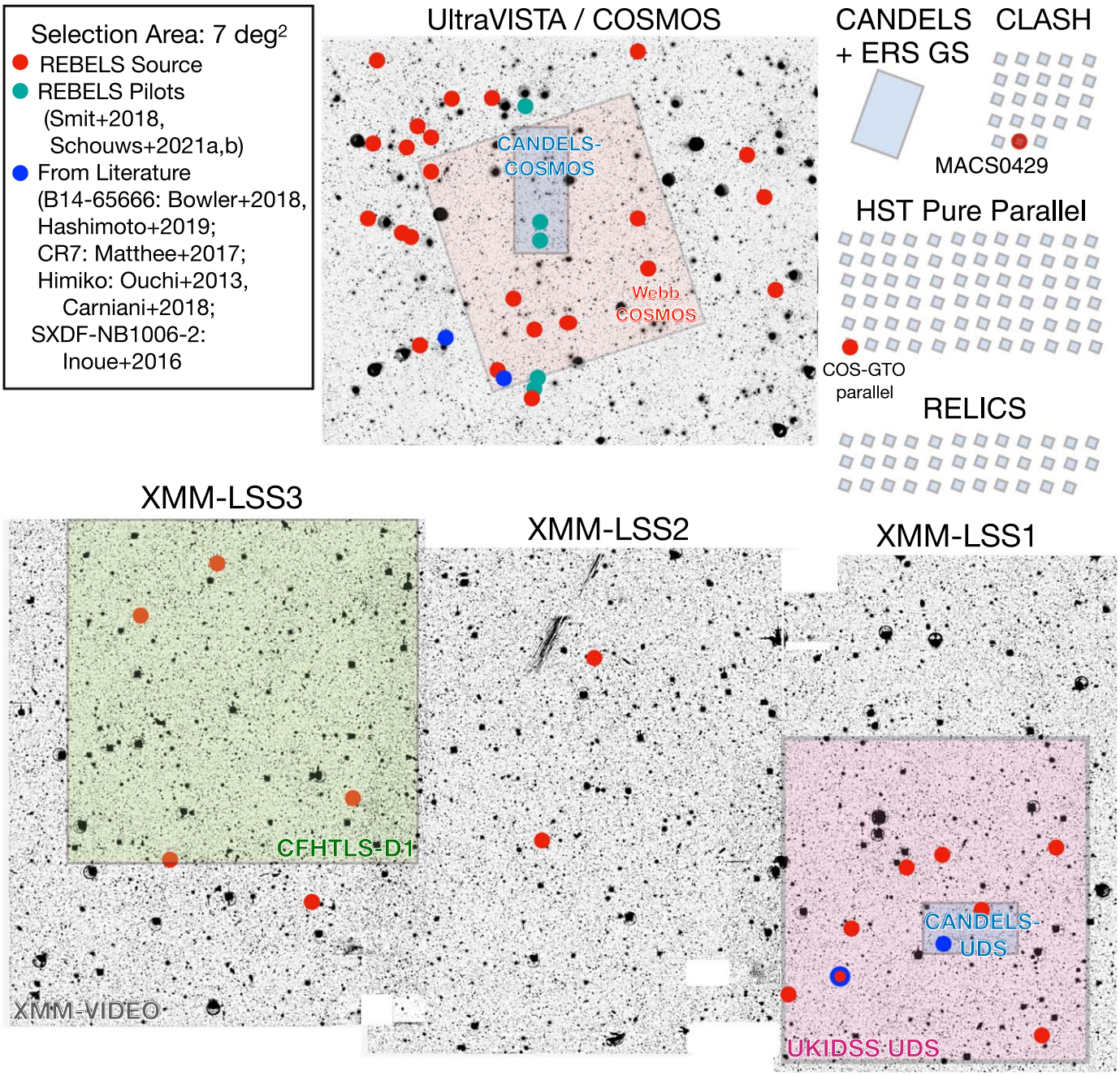

Figure 3. The layout of the two wide-area ground-based fields + HST data sets used to identify $z = 6.5$–9.5 targets for the REBELS ALMA Large Program. The red circles indicate the position of REBELS targets, and the cyan circles indicate the position of targets in the REBELS pilot programs (Smit et al. 2018; Schouws et al. 2022b). The blue circles indicate the position of other sources in the literature that also meet the selection criteria for REBELS but already have substantial ALMA observations (Ouchi et al. 2013; Inoue et al. 2016; Matthee et al. 2017; Bowler et al. 2018; Carniani et al. 2018; Hashimoto et al. 2019). Also shown is the array of individual HST fields considered in the selection of targets for REBELS, including CANDELS GOODS South (Grogin et al. 2011), CLASH (Postman et al. 2012), various pure parallel fields (e.g., Morishita et al. 2018; Bridge et al. 2019), and RELICS (Coe et al. 2019). The position of the CANDELS COSMOS and CANDELS UDS fields within the COSMOS/UltraVISTA and UDS/XMM-LSS fields is indicated. The planned layout of the Webb-COSMOS survey (Kartaltepe et al. 2021) is also included on this figure.

For each of the 60 candidates identified over the UltraVISTA/COSMOS, VIDEO/XMM-LSS, and UKIDSS/UDS fields, measurements of the optical, near-IR, and Spitzer/IRAC fluxes were made by three members of our team (Mauro Stefanon, Rebecca Bowler, and Ryan Endsley) applying their own photometric procedures to the imaging data sets each had compiled of the fields. We refer to these flux measurements as PHOT1, PHOT2, and PHOT3, respectively. Very briefly, PHOT1 is based on neighbor-subtracted aperture photometry of sources in 1.″2 diameter and 1.″8 diameter apertures in the optical/near-IR and Spitzer/IRAC data using MOPHONGO (e.g., see Stefanon et al. 2019a), PHOT2 is based on aperture photometry in 1.″8 diameter apertures and neighbor-subtracted aperture photometry in 2.″8 diameter apertures with T-PHOT (Merlin et al. 2015) for the optical/near-IR and Spitzer/IRAC data, respectively (see, e.g., Bowler et al. 2020), and PHOT3 is based on 1.″2 diameter aperture photometry for the optical/near-IR data, and in 2.″8 diameter apertures after subtracting

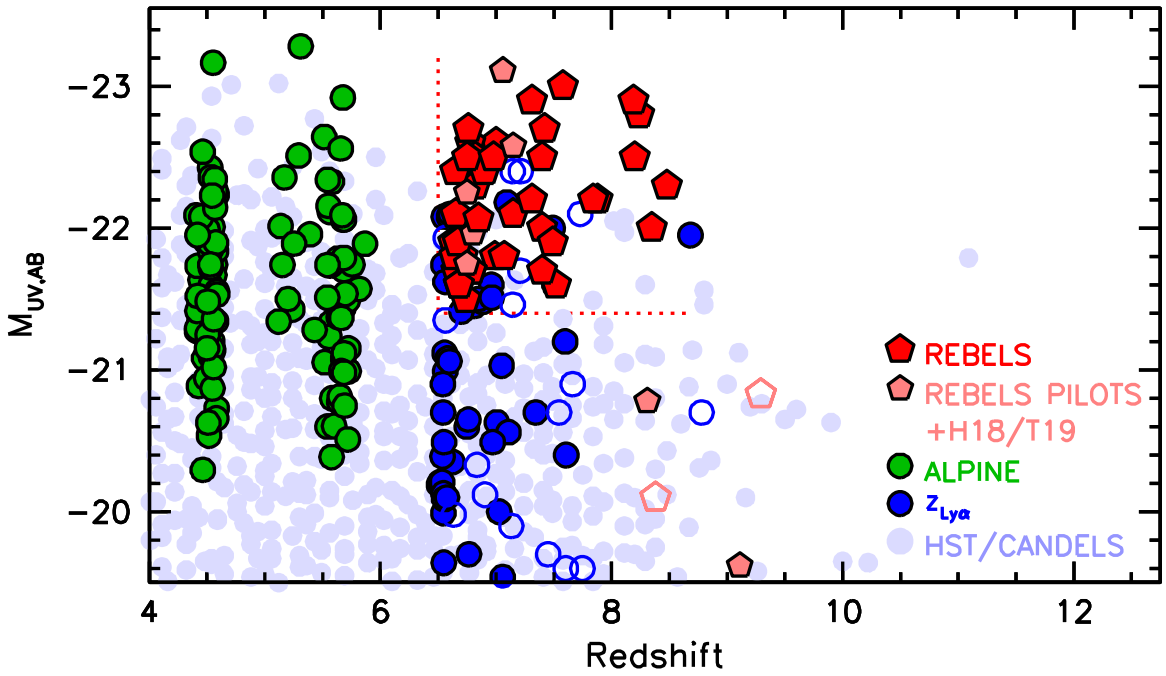

Figure 4. UV luminosities and photometric redshifts of the new sample of bright $z > 6.5$ galaxies (red pentagons) being targeted with the REBELS ALMA Large program relative to $z > 6.5$ sources with spectroscopic redshifts from Lyα (dark blue circles), $z > 6.5$ sources from pilots to REBELS (light red pentagons), sources over various HST legacy fields (Bouwens et al. 2021; light blue circles), and sources with the ALPINE program (green circles). The $z > 6.5$ sources with redshift determinations based on Lyα and [O III]$_{88\ \mu m}$ lines where the significance is $<7\sigma$ are shown with open blue circles and open light red pentagons, respectively.

neighbors using a MOPHONGO/T-PHOT-like algorithm (see Endsley et al. 2021a). For each of these photometric catalogs, aperture measurements are corrected to total based on the curve of growth. More details on these photometric procedures will be provided in M. Stefanon et al. (2022, in preparation). For sources found within various HST legacy fields, use was made of published photometry, except in the case of the Super8 sources where deeper IRAC imaging observations (Holwerda et al. 2018) were utilized.

Each team member doing photometry (M.S., R.B., and R.E.) then made use of a separate photometric redshift code (EAZY, LEPHARE, and BEAGLE [Chevallard & Charlot 2016], respectively) to derive a redshift likelihood distribution for each candidate on the basis of their photometry (PHOT1, PHOT2, and PHOT3, respectively). A fourth member of the REBELS team (Rychard Bouwens) then derived a fourth, fifth, and sixth photometric redshift distribution for each source by running the EAZY photometric redshift code a second time on the photometry derived by R.B., R.E., and M.S., but using a different set of SED templates SED4. In particular, instead of using the EAZY_v1.0 template set augmented by the Binary Population and Spectral Synthesis code (BPASS; Eldridge et al. 2017) v1.1 for subsolar metallicity ($Z = 0.2Z_{\odot}$), which include nebular emission from CLOUDY (Ferland et al. 2017), and 2Gyr old passively evolving systems with varying amounts ($A_V = 0$–8 mag) of dust extinction adopting the Calzetti et al. (2000) law, i.e., SED template set SED1, the second EAZY runs use the EAZY_v1.0 template set augmented by SED templates from the Galaxy Evolutionary Synthesis Models (GALEV; Kotulla et al. 2009), i.e., SED template set SED4. Nebular continuum and emission lines were included in the latter templates according to the prescription provided in Anders & Fritze-v. Alvensleben (2003), a $0.2Z_{\odot}$ metallicity, and scaled to a rest-frame EW for Hα of 1300 Å.

The mean of the six redshift likelihood distributions was then taken and a single distribution derived (Figure 2). Care was taken to explicitly verify that none of the candidates considered resulted from the VISTA/VIRCAM electronic crosstalk artifact Bowler et al. (2017) identified. Bowler et al. (2017) found that such artifacts occurred at multiples of 128 pixel separations from saturated stars in the VISTA/VIRCAM data. Similar crosstalk artifacts are known to occur in the UKIDSS/UDS observations (Dye et al. 2006; Warren et al. 2006), and as such, care was taken to confirm the reality of sources based on multiple data sets, e.g., with VISTA/VIRCAM, UKIDSS/UDS, and Spitzer/IRAC data. Any source suspected to correspond to an artifact was excluded from consideration.

Sources were then ordered in terms of the likelihood of detecting an ISM-cooling line in each. In computing these likelihoods, an SFR_{UV}-to-$L_{[C\ II]_{158\ \mu m}}$ conversion factor of $2 \times 10^7\ L_{\odot}/(M_{\odot}\ yr^{-1})$ was assumed (De Looze et al. 2014), with a 0.3 dex scatter. Additionally, $z = 6.5$–7.2 candidate sources, $z = 7.2$–7.7 candidate sources, and $z = 7.7$–9.5 candidate sources were assumed to have an allocation of 2, 3, and 6 tunings, respectively. To ensure a good sampling of luminous ISM reservoirs as a function of redshift, 20 $z = 6.5$–7.2 targets, 16 $z = 7.2$–8.5 targets, and 4 $z = 7.8$–9.4 targets were chosen.

2.4. Characteristics of the REBELS Targets

The final set of 40 targets for the REBELS program is presented in Table 1. Along with the R.A. and decl. for individual targets in our program, we also include the original source names used in the ALMA observations, UV luminosities, and photometric redshifts. UV-continuum slopes β, stellar mass estimates, [O III]$_{4959,5007}$+Hβ EWs, and SFRs are presented in Table 2. UV luminosities for sources and photometry are based on flux measurements made within 2.″4 diameter apertures.

Table 1
Bright $z > 6.5$ Candidate Galaxies Targeted by the REBELS Program

REBELS ID	ALMA ID	R.A.	Decl.	$z_{\rm phot}$	$M_{\rm UV}$	Ref[b]
REBELS-01[c]	XMM1-Z-276466	02:16:25.09	−04:57:38.5	$7.31^{+0.11}_{-0.10}$	-22.9 ± 0.1	
REBELS-02[c]	XMM1-35779	02:16:32.43	−05:30:05.6	$6.65^{+0.18}_{-0.13}$	-22.1 ± 0.2	
REBELS-03[c]	XMM1-Z-1664	02:17:15.23	−05:07:45.8	$6.99^{+0.24}_{-0.20}$	-21.8 ± 0.3	
REBELS-04	XMM-J-355	02:17:42.46	−04:58:57.4	$8.57^{+0.10}_{-0.09}$[d]	-22.3 ± 0.1	[6]
REBELS-05	XMM1-1591	02:18:11.51	−05:00:59.3	$6.68^{+0.18}_{-0.17}$	-21.6 ± 0.2	[2]
REBELS-06[c]	XMM1-Z-151269	02:18:47.47	−05:10:20.3	$6.79^{+0.13}_{-0.11}$	-21.7 ± 0.3	
REBELS-07[c,e]	XMM1-Z-1510	02:18:56.53	−05:19:58.6	$7.15^{+0.20}_{-0.14}$	-22.1 ± 0.3	[3]
REBELS-08	XMM1-67420	02:19:35.13	−05:23:19.2	$6.71^{+0.13}_{-0.10}$	-21.8 ± 0.4	[7]
REBELS-09[a]	XMM2-Z-1116453	02:21:54.15	−04:24:12.3	$7.58^{+0.27}_{-0.13}$	-23.0 ± 0.3	[6]
REBELS-10[a,c]	XMM2-Z-564239	02:22:32.59	−04:56:51.2	$7.42^{+0.23}_{-0.91}$	-22.7 ± 0.3	
REBELS-11[c]	XMM3-Y-217016	02:24:39.35	−04:48:30.0	$8.24^{+0.65}_{-0.37}$	-22.8 ± 0.2	
REBELS-12[c]	XMM3-Z-110958	02:25:07.94	−05:06:40.7	$7.40^{+0.15}_{-0.20}$	-22.5 ± 0.3	
REBELS-13[a]	XMM-J-6787	02:26:16.52	−04:07:04.1	$8.19^{+0.84}_{-0.50}$	-22.9 ± 0.2	[6]
REBELS-14[c]	XMM3-Z-432815	02:26:46.19	−04:59:53.5	$7.00^{+0.20}_{-0.27}$	-22.6 ± 0.4	
REBELS-15[c]	XMM3-Z-1122596	02:27:13.11	−04:17:59.2	$6.78^{+0.11}_{-0.09}$	-22.6 ± 0.3	
REBELS-16	MACS0429-Z1	04:29:37.20	−02:53:49.1	$6.74^{+0.09}_{-0.09}$	-21.5 ± 0.1	[1]
REBELS-17[c]	UVISTA-Z-1373	09:57:36.99	02:05:11.3	$6.66^{+0.16}_{-0.22}$	-21.7 ± 0.2	
REBELS-18	UVISTA-Y-001	09:57:47.90	02:20:43.7	$8.20^{+0.63}_{-0.37}$	-22.5 ± 0.1	[4,6]
REBELS-19	UVISTA-Y-879	09:57:54.69	02:27:54.9	$7.52^{+0.29}_{-0.21}$	-21.6 ± 0.2	[6]
REBELS-20	UVISTA-Z-734	09:59:15.88	02:07:31.9	$7.07^{+0.10}_{-0.08}$	-21.8 ± 0.1	[2]
REBELS-21	UVISTA-Z-013	09:59:19.35	02:46:41.3	$6.63^{+0.09}_{-0.12}$	-21.9 ± 0.2	[7,8]
REBELS-22	UVISTA-Y-657	09:59:20.35	02:17:22.7	$7.31^{+0.11}_{-0.10}$	-22.2 ± 0.1	[6]
REBELS-23	UVISTA-Z-1410	10:00:04.36	01:58:35.5	$6.68^{+0.12}_{-0.09}$	-21.6 ± 0.5	[7]
REBELS-24	UVISTA-Y-005	10:00:31.89	01:57:50.2	$8.35^{+0.66}_{-0.51}$	-22.0 ± 0.2	[4,6]
REBELS-25	UVISTA-Y-003	10:00:32.32	01:44:31.3	$7.40^{+0.22}_{-0.19}$	-21.7 ± 0.2	[4,6]
REBELS-26	UVISTA-Z-011	10:00:42.12	02:01:57.1	$6.64^{+0.22}_{-0.13}$	-21.8 ± 0.1	[2,7,8]
REBELS-27	UVISTA-Y-004	10:00:58.49	01:49:56.0	$7.40^{+0.13}_{-0.14}$	-22.0 ± 0.2	[4,6]
REBELS-28[c]	UVISTA-Z-1595	10:01:04.60	02:38:56.7	$6.82^{+0.13}_{-0.13}$	-22.5 ± 0.3	
REBELS-29	UVISTA-Z-004	10:01:36.85	02:37:49.1	$6.82^{+0.13}_{-0.11}$	-22.3 ± 0.1	[2,7,8]
REBELS-30	UVISTA-Z-009	10:01:52.30	02:25:42.3	$6.90^{+0.08}_{-0.09}$	-22.4 ± 0.1	[2,8]
REBELS-31	UVISTA-Z-005	10:01:58.50	02:33:08.2	$6.65^{+0.10}_{-0.06}$	-22.4 ± 0.2	[2,7,8]
REBELS-32	UVISTA-Z-049	10:01:59.07	01:53:27.5	$6.79^{+0.17}_{-0.11}$	-21.7 ± 0.1	[7,8]
REBELS-33	UVISTA-Z-018	10:02:03.81	02:13:25.1	$6.68^{+0.12}_{-0.12}$	-21.6 ± 0.1	[2,8]
REBELS-34	UVISTA-Z-002	10:02:06.47	02:13:24.2	$6.75^{+0.09}_{-0.07}$	-22.5 ± 0.1	[2,7,8]
REBELS-35	UVISTA-Z-003	10:02:06.70	02:34:21.4	$6.98^{+0.10}_{-0.10}$	-22.5 ± 0.1	[8]
REBELS-36	UVISTA-Y-002	10:02:12.56	02:30:45.7	$7.88^{+0.58}_{-0.20}$	-22.2 ± 0.2	[4]
REBELS-37	UVISTA-J-1212	10:02:31.81	02:31:17.1	$7.75^{+0.09}_{-0.17}$[d]	-22.2 ± 0.1	[6]
REBELS-38	UVISTA-Z-349	10:02:54.05	02:42:12.0	$6.67^{+0.16}_{-0.10}$	-21.9 ± 0.2	[7]
REBELS-39	UVISTA-Z-068[a]	10:03:05.25	02:18:42.7	$6.76^{+0.06}_{-0.05}$	-22.7 ± 0.2	[7]
REBELS-40	Super8-1	23:50:34.66	−43:32:32.5	$7.49^{+0.00}_{-0.08}$	-21.9 ± 0.1	[5]

Notes.
[a] Given that >15% of the integrated redshift likelihood distribution $P(z)$ for the source is at $z < 6$, this is one of two targets in the REBELS selection that could correspond to a lower-redshift interloper.
[b] [1] Smit et al. (2014), [2] Bowler et al. (2014), [3] Inoue et al. (2016), [4] Stefanon et al. (2017b, 2019a), [5] Bridge et al. (2019), [6] Bowler et al. (2020), [7] Endsley et al. (2021a), and [8] Schouws et al. (2022b).
[c] Identified here in selecting the base REBELS sample.
[d] Including the F105W, F125W, and F160W-band data from GO 15931 (PI: Bowler) and GO 16879 (PI: Stefanon).
[e] SXDF-NB1006-2 with $z_{\rm [O\,III]} = 7.2120 \pm 0.0003$ (Inoue et al. 2016).

Fiducial stellar masses and [O III]$_{4959,5007}$+Hβ EWs for sources in REBELS are derived using the BEAGLE photometric +spectroscopic stellar population fitting code (Chevallard & Charlot 2016), while our UV-continuum slopes β are derived based on power-law fits to the best-fit SED (as performed in Stefanon et al. 2019a). Our procedures for quantifying the UV-continuum slopes β, stellar masses, and [O III]$_{4959,5007}$+Hβ EWs for all 40 sources in the REBELS sample will be detailed in M. Stefanon et al. (2022, in preparation). Unobscured and obscured SFRs for targets are derived from the rest-frame UV luminosities and IR luminosities using prescriptions given in Section 4.2.

In Figure 4, we present the UV luminosities $M_{\rm UV}$ of sources in the 40 source REBELS selection versus their photometric redshift. For context, the light blue circles are included to show the UV luminosities and redshifts of sources from various legacy fields covering an area of $\sim$0.3 deg^2 (Bouwens et al. 2021). The light green hexagons indicate the UV luminosities and redshifts for other $z > 6$ sources with spectroscopic redshift

Table 2
UV-continuum Slopes, Stellar Population Parameters, and SFRs for Bright $z > 6.5$ Candidate Galaxies Targeted by the REBELS Program

REBELS ID	Redshift	β	$\log_{10} M_*$ ($M_\odot$)[a]	EW([O III]+Hβ) (Å)[a]	SFR_{UV} [$M_\odot$ yr^{-1}][b]	SFR_{IR} [$M_\odot$ yr^{-1}][c]
REBELS-01	7.177	$-2.04^{+0.24}_{-0.20}$	$10.02^{+0.41}_{-0.53}$	$2.90^{+0.28}_{-0.12}$	45 ± 5	<35
REBELS-02	$6.65^{+0.18}_{-0.13}$	$-2.24^{+0.44}_{-0.36}$	$9.04^{+0.50}_{-0.49}$	$3.07^{+0.14}_{-0.16}$	22 ± 4	<30
REBELS-03	6.969	$-2.14^{+0.63}_{-0.46}$	$9.13^{+0.64}_{-0.88}$	$3.05^{+0.33}_{-0.22}$	16 ± 4	<34
REBELS-04	$8.57^{+0.10}_{-0.09}$	$-2.15^{+0.20}_{-0.38}$	$8.72^{+1.03}_{-0.68}$	$3.25^{+0.33}_{-0.31}$	23 ± 2	59^{+20}_{-36}
REBELS-05	6.496	$-1.29^{+0.36}_{-0.44}$	$9.16^{+0.85}_{-1.00}$	$3.12^{+0.30}_{-0.32}$	14 ± 3	40^{+23}_{-16}
REBELS-06	$6.79^{+0.13}_{-0.11}$	$-1.24^{+0.67}_{-0.35}$	$9.50^{+0.45}_{-0.79}$	$2.96^{+0.27}_{-0.18}$	15 ± 4	49^{+28}_{-19}
REBELS-07	$7.15^{+0.20}_{-0.14}$	$-2.39^{+0.37}_{-0.43}$	$8.69^{+0.74}_{-0.76}$	$3.18^{+0.33}_{-0.17}$	20 ± 5	<34
REBELS-08	6.749	$-2.17^{+0.58}_{-0.58}$	$9.02^{+0.64}_{-0.68}$	$3.07^{+0.23}_{-0.22}$	16 ± 6	64^{+48}_{-24}
REBELS-09	$7.58^{+0.27}_{-0.13}$	$-2.66^{+0.93}_{-0.53}$	$8.65^{+0.43}_{-0.43}$	$3.77^{+0.05}_{-0.02}$	49 ± 14	<41
REBELS-10	$7.42^{+0.23}_{-0.91}$	$-1.34^{+0.48}_{-0.83}$	$10.16^{+0.31}_{-0.32}$	$2.95^{+0.10}_{-0.09}$	37 ± 10	<41
REBELS-11	$8.24^{+0.65}_{-0.37}$	$-1.60^{+0.17}_{-1.15}$	$9.36^{+0.52}_{-0.56}$	$3.08^{+0.21}_{-0.19}$	39 ± 8	<77
REBELS-12[d]	7.349	$-1.99^{+0.48}_{-0.76}$	$8.94^{+0.93}_{-0.70}$	$3.26^{+0.29}_{-0.25}$	30 ± 8	62^{+38}_{-28}
REBELS-13	$8.19^{+0.84}_{-0.50}$	$-1.08^{+0.59}_{-0.65}$	$9.80^{+0.43}_{-0.44}$	$2.98^{+0.13}_{-0.09}$	44 ± 9	<72
REBELS-14	7.084	$-2.21^{+0.41}_{-0.47}$	$8.73^{+0.80}_{-0.70}$	$3.21^{+0.35}_{-0.20}$	35 ± 13	41^{+24}_{-17}
REBELS-15	$6.78^{+0.11}_{-0.09}$	$-2.18^{+0.52}_{-0.50}$	$8.81^{+0.50}_{-0.50}$	$3.73^{+0.10}_{-0.54}$	33 ± 9	<44
REBELS-16	$6.74^{+0.09}_{-0.09}$	$-1.70^{+0.48}_{-0.76}$	$9.47^{+0.34}_{-0.36}$	$3.02^{+0.10}_{-0.10}$	12 ± 1	<44
REBELS-17	$6.66^{+0.16}_{-0.22}$	$-1.70^{+0.33}_{-0.47}$	$9.07^{+0.58}_{-0.63}$	$3.04^{+0.21}_{-0.19}$	15 ± 3	<48
REBELS-18	7.675	$-1.34^{+0.19}_{-0.32}$	$9.49^{+0.56}_{-0.73}$	$3.00^{+0.22}_{-0.17}$	31 ± 4	41^{+23}_{-16}
REBELS-19	7.369	$-2.33^{+0.45}_{-0.64}$	$8.79^{+0.69}_{-0.69}$	$3.11^{+0.21}_{-0.22}$	14 ± 3	52^{+31}_{-23}
REBELS-20	$7.07^{+0.10}_{-0.08}$	$-2.59^{+0.57}_{-0.60}$	$8.59^{+0.63}_{-0.63}$	$3.17^{+0.15}_{-0.11}$	16 ± 2	<52
REBELS-21	$6.63^{+0.09}_{-0.12}$	$-2.15^{+0.42}_{-0.24}$	$10.38^{+0.25}_{-0.42}$	$2.84^{+0.28}_{-0.12}$	18 ± 4	<32
REBELS-22	$7.31^{+0.11}_{-0.10}$	$-2.23^{+0.21}_{-0.30}$	$9.65^{+0.42}_{-0.76}$	$2.91^{+0.31}_{-0.14}$	23 ± 2	<34
REBELS-23	$6.68^{+0.12}_{-0.09}$	$-1.57^{+0.28}_{-0.45}$	$9.11^{+0.54}_{-0.61}$	$3.03^{+0.19}_{-0.16}$	14 ± 7	<47
REBELS-24	$8.35^{+0.66}_{-0.51}$	$-1.56^{+0.56}_{-0.83}$	$8.97^{+0.89}_{-0.89}$	$3.13^{+0.19}_{-0.21}$	20 ± 4	<38
REBELS-25	7.306	$-1.85^{+0.56}_{-0.46}$	$9.89^{+0.15}_{-0.18}$	$2.79^{+0.21}_{-0.06}$	15 ± 3	185^{+101}_{-64}
REBELS-26	$6.64^{+0.22}_{-0.13}$	$-1.92^{+0.19}_{-0.25}$	$9.54^{+0.52}_{-0.82}$	$2.98^{+0.27}_{-0.21}$	17 ± 2	<58
REBELS-27	7.090	$-1.79^{+0.42}_{-0.45}$	$9.69^{+0.25}_{-0.34}$	$2.89^{+0.27}_{-0.11}$	20 ± 4	35^{+19}_{-13}
REBELS-28	$6.82^{+0.13}_{-0.13}$	$-1.95^{+0.29}_{-0.36}$	$8.61^{+0.70}_{-0.51}$	$3.26^{+0.49}_{-0.20}$	29 ± 8	<43
REBELS-29[d]	6.685	$-1.61^{+0.10}_{-0.19}$	$9.62^{+0.19}_{-0.19}$	$2.90^{+0.12}_{-0.08}$	25 ± 3	35^{+20}_{-14}
REBELS-30	6.983	$-1.95^{+0.15}_{-0.22}$	$9.28^{+0.45}_{-0.61}$	$3.06^{+0.20}_{-0.13}$	27 ± 2	<36
REBELS-31	$6.65^{+0.10}_{-0.06}$	$-2.27^{+0.18}_{-0.33}$	$9.21^{+0.37}_{-0.37}$	$3.05^{+0.06}_{-0.06}$	27 ± 4	<52
REBELS-32	6.729	$-1.50^{+0.28}_{-0.30}$	$9.55^{+0.35}_{-0.37}$	$3.01^{+0.11}_{-0.11}$	14 ± 2	37^{+23}_{-17}
REBELS-33	$6.68^{+0.12}_{-0.12}$	$-2.04^{+0.24}_{-0.71}$	$9.39^{+0.40}_{-0.51}$	$2.90^{+0.27}_{-0.11}$	13 ± 2	<49
REBELS-34	6.633	$-2.02^{+0.07}_{-0.15}$	$9.33^{+0.33}_{-0.34}$	$3.03^{+0.07}_{-0.06}$	31 ± 2	<46
REBELS-35	$6.98^{+0.10}_{-0.10}$	$-2.07^{+0.27}_{-1.12}$	$8.91^{+0.66}_{-0.65}$	$3.18^{+0.30}_{-0.18}$	31 ± 3	<47
REBELS-36	7.677	$-2.57^{+0.48}_{-0.47}$	$9.40^{+0.76}_{-0.95}$	$2.99^{+0.25}_{-0.16}$	24 ± 4	<32
REBELS-37	$7.75^{+0.09}_{-0.17}$	$-1.24^{+0.16}_{-0.27}$	$8.58^{+0.74}_{-0.71}$	$3.25^{+0.32}_{-0.17}$	28 ± 3	74^{+18}_{-41}
REBELS-38	6.577	$-2.18^{+0.45}_{-0.42}$	$9.58^{+0.74}_{-1.27}$	$3.01^{+0.35}_{-0.25}$	18 ± 4	98^{+54}_{-35}
REBELS-39	6.847	$-1.96^{+0.30}_{-0.28}$	$8.56^{+0.57}_{-0.57}$	$3.58^{+0.17}_{-0.37}$	37 ± 6	52^{+30}_{-20}
REBELS-40	7.365	$-1.44^{+0.29}_{-0.36}$	$9.48^{+0.45}_{-0.99}$	$2.98^{+0.32}_{-0.20}$	17 ± 1	35^{+20}_{-14}

Notes.
[a] Estimated using BEAGLE (Chevallard & Charlot 2016) assuming a constant star formation history (CSFH). See M. Stefanon et al. (2022, in preparation) for details. Note that alternate estimates of the EWs are provided assuming a delayed star formation history in Table 4 of Appendix B.
[b] Derived from the measured UV luminosity using the prescription given in Section 4.2.
[c] Derived from the measured IR luminosity L_{IR} (Inami et al. 2022) using the prescription given in Section 4.2. Note that no use of this SFR is made for Figure 5. Instead, for that figure, SFR_{IR} is taken to be $(10^{0.19} - 1)SFR_{UV}$ as found for the average luminous $z \sim 7$ source by Schouws et al. (2022a).
[d] Estimates of the stellar mass presented in Fudamoto et al. (2021) for REBELS-12 and REBELS-29 are higher by ~0.7–1.0 dex than those quoted here using BEAGLE and assuming a constant star formation history, and are more in line with stellar mass estimates from PROSPECTOR relying on nonparametric star formation histories (M. Stefanon et al. 2022, in preparation; Topping et al. 2022). Estimates for the obscured SFR estimates from Fudamoto et al. (2021) are almost identical to what we present here, while the UV SFRs are ~0.1 dex higher.

determinations from ALMA. The solid and open blue circles are sources with redshift measurements from $\geqslant 7\sigma$ and $<7\sigma$ Lyα lines, respectively (Vanzella et al. 2011; Schenker et al. 2012; Shibuya et al. 2012; Ono et al. 2012, Pentericci et al. 2011; Jiang et al. 2013; Oesch et al. 2015; Sobral et al. 2015; Zitrin et al. 2015; Song et al. 2016; Hoag et al. 2017; Stark et al. 2017; Larson et al. 2018; Pentericci et al. 2018; Fuller et al. 2020; Jung et al. 2020; Endsley et al. 2021a; Laporte et al. 2021; Pelliccia et al. 2021).

Figure 5 shows the approximate SFRs of targets in the REBELS program versus their inferred stellar masses (solid red circles). These results are shown (shaded gray region) relative to

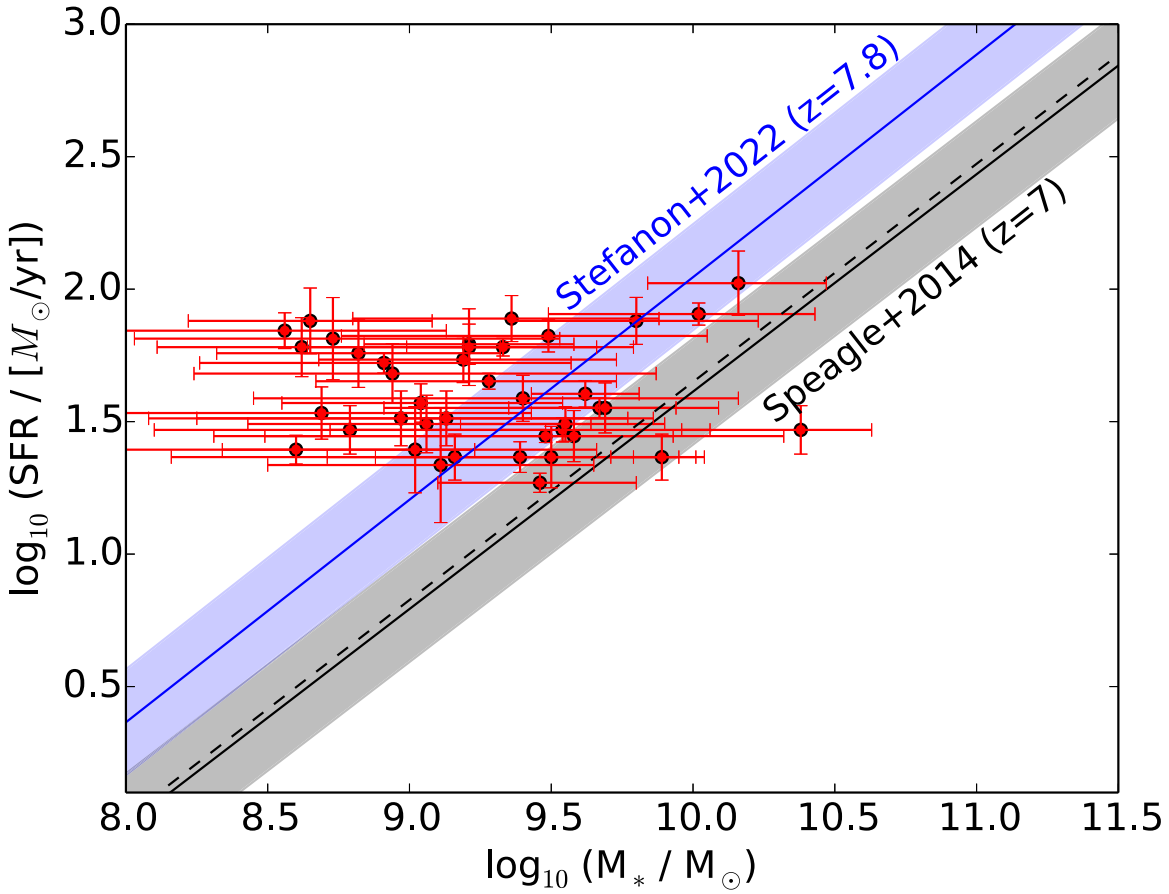

Figure 5. Estimated star formation rate versus stellar mass for the 40 targets (solid red circles) in the REBELS program. The shaded gray region shows the star-forming main sequence implied by the Speagle et al. (2014) fitting formula results at $z \sim 7$, while the dashed black line shows the implied main sequence at $z \sim 7.8$. The blue shaded region offsets this main sequence vertically to match the Stefanon et al. (2022) specific star formation rate results at $z \sim 7.8$. The stellar masses shown in this figure are derived from the REBELS photometry using BEAGLE (M. Stefanon et al. 2022, in preparation) and assuming a constant star formation history. Meanwhile, the SFRs shown in this figure are the unobscured SFRs derived from the rest-UV data corrected upward by ∼0.19 dex to account for the average contribution of the obscured SF (prior to the execution of the REBELS program) to the total (as found by Schouws et al. (2022a)). Our assumption of a constant star formation history may result in a significant underestimation of the stellar masses for sources with bursty star formation histories (Topping et al. 2022). An improved version of the presented relation will be presented in Topping et al. (2022).

the main sequence at $z \sim 7$ implied by the Speagle et al. (2014) star-forming main-sequence fitting formula $\log_{10}\mathrm{SFR}(M_*, t) = (0.84 \pm 0.02 - (0.026 \pm 0.003)t)\log_{10} M_* - (6.51 \pm 0.24 - (0.11 \pm 0.03)t)$ where t is the age of the universe in Gyr. Also shown for comparison is the main-sequence relation shifted to match the specific star formation results from Stefanon et al. (2022) at $z \sim 7.8$ (shaded blue region). Overall, the REBELS targets are distributed both above and below the main-sequence relation (particularly that derived by Stefanon et al. 2022). Our assuming a constant star formation history may result in a significant underestimate of the stellar masses for sources with bursty star formation histories (Topping et al. 2022). Topping et al. (2022) will provide an improved discussion of where the REBELS targets fall on the SFR versus stellar mass relation.

Figure 17 from Appendix B shows the distribution of the REBELS targets in stellar mass and compares this distribution with that inferred (Faisst et al. 2020) for the $z = 4$–6 ALPINE sample. The REBELS sample spans a range in stellar mass similar to that of ALPINE. The median stellar masses for the REBELS sample inferred from the BEAGLE and PROSPECTOR stellar population fitting codes (assuming constant and nonparametric star formation histories, respectively) are $10^{9.25}$ $M_\odot$ and $10^{9.79}$ $M_\odot$, ∼0.4 dex lower and ∼0.1 dex higher than inferred for ALPINE. Stellar mass estimates for sources in our sample from PROSPECTOR will be presented in M. Stefanon et al. (2022, in preparation). Thanks to the similarities between the samples, ALPINE provides us with a convenient $z = 4$–6 comparison sample for assessing evolution in the galaxy population with redshift.

The distribution of REBELS targets in redshift, UV luminosity, UV-continuum slope β, and [O III]$_{4959,5007}$+Hβ EW is illustrated in Figure 18 of Appendix B. The latter two distributions appear to be completely consistent with that found for the $z \sim 7$ galaxy population as a whole, suggesting that results derived from REBELS should be representative of the general population of massive star-forming galaxies at $z > 6.5$. Despite the similar stellar mass characteristics of the two samples, REBELS does not include targets that extend as faint in UV luminosities as ALPINE does (as Figure 4 makes clear).

3. Observational Implementation of REBELS Survey

3.1. Choice of ISM Cooling Line for Spectral Scans

Galaxies with the most luminous ISM reservoirs shine very brightly in both the 157.74 μm [C II] and 88.36 μm [O III] ISM-cooling lines, and both lines are readily detectable with ALMA over a significant fraction of the redshift range between $z \sim 6$ and $z \sim 10$. As a result, ALMA has already been successful in

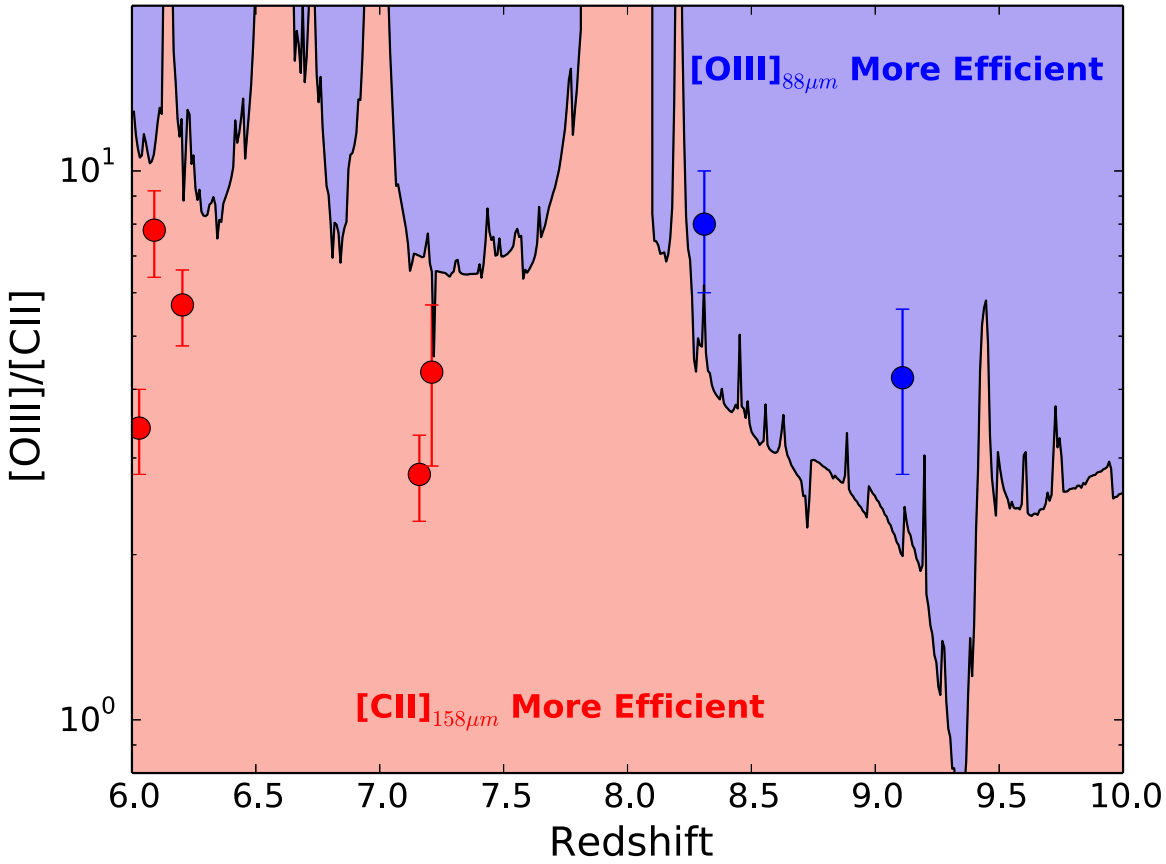

Figure 6. The break-even [O III]$_{88\ \mu m}$/[C II]$_{158\ \mu m}$ luminosity ratio where [C II]$_{158\ \mu m}$ and [O III]$_{88\ \mu m}$ scans are equally efficient to execute (Section 3.1). The plotted red and blue circles show the measured [O III]$_{88\ \mu m}$/[C II]$_{158\ \mu m}$ luminosity ratios for specific high-redshift sources (Hashimoto et al. 2019; Bakx et al. 2020; Carniani et al. 2020; Harikane et al. 2020) featuring $\geqslant 5\sigma$ line detections and where the emission is largely cospatial (but see Carniani et al. 2017). For luminosity ratios in the red regions, [C II]$_{158\ \mu m}$ scans are more efficient, while for luminosity ratios in the blue regions, [O III]$_{88\ \mu m}$ scans are more efficient. The break-even ratios are computed based on the integration times required to detect [C II]$_{158\ \mu m}$ and [O III]$_{88\ \mu m}$ lines at a given redshift and rely on the atmospheric transmission at a given frequency using the equations in the ALMA Technical Handbook (Cortes et al. 2020). Use of the [C II]$_{158\ \mu m}$ line for spectral scans seems to be more efficient for galaxies at $z = 6.5$–8.2, while use of the [O III]$_{88\ \mu m}$ line for spectral scans at $z > 8.5$ seems more efficient.

scanning for the [C II]$_{158\ \mu m}$ line in five sources at $z \sim 6$–7 (Smit et al. 2018; Schouws et al. 2022b) as well as uncovering serendipitous galaxies in the immediate neighborhood of $z \sim 6$–7 QSOs (Decarli et al. 2017; Venemans et al. 2019, 2020). Similarly, spectral scans for the [O III]$_{88\ \mu m}$ line have been shown to allow for efficient redshift determinations for galaxies at $z > 8$ (e.g., Hashimoto et al. 2018; Tamura et al. 2019).

As such, we could potentially target either transition in searching for bright ISM-cooling lines in $z > 6$ galaxies. To help decide which line would be more efficient, we calculated the approximate break-even luminosity $L_{[\mathrm{O\ III}]_{88\ \mu m}}/L_{[\mathrm{C\ II}]_{158\ \mu m}}$ ratio for [O III]$_{88\ \mu m}$ versus [C II]$_{158\ \mu m}$ spectral scans as a function of redshift. In calculating this ratio, we expressly made use of the atmospheric transmission, using Equation (9.8) from the ALMA Technical Handbook[27] and the specified inputs to this equation from chapter 9 of the handbook to derive sensitivities for a given integration time (Cortes et al. 2020). Observations were assumed to be conducted in a precipitable water vapor (PWV) octile consistent with that shown in Figure 9.1 of the ALMA Technical Handbook, i.e., with band 6 observations being conducted in the fifth octile weather and band 7 observations being conducted in generally better weather but depending on the observational frequency. As a check on the results from our sensitivity calculations, use was made of the ALMA sensitivity calculator. Also, account was made for the line scans with [O III]$_{88\ \mu m}$ covering a 1.8× smaller range in Δz than [C II]$_{158\ \mu m}$ (due to the higher frequency of [O III]$_{88\ \mu m}$). The FWHM of the [C II]$_{158\ \mu m}$ and [O III]$_{88\ \mu m}$ lines was assumed to be the same, i.e., 250 km s^{-1}, for this calculation. Such an FWHM is fairly typical for ISM-cooling lines found for UV-bright $z > 6$ galaxies (e.g., Matthee et al. 2019; Harikane et al. 2020; Schouws et al. 2022a) and is consistent with theoretical expectations (Kohandel et al. 2019, 2020). We emphasize that other FWHMs should yield essentially identical results.

The results are shown in Figure 6. For the typical luminosity ratios observed for $z \sim 6$–8 galaxies, i.e., ∼4 (e.g., Bakx et al. 2020; Carniani et al. 2020; Harikane et al. 2020; Inoue et al. 2016), not only is [C II]$_{158\ \mu m}$ clearly the most efficient line to use for our spectral scans in the redshift range $z \sim 6.0$ to $z \sim 8.5$, but also is not subject to significant gaps in redshift coverage. For sources at $z > 8.5$, by contrast, [O III]$_{88\ \mu m}$ is the most efficient line to use for spectral scans. The [O III]$_{88\ \mu m}$ scans do become significantly less efficient at a redshift $z \sim 9.4$ due to the $H_2O\ 5_{15} - 4_{22}$ line in the Earth's atmosphere at 325 GHz, but [C II]$_{158\ \mu m}$ is also not especially

[27] https://almascience.eso.org/documents-and-tools/cycle8/alma-technical-handbook

efficient at that redshift, due to the $H_2O\ 3_{13}-2_{20}$ line at 183 GHz.

3.2. Setup of the Spectral Scan Windows

Here, we describe our strategy for setting up the tunings for our spectral scans. For each target, we aim to optimally cover the redshift likelihood distribution derived combining the results from three independent sets of photometry (Figure 2).

For bright sources in the redshift range $z = 6.5$–7.2, the redshifts of sources can be accurately estimated thanks to the Lyman-break and high-EW [O III]$_{4959,5007}$ doublet lying very close to edge of multiple spectral elements ($z_{\rm Subaru}$, $z_{\rm HSC}$, $Y_{\rm VISTA}$, $y_{\rm HSC}$, [3.6], and [4.5]) with deep coverage over the COSMOS/UltraVISTA, VIDEO/XMM-LSS, and UKIDSS/UDS fields. For $z = 6.5$–7.2 sources over the COSMOS/UltraVISTA field, the median Δz uncertainty is ± 0.11 while over the VIDEO/XMM-LSS + UKIDSS/UDS fields, the median Δz uncertainty is ± 0.15. For most $z = 6.5$–7.2 sources over the COSMOS/UltraVISTA field, we find that we can use [C II]$_{158\ \mu\rm m}$ scans to cover $\sim$89% of the likelihood distribution with two redshift tunings, each covering a contiguous 5.375 GHz frequency range (and a 10.75 GHz contiguous range in total). REBELS-08 in Figure 15 of Appendix A is one example of a source where we used this tuning strategy.

From $z = 7.2$ to $z = 7.7$, the redshifts of sources are largely constrained based on the position of the Lyman break in the Y-band filter. Nevertheless, since there are fewer passbands with flux measurements providing direct constraints on the redshifts of sources, the median uncertainty on the redshifts of sources is larger, with a value of ± 0.15. For sources in this redshift range, we find that we can use [C II]$_{158\ \mu\rm m}$ scans to cover the 91% of the redshift likelihood distribution in three tunings covering a contiguous frequency range of 20.375 GHz (5.375 + 7.5 + 7.5 GHz). REBELS-01 in Figure 15 of Appendix A is one example of a source where we used this tuning strategy.

For sources with photometric redshifts in excess of 7.7, the redshift uncertainties increase substantially, due to the Lyman break falling between the ground-based Y and J bands. For these sources, the redshift likelihood distribution typically extended from $z \sim 7.7$ to 9.3, with a median uncertainty of ± 0.44. To execute a spectral scan for the ISM-cooling line over this range, we made use of [C II]$_{158\ \mu\rm m}$ scans in cases where such a scan had already begun as part of a cycle-6 program (2018.1.00236.S, PI: Stefanon) probing the dust continuum. Otherwise, sources required six tunings in band 7 to search for [O III]$_{88\ \mu\rm m}$ (probing the redshift range $z = 8.10$ to 9.39) and approximately three tunings in band 6 to search for [C II]$_{158\ \mu\rm m}$ (probing the range $z = 7.37$–8.00).[28]

We present the spectral scan windows we use for the 40 targets in the REBELS LP in Figures 15 and 16 of Appendix A. In total, 16 of the targets from the program required 2 tunings to cover the redshift likelihood distribution, 17 targets required 3 tunings, 1 target required 4 tunings, 2 targets required 5 tunings, 1 target required 6 tunings, and 1 target required 8 tunings. For 2 targets, only 1 tuning was allocated to extend scans that had already started in our second pilot program (Schouws et al. 2022b). In total, the number of targets × tuning windows for the REBELS program is equal to 91 for the [C II]$_{158\ \mu\rm m}$ line and 22 for the [O III]$_{88\ \mu\rm m}$ line. Archival ALMA observations contributed an additional 12 tunings to our [C II]$_{158\ \mu\rm m}$ scans (see Appendix A).

[28] Because of some adjustments made to our program after submission, there was insufficient time to scan the redshift range $z = 7.7$ to 8.1 for REBELS-11 and REBELS-13.

3.3. Sensitivity Requirements for Spectral Scans

Our sensitivity requirements for REBELS relies on our experience with searches in our pilot programs (Smit et al. 2018; Schouws et al. 2022b). There, the detected [C II]$_{158\ \mu\rm m}$ lines had peak fluxes of 1.5–4.0 mJy. To guarantee the selection of similar sources at $z \sim 7$ with REBELS, we required that the peak flux sensitivity be $\sim$340 μJy in a 66 km s^{-1} channel such that sources with a peak flux of 1 mJy can be detected at 5σ when combining multiple channels. This is equivalent to a 5σ limiting point-source luminosity of $\sim 3 \times 10^8 L_\odot$ at $z \sim 7$ (assuming a line width of 250 km s^{-1}), which requires $\sim$20 minutes of integration time per tuning. Reaching the same limiting luminosity at $z \sim 8$ requires a 300 μJy sensitivity and $\sim$30–40 minutes of integration time in band 5 or 6 (for $z > 8$ and $z < 8$ [C II]$_{158\ \mu\rm m}$ searches, respectively). In scanning for the bright [O III]$_{88\ \mu\rm m}$ lines in our $z \sim 9$ targets, the equivalent sensitivity requirement is 450 μJy, assuming an [O III]$_{88\ \mu\rm m}$/[C II]$_{158\ \mu\rm m}$ luminosity ratio of 3.5.

For the purposes of illustration, the limiting [C II]$_{158\ \mu\rm m}$ and [O III]$_{88\ \mu\rm m}$ luminosities probed as a function of source redshift for the spectral scans planned for sources in REBELS are provided in Figure 7. This is for the requisite sensitivity specified for the REBELS program. In practice, the sensitivity achieved is typically $\sim$1.4× better than specified (S. Schouws et al. 2022, in preparation), allowing us to detect even lower-luminosity ISM-cooling lines (indicated with the lighter shading in Figure 7). For context, we have included the [C II]$_{158\ \mu\rm m}$ luminosities and redshifts of detected sources from the literature (gray circles) and our pilot programs (filled stars). As should be clear from the figure, REBELS will detect line emission from sources if their [C II]$_{158\ \mu\rm m}$ luminosities exceed $\sim 3 \times 10^8\ L_\odot$ and $\sim 2 \times 10^8\ L_\odot$ (requested and typical sensitivities, respectively), and for $z > 8.5$ targets, if their [O III]$_{88\ \mu\rm m}$ luminosities exceed $\sim 1.1 \times 10^9 L_\odot$ and $0.8 \times 10^9 L_\odot$ (required and typical sensitivities, respectively).

To maximize the sensitivity of the REBELS spectral scan observations and not overresolve the [C II]$_{158\ \mu\rm m}$ line, observations were conducted in the lowest spatial resolution configurations (C43-1 and C43-2), with $\sim$1.″2–1.″6 FWHM. The REBELS observations were obtained in frequency domain mode (FDM) at a spectral resolution of 488 MHz and then spectrally averaged in bins of size 16, giving the output data a spectral resolution of 7.813 MHz, equivalent to a velocity resolution of $\sim$9 km s^{-1} for [C II]$_{158\ \mu\rm m}$ line at $z \sim 7$. Given that [C II]$_{158\ \mu\rm m}$ lines in luminous $z \sim 7$ galaxies have been found to have a minimum FWHM of $\sim$80 km s^{-1} and more typically 250 km s^{-1}, this was expected to be more than sufficient to study the kinematic structure of sources revealed by the program.

Of the $z \sim 7$ galaxies targeted with observations from our pilot programs, 63% yielded lines with luminosities in excess of $2 \times 10^8\ L_\odot$. Given that similar selection criteria are used for the REBELS large program, we would expect a similar detection rate of [C II]$_{158\ \mu\rm m}$ for the REBELS program, suggesting we will detect lines in 25 out of 40 targets. Combining the expected results with previous [C II]$_{158\ \mu\rm m}$ and [O III]$_{88\ \mu\rm m}$ line detections, we expected $\geqslant$35 $z > 6.5$ galaxies with ALMA line detections once the program was completed.

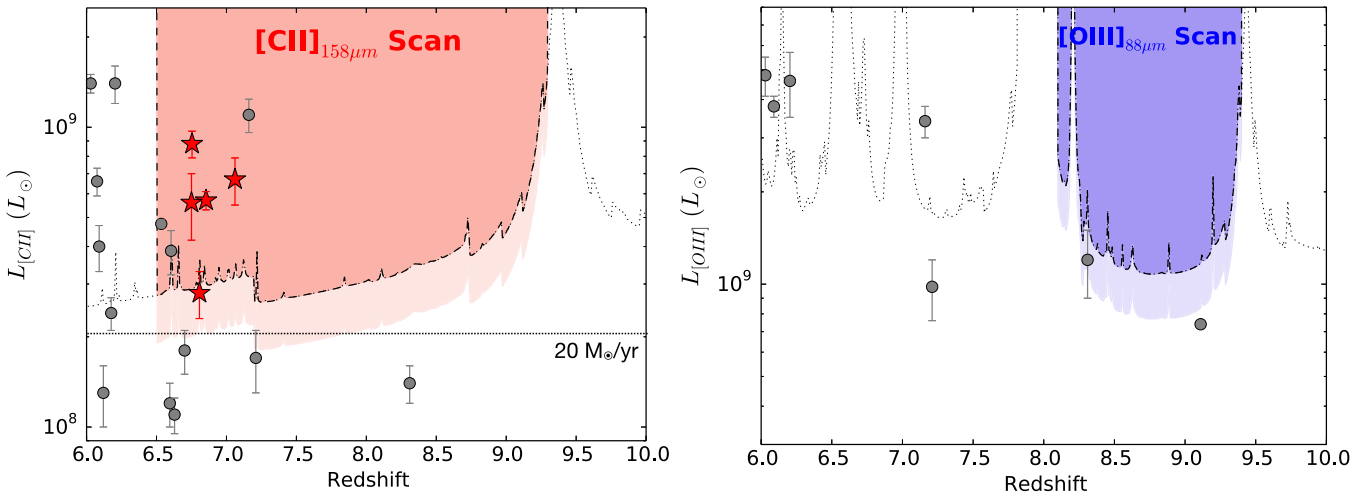

Figure 7. The shaded regions indicate the parameter space we are scanning for [C II]$_{158\ \mu m}$ and [O III]$_{88\ \mu m}$ in our 36 targeted $z \sim 6.5$–8.5 and 4 $z \sim 8.2$–9.4 galaxies (assuming a 5σ detection threshold and the specified sensitivity). The dotted line is computed using the equations in the ALMA Technical Handbook (Cortes et al. 2020), as in Figure 6. The lighter shaded regions show the luminosities probed for the more typical sensitivity reached in the REBELS observations. For context, [C II]$_{158\ \mu m}$ and [O III]$_{88\ \mu m}$ detections (left and right panels, respectively) from the pilot program (red and blue stars; Smit et al. 2018; Schouws et al. 2022b) and the literature (gray circles) are also included here. The approximate limiting luminosity achieved in a typical [C II]$_{158\ \mu m}$ scan (for a 5σ detection threshold) is 20 $M_\odot$ yr^{-1} (dotted horizontal line), assuming the De Looze et al. (2014) $z \sim 0$ [C II]$_{158\ \mu m}$–SFR relation.

This is a sufficient number for a detailed physical characterization of massive galaxies at $z \gtrsim 6.5$ and a study of their evolution.

3.4. Dust-continuum Sensitivities

The detection of dust-continuum emission from star-forming galaxies at $z \sim 5$–8 with ALMA has been found to be much more difficult than detection of the [C II]$_{158\ \mu m}$ or [O III]$_{88\ \mu m}$ ISM-cooling lines. This basic difference in detectability was already evident in $z \sim 5.5$ results by Capak et al. (2015), who were able to detect all 10 luminous $z = 5.2$–5.7 galaxies they targeted in [C II]$_{158\ \mu m}$, but were only able to detect 4 of the 10 sources in the dust continuum. Other results available on $z > 5$ galaxies have been similar, with [C II]$_{158\ \mu m}$ being detected in a much larger fraction of sources than the dust continuum (e.g., Maiolino et al. 2015; Willott et al. 2015; Inoue et al. 2016; Matthee et al. 2017, 2019; Béthermin et al. 2020; Harikane et al. 2020).

The relative detectability of ISM-cooling lines like [C II]$_{158\ \mu m}$ or [O III]$_{88\ \mu m}$ and the dust continuum can be quantified on the basis of their measured $L_{[\mathrm{C\ II}]_{158\ \mu m}}$-to-$L_{\mathrm{IR}}$ ratios or $L_{[\mathrm{O\ III}]_{88\ \mu m}}$-to-$L_{\mathrm{IR}}$ ratios. Compiling previous results from Capak et al. (2015), ALPINE (Béthermin et al. 2020; Faisst et al. 2020; Le Fevre et al. 2020), Smit et al. (2018), Schouws et al. (2022a), and Schouws et al. (2022b), we can calculate the relative integration time required to detect sources in the dust continuum and the integration time required to detect sources in [C II]$_{158\ \mu m}$. In performing this calculation, we assume a line width of 235 km s^{-1} (FWHM) for both the [C II]$_{158\ \mu m}$ and [O III]$_{88\ \mu m}$ lines, and we assume a modified blackbody form for the dust-continuum SED with a dust temperature of 50 K and dust emissivity index β of 1.6, which lies intermediate between the lowest and highest dust temperature measurements at $z > 7$ (e.g., Knudsen et al. 2017; Bakx et al. 2020). We present results in Figure 8.

Given the much longer exposure times required to detect sources in the dust continuum than in either [C II]$_{158\ \mu m}$ or [O III]$_{88\ \mu m}$, our use of multiple tuning windows for spectral scans really does provide an advantage in allowing us to probe the dust continuum. We have illustrated the approximate IR luminosities we are able to probe with the REBELS LP in Figure 9. Two spectral scan windows (10.75 GHz bandwidth) are assumed at $z = 6.5$–7.2, three spectral scan windows (20.375 GHz bandwidth) at $z = 7.2$–7.7, and six spectral scan windows (45 GHz bandwidth) at $z > 7.7$.

The REBELS dust-continuum probe also allows for a very valuable assessment of incompleteness in our spectral scan results. This is because incompleteness can arise as a result of (1) scan range not extending over a wide enough range in frequency to find the relevant ISM-cooling line or (2) the relevant ISM-cooling line being fainter than the 5σ detection limit for the spectral scan. Given the strong correlation between dust-continuum luminosities of galaxies and the luminosities of [C II]$_{158\ \mu m}$ and [O III]$_{88\ \mu m}$, the detection of the dust continuum in a source strongly suggests that the associated ISM cooling is sufficiently bright to have been detected in our spectral scans. If the ISM line is not found but the dust continuum is, it strongly suggests the spectral scan did not extend broadly enough in frequency. In cases where neither the line nor the dust continuum is detected, it may mean that the line is fainter than the sensitivity limits of the scans (or in the worst case at lower redshift, but our careful selection suggests that the number of such targets in the REBELS program is small).

3.5. Summary and Execution of Program

The REBELS LP observations began on 2019 November 15, when ALMA was in the C43-2 configuration, and continued until 2020 January 10, while ALMA was in configurations C43-1 and C43-2. Thus far, 60.6 hr of ALMA observations have been acquired, with 8 hr remaining to be observed.

Thirty-four targets from the program have now been fully observed. Observations are still incoming for REBELS-04, REBELS-06, REBELS-11, REBELS-16, REBELS-24, and REBELS-37. Two of the sources with incoming observations are part of our 33-target $z = 6.5$–7.7 sample. The remaining

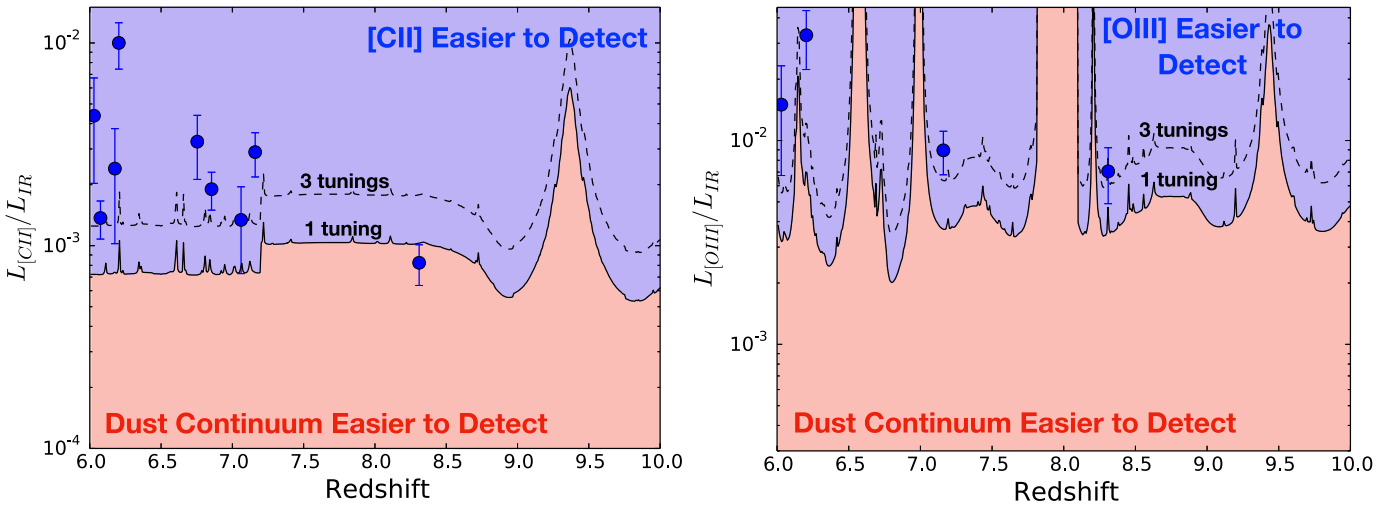

Figure 8. The break-even [C II]$_{158\ \mu m}$/IR and [O III]$_{88\ \mu m}$/IR luminosity ratio (left and right panels, respectively) for both detection (5σ) of the [C II]$_{158\ \mu m}$ and [O III]$_{88\ \mu m}$ lines and detection (3.3σ) of the dust continuum shown as a function of redshift. Also shown on this diagram are $z \sim 6$–10 sources from the REBELS pilot programs (Smit et al. 2018; Schouws et al. 2022a, 2022b) and the literature (Hashimoto et al. 2019; Tamura et al. 2019; Bakx et al. 2020; Harikane et al. 2020). The dashed lines show the break-even ratios assuming three separate tunings for a spectral scan. The use of >3 tunings would shift the break-even ratio to even higher values. For the typical source, one can clearly consider up to six tunings per source before the line sensitivity of ALMA becomes the limiting factor in probing both line and continuum emission. This fits very well with the spectral scan strategy employed in REBELS, where the aim is to probe both lines and the dust continuum.

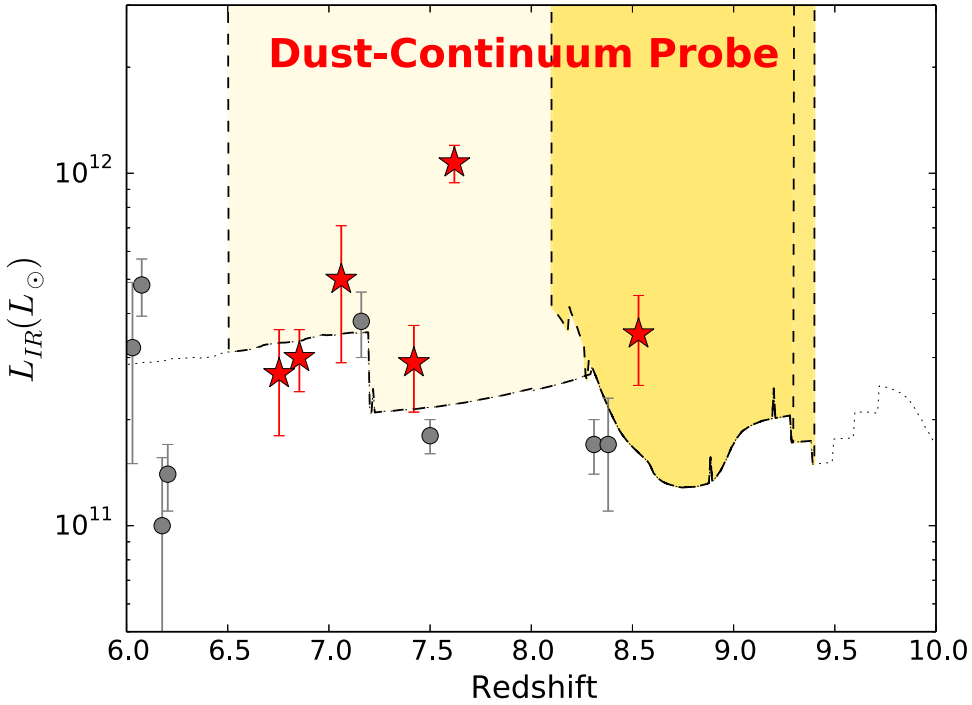

Figure 9. The 3.3σ limiting IR luminosities probed by the REBELS scans for [C II]$_{158\ \mu m}$ and [O III]$_{88\ \mu m}$ in 40 very bright reionization-era galaxies (light yellow and gold shaded regions, respectively). The red stars show the IR luminosities of six $z = 7$-8 galaxies from the REBELS pilot programs (Schouws et al. 2022a; Smit et al. 2018) while the gray circles show the IR luminosities inferred for various dust-detected galaxies in the literature. REBELS will detect sources in the dust continuum if their IR luminosities are greater than $3 \times 10^{11} L_\odot$ to $z \sim 7.2$ and down to $2 \times 10^{11}\ L_\odot$ at $z = 7.2$–9.4 (equivalent to obscured SFRs of 36 $M_\odot$ yr^{-1} and 24 $M_\odot$ yr^{-1}, respectively). Extrapolating our pilot results, the REBELS program is projected to increase the number of dust detections by 3–4× at $z > 6.5$, and will allow us to test whether large dust reservoirs are common (as suggested by our detections and also the Watson et al. (2015) and Laporte et al. (2017) sources at $z \sim 7.5$ and $z = 8.38$, respectively) or whether there is a rapid decline in IR bright galaxies at $z > 7.5$.

four are part of our seven-target $z = 7.7$–9.4 sample. The REBELS spectral scans for our $z = 6.5$–7.7 and $z = 7.7$–9.4 targets are therefore 94% and 43% complete, respectively.

Following the first year of observations from the REBELS program and successful detection of [C II]$_{158\ \mu m}$ in REBELS-18 and REBELS-36, several tunings from REBELS-18 and REBELS-36 were shifted to REBELS-06, REBELS-16, and REBELS-37 to extend the spectral scan range for [C II]$_{158\ \mu m}$ in those sources.

The remaining observations appear likely to be executed in March 2022 when the configuration of ALMA is in C43-1 or C43-2, according to the current JAO schedule.

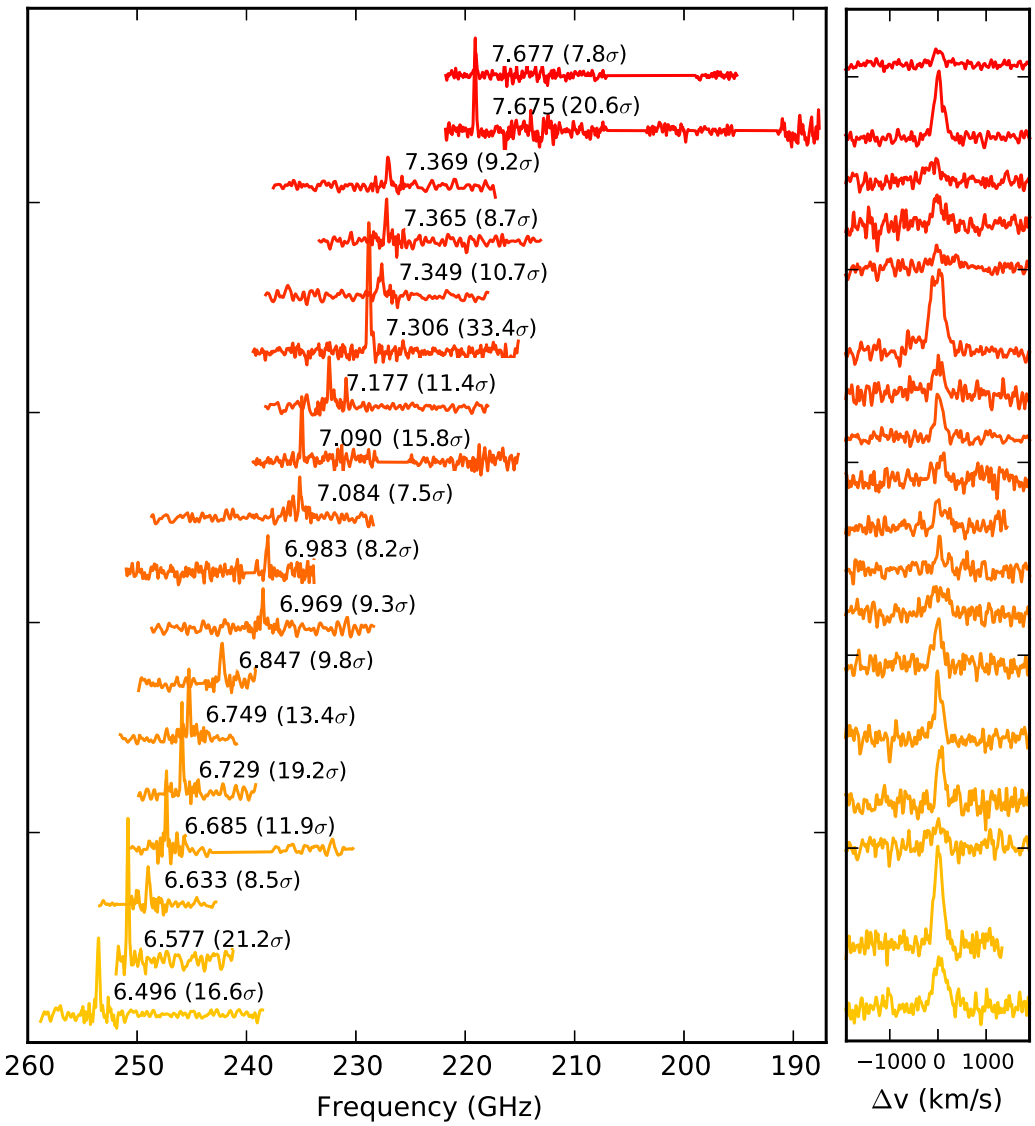

Figure 10. (left) Illustration of the highest-significance ($\geqslant 7\sigma$) ISM-cooling lines identified to date in the REBELS program, and the band-5/6 spectral scans used to locate these lines (Section 4.1). Shown on the figure next to the [C II]$_{158\ \mu m}$ line detections are the systemic redshifts of the sources as well as an estimate of the significance of the line detection. (right) Velocity structure of the same line detections as shown in the left panel. More details on these line detections and on the characteristics of even fainter, lower-S/N line detections in the REBELS first-year data will be presented in S. Schouws et al. (2022, in preparation).

4. Spectral Scan Results

The purpose of this section is to provide a quick overview of some of the most prominent ISM-cooling line detections obtained thus far with the REBELS LP observations, and to assess how effective the observational strategy has been.

4.1. Processing of the ALMA Data and Initial Results

Here, we provide a very brief summary of the procedures used to reduce and calibrate ALMA observations from the REBELS program. More details will be given in S. Schouws et al. (2022, in preparation) and Inami et al. (2022).

Reduction and calibration of data from the program were performed using the standard ALMA calibration pipeline as implemented in the Common Astronomy Software Applications package (CASA) version 5.6.1. Data cubes were reimaged with the `tclean` task using a natural weighting to maximize our sensitivity for detecting ISM-cooling lines in ALMA band-5/6/7 observations obtained from the program. Cleaning was done down to 2σ in producing the data cubes.

Line searches were performed using three different line-search algorithms on the reduced data cubes. Searches for $>5\sigma$ lines were performed within 1" of the target center in the rest UV. Line widths from 80 to 600 km s^{-1} were considered in searching for lines throughout our data cubes. S. Schouws et al. (2022, in preparation) will provide a detailed description of our line search procedures and catalogs, while carefully quantifying both the completeness and purity of the line searches.

As an illustration of the effectiveness of the spectral scans employed in the REBELS program to date, we include in Figure 10 the 18 [C II]$_{158\ \mu m}$ lines detected with a significance of $>7\sigma$. These lines are also presented in Table 3. Redshifts of the detected [C II]$_{158\ \mu m}$ lines range from $z = 6.496$ to 7.677. The value of 7σ was adopted as the detection threshold in this paper to keep the focus on the brightest and most significant lines found in the survey. Details on the purity of our ISM line searches, characteristics of the [C II]$_{158\ \mu m}$ line detections, as

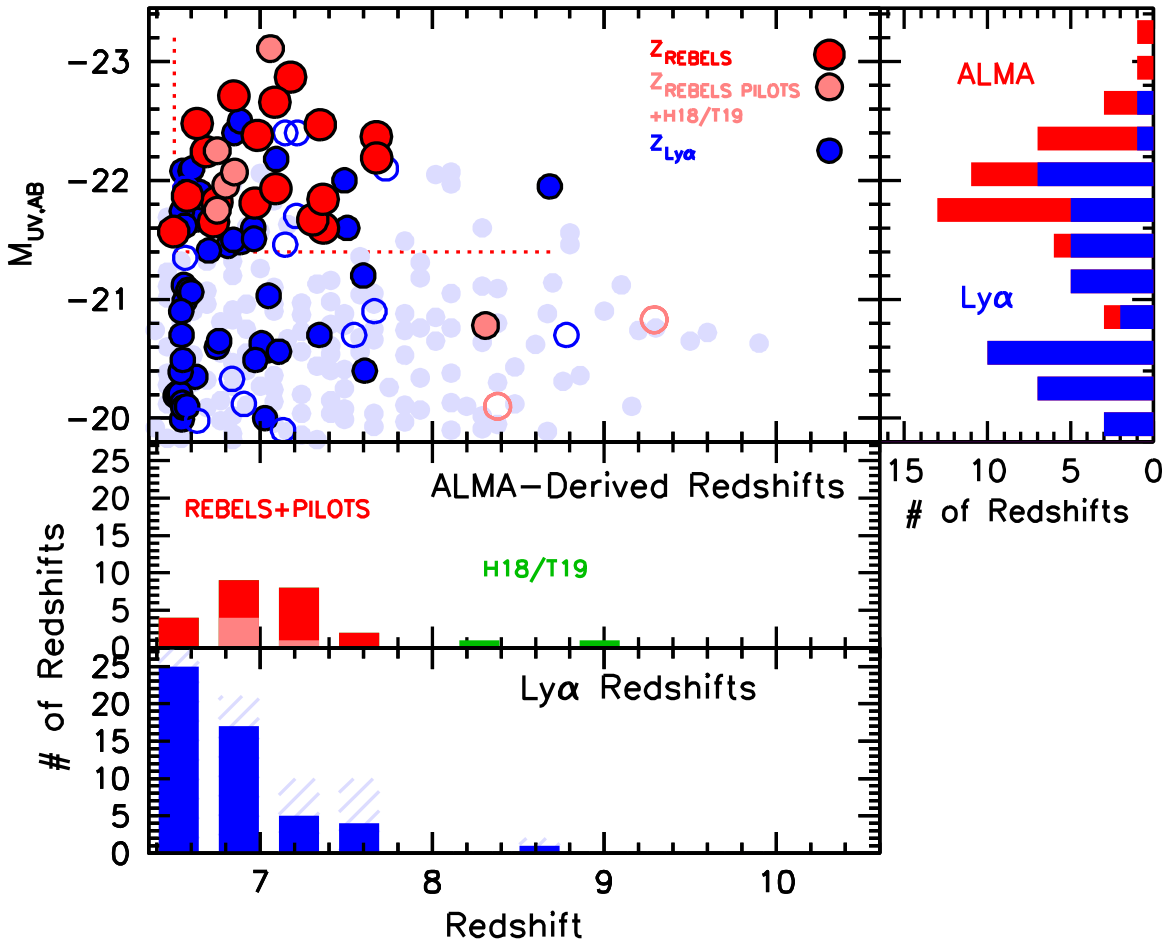

Figure 11. (upper panel) UV luminosity versus spectroscopic redshift measurement from $[C\ II]_{158\ \mu m}$ based on observations from the REBELS ALMA large program (red circles). Also shown (light red circles) are the UV luminosities and spectroscopic redshift for sources from the REBELS pilot programs (Smit et al. 2018; Schouws et al. 2022a, 2022b) and other spectral scan programs in the literature (Hashimoto et al. 2018; Tamura et al. 2019). For context, the UV luminosities and existing spectroscopic redshift measurements from the Lyα line are shown as the blue circles. The $z > 6.5$ sources with redshift determinations based on Lyα and $[O\ III]_{88\ \mu m}$ lines where the significance is $<7\sigma$ are shown with open blue circles and open light red circles, respectively. The light blue circles are also shown for context, and are based on the UV luminosities and photometric redshifts of sources over HST legacy fields (Bouwens et al. 2021). (middle panel) The number of spectroscopic redshifts available as a function of redshift relying on only the most prominent ($>7\sigma$) $[C\ II]_{158\ \mu m}$ -detected galaxies in the REBELS large program and pilot programs (red and light red histogram, respectively). The green histogram shows the numbers based on other spectral scan programs in the literature (Hashimoto et al. 2018; Tamura et al. 2019). (lower panel) The number of spectroscopic redshifts available as a function of redshift relying on $\geqslant 7\sigma$ and 5σ–7σ Lyα-detected galaxies at $z > 6.5$ (blue and light blue hatched histogram, respectively). (right panel) Number of spectroscopic redshifts from ALMA (red histogram) and Lyα (blue histogram) on the basis of $\geqslant 7\sigma$ lines. Notice how there are already $\approx 2\times$ as many spectroscopic redshifts available for the brightest ($M_{UV,AB} < -22$) sources from ALMA as available from Lyα.

Table 3
Discovered $\geqslant 7\sigma$ $[C\ II]_{158\ \mu m}$ Lines in the First-year Data from the REBELS Program

REBELS ID	$\nu_{[C\ II]}$ (GHz)	$z_{[C\ II]}$	$S/N_{[C\ II]}$[a]	$S/N_{continuum}$[a]
REBELS-01	232.42	7.177	11.4	<3.3
REBELS-03	238.49	6.969	9.3	<3.3
REBELS-05	253.53	6.496	16.6	5.5
REBELS-08	245.25	6.749	13.4	5.0
REBELS-12	227.65	7.349	10.7	3.4
REBELS-14	235.09	7.084	7.5	5.1
REBELS-18	219.08	7.675	20.6	4.9
REBELS-19	227.09	7.369	9.2	3.4
REBELS-25	228.80	7.306	33.4	17.4
REBELS-27	234.94	7.090	15.8	5.3
REBELS-29	247.31	6.685	11.9	4.0
REBELS-30	238.08	6.983	8.2	<3.3
REBELS-32	245.89	6.729	19.2	4.0
REBELS-34	248.98	6.633	8.5	<3.3
REBELS-36	219.02	7.677	7.8	<3.3
REBELS-38	250.83	6.577	21.2	7.1
REBELS-39	242.19	6.847	9.8	5.2
REBELS-40	227.20	7.365	8.7	3.6

Note.
[a] Based on the peak flux.

well as several additional lower S/N $[C\ II]_{158\ \mu m}$ lines will be presented in S. Schouws et al. (2022, in preparation).

Even if we consider only the $>7\sigma$ line detections in the REBELS data obtained thus far, the program is already having a substantial impact on the number of spectroscopic redshifts derived with ALMA at $z > 6.5$. Figure 11 (top panel) shows how the sources with $\geqslant 7\sigma$ ISM-cooling lines are distributed as a function of redshift and UV luminosity. Also shown in the top panel of Figure 11 are sources from the two pilot programs to REBELS (Smit et al. 2018; Schouws et al. 2022a, 2022b).

As the lower two panels of Figure 11 demonstrate, the number of spectroscopic redshift measurements from ALMA is already fairly similar to that available from similarly significant Lyα lines at $z > 7$, if one makes use of the most significant ISM-cooling line detections from the REBELS program and from the two pilot programs. This is especially the case for the brightest and most massive sources at $z > 6.5$, where the number of redshifts from ALMA already exceeds that available from Lyα by a factor of two.

Simultaneous with the REBELS spectral scans for bright ISM-cooling lines, we are able to probe dust continuum

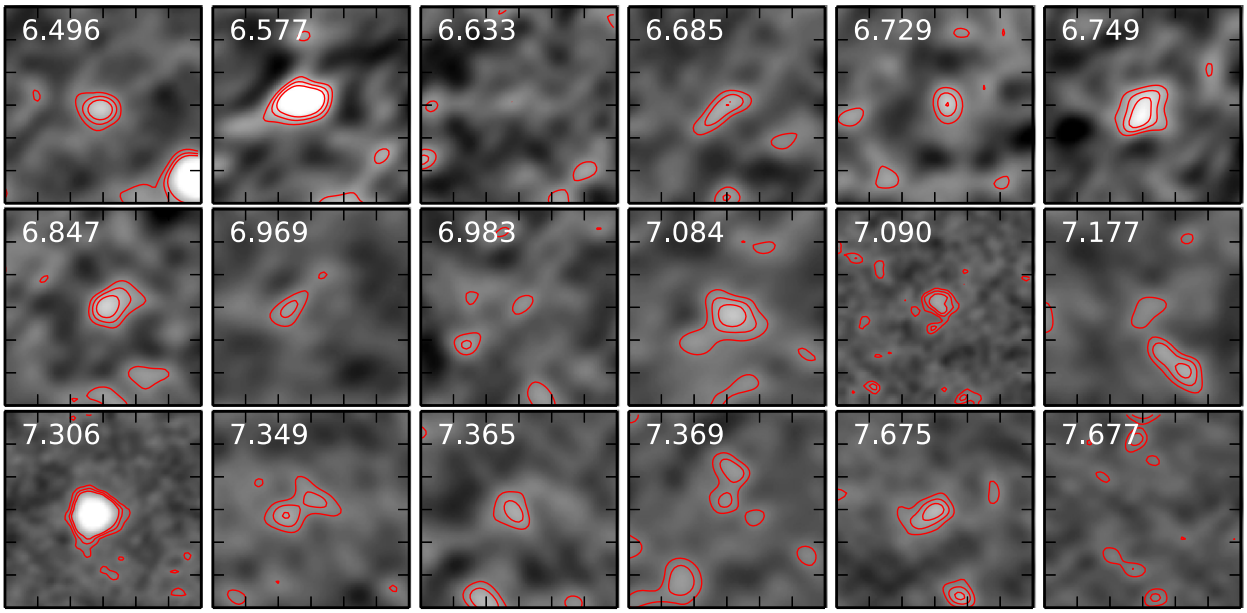

Figure 12. Illustration of the dust-continuum observations available for sources showing $\geqslant 7\sigma$ ISM-cooling line detections in Figure 10. Each stamp is $7\farcs2 \times 7\farcs2$ on a side. The redshifts of the sources are indicated in the upper left corner of each panel. The red contours correspond to 2σ, 3σ, and 4σ. The majority of the sources with highly significant 7σ ISM-cooling line detections (13 out of 18) also show $\gtrsim 3.3\sigma$ detections in the dust continuum. A more detailed characterization of the REBELS targets in the dust continuum will be presented in Inami et al. (2022).

emission from sources in REBELS. Figure 12 shows the continuum observations available for the 18 targets from REBELS with $\geqslant 7\sigma$ ISM-cooling line detections, and it is clear that the majority of these $[\mathrm{C\,II}]_{158\,\mu\mathrm{m}}$-detected sources (13/18) show nominal 3.3σ detections in the dust continuum. These dust-continuum images were generated using the `tclean` task in CASA. Any channels containing emission from the $[\mathrm{C\,II}]_{158\,\mu\mathrm{m}}$ line were excluded when producing the continuum maps. More details on our current dust-continuum results from REBELS will be presented in Inami et al. (2022).

4.2. Effectiveness of the REBELS Spectral Scan Strategy

We can already use the results from the REBELS first-year data to assess the effectiveness of the spectral scan strategy. Perhaps the most relevant variable to utilize in gauging the effectiveness of the scans is in terms of the SFRs of individual targets in our program.

For our SFR estimates for individual sources in the REBELS program, we make use of the luminosities of sources in both the rest-UV and far-IR continuum. The unobscured $\mathrm{SFR_{UV}}$s for sources are estimated based on source UV luminosities using the relation $\mathrm{SFR_{UV}} = 7.1 \times 10^{-29} L_\nu [\mathrm{erg\,s^{-1}\,Hz^{-1}}]$, while the obscured $\mathrm{SFR_{IR}}$s of sources are estimated based on source IR luminosities using the relation $\mathrm{SFR}_{IR} = 1.2 \times 10^{-10} L_{IR}/L_\odot$. The inferred SFRs are $\sim$14% lower for a given UV/IR luminosity than the calibrations adopted for ALPINE (e.g., Schaerer et al. 2020). A detailed motivation and discussion of these relations will be provided in M. Stefanon et al. (2022, in preparation), Topping et al. (2022), and Inami et al. (2022).

In computing the obscured $\mathrm{SFR_{IR}}$ of sources, the IR luminosities of sources L_{IR} are taken to equal $14.2^{+7.6}_{-4.7}\ \nu L_\nu$ where ν is the frequency of the $[\mathrm{C\,II}]_{158\,\mu\mathrm{m}}$ line (Inami et al. 2022; Sommovigo et al. 2022). Using this scaling, sources in REBELS have L_{IR} luminosities ranging from $3 \times 10^{11}\ L_\odot$ to $1 \times 10^{12}\ L_\odot$ (equivalent to obscured SFRs of 36 $M_\odot\,\mathrm{yr^{-1}}$ to 120 $M_\odot\,\mathrm{yr^{-1}}$, respectively). The precise scaling we use here is equivalent to that found from a modified blackbody SED with a dust temperature of 50 K and a dust opacity index β of 1.6. This is a slightly higher dust temperature than ALPINE use in the analysis of their $z = 4$–6 sample (Béthermin et al. 2020), but lower than is found by Bouwens et al. (2020) in modeling the dust temperature versus redshift measurements available at the time. It is also consistent with the general range of dust temperatures found by semi-analytical models (Sommovigo et al. 2022) and numerical simulations (R. Schneider et al. 2022, in preparation) for REBELS-like sources. A more extensive motivation for these conversion factors will be provided in Inami et al. (2022).

Using the above scalings to estimate the SFRs of individual sources, we present the number of sources showing prominent ISM-cooling line detections as a function of the total SFR of sources in Figure 13. We only include in the analysis the 32 sources for which our ISM-cooling line scans are complete and which appear to be securely at $z > 6$.[29] Since only one of our $[\mathrm{O\,III}]_{88\,\mu\mathrm{m}}$ spectral scans is complete to present in the first-year data, it makes sense to frame these search results in terms of our spectral scans for $[\mathrm{C\,II}]_{158\,\mu\mathrm{m}}$.

Looking over the results, our spectral scans for $[\mathrm{C\,II}]_{158\,\mu\mathrm{m}}$ show a dramatic increase in efficiency above 28 $M_\odot\,\mathrm{yr^{-1}}$. Fifteen of the 19 sources with SFRs in excess of 28 $M_\odot\,\mathrm{yr^{-1}}$, i.e., 79%, show prominent 7σ ISM-cooling lines in the observations taken to date. Meanwhile, below an SFR of

[29] Significantly deeper Spitzer/IRAC observations became available for REBELS-10 following the selection of targets for the REBELS program (Stefanon et al. 2019a). Using the new photometry, REBELS-10 now appears to be more likely at $z < 6$ than at $z > 6$. In addition to REBELS-10, there are also concerns about the robustness of REBELS-13, given the formal integrated likelihood of its being at $z < 6$ and its lacking a red [3.6]−[4.5] color, as is typical for star-forming galaxies in the redshift range $z = 7.0$–9.1 due to the $[\mathrm{O\,III}]_{4959,5007}$+H$\beta$ emission lines (Roberts-Borsani et al. 2016). M. Stefanon et al. (2022, in preparation) will discuss each of these cases in more detail.

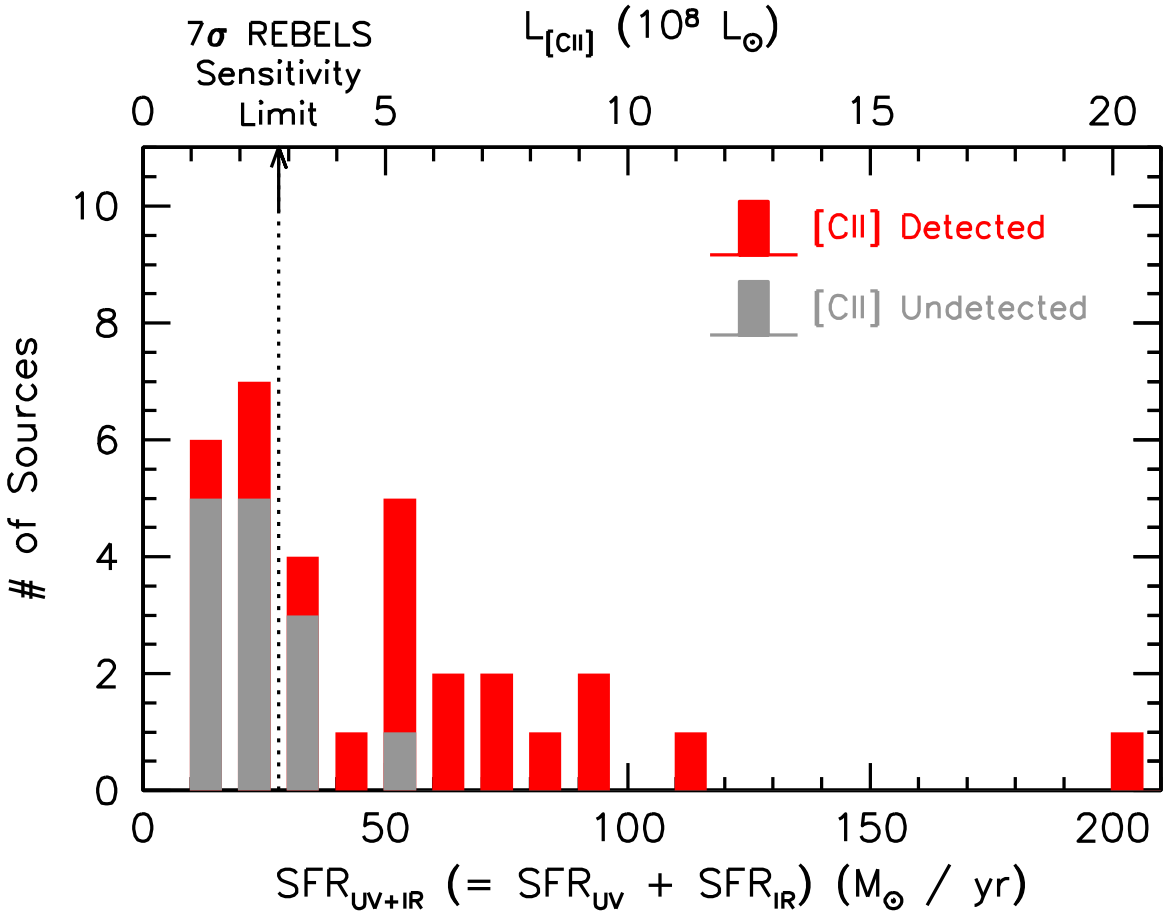

Figure 13. Number of sources with $[\mathrm{C\,II}]_{158\,\mu\mathrm{m}}$ detected (red histograms) at 7σ versus $\mathrm{SFR_{UV+IR}}$ ($=\mathrm{SFR_{UV}}+\mathrm{SFR_{IR}}$). The gray histograms indicate the number of sources where $[\mathrm{C\,II}]_{158\,\mu\mathrm{m}}$ is yet to be detected at 7σ in the REBELS program. Only sources where the spectral scans are complete—and where sources are considered to be securely at $z>6$—are included in the numbers. The upper horizontal axis shows the $[\mathrm{C\,II}]_{158\,\mu\mathrm{m}}$ luminosity that is equivalent to a given $\mathrm{SFR_{UV+IR}}$s using the $z\sim0$ $L_{[\mathrm{C\,II}]_{158\,\mu\mathrm{m}}}$–SFR relation from De Looze et al. (2014). Our prescriptions for computing $\mathrm{SFR_{UV}}$ and $\mathrm{SFR_{IR}}$ are given in Section 4.2. The detection rate of $[\mathrm{C\,II}]_{158\,\mu\mathrm{m}}$ shows a dramatic increase at SFRs higher than 28 $M_\odot\,\mathrm{yr}^{-1}$ (equivalent to the approximate luminosity limit for searches for $[\mathrm{C\,II}]_{158\,\mu\mathrm{m}}$ in REBELS adopting a 7σ detection threshold, i.e., $2.8\times10^8 L_\odot$ [Figure 7]).

28 $M_\odot\,\mathrm{yr}^{-1}$, only three of 13 sources show a prominent 7σ $[\mathrm{C\,II}]_{158\,\mu\mathrm{m}}$ detection. We note that the 7σ limiting luminosity for $[\mathrm{C\,II}]_{158\,\mu\mathrm{m}}$ scans in the REBELS program (Figure 7), $2.8\times10^8\,L_\odot\,\mathrm{yr}^{-1}$, is equivalent to an SFR threshold of 28 $M_\odot\,\mathrm{yr}^{-1}$, using the $z\sim0$ relation from De Looze et al. (2014). This result is suggestive of only minimal evolution in the $[\mathrm{C\,II}]_{158\,\mu\mathrm{m}}$–SFR relation to $z\sim0$ (see also Matthee et al. 2017, 2019; Carniani et al. 2018, 2020; Harikane et al. 2020; Schaerer et al. 2020).

We also note that some sources with SFRs higher than 28 $M_\odot\,\mathrm{yr}^{-1}$ remain undetected in $[\mathrm{C\,II}]_{158\,\mu\mathrm{m}}$, while some sources below 28 $M_\odot\,\mathrm{yr}^{-1}$ are detected. This is suggestive of there being some intrinsic scatter in the $L_{[\mathrm{C\,II}]_{158\,\mu\mathrm{m}}}$ versus SFR relation at $z\sim7$, similar to the 0.27 dex scatter observed at $z\sim0$ by De Looze et al. (2014). We will further characterize both the evolution and the scatter in the $L_{[\mathrm{C\,II}]_{158\,\mu\mathrm{m}}}$ versus SFR relation in S. Schouws et al. (2022, in preparation).

It is also interesting to present the efficiency of our $[\mathrm{C\,II}]_{158\,\mu\mathrm{m}}$ scans in terms of the unobscured SFRs for sources. Figure 14 shows the number of sources where $[\mathrm{C\,II}]_{158\,\mu\mathrm{m}}$ is prominently detected ($>7\sigma$: red histogram) as a function of the unobscured SFRs, and also the number of sources where no prominent $[\mathrm{C\,II}]_{158\,\mu\mathrm{m}}$ emission is found (gray histogram). While the $[\mathrm{C\,II}]_{158\,\mu\mathrm{m}}$ detection fraction does show some dependence on the unobscured $\mathrm{SFR_{UV}}$s, the dependence is significantly less steep than on the total $\mathrm{SFR_{UV+IR}}$s (Figure 13). This demonstrates the essential value ALMA observations have for characterizing the ISM of star-forming galaxies at $z>6.5$.

We emphasize that only the most prominent $[\mathrm{C\,II}]_{158\,\mu\mathrm{m}}$ detections from the REBELS program are included here in evaluating the efficiency of the spectral scans. There are indeed a larger number of $[\mathrm{C\,II}]_{158\,\mu\mathrm{m}}$ detections in REBELS, but these detections require a more careful demonstration of their robustness. These line detections will be presented in detail in S. Schouws et al. (2022, in preparation).

5. Science Objectives

In facilitating the construction of a significant sample of especially luminous ISM reservoirs in the $z>6.5$ universe, the REBELS Large Program enables us to pursue a wide variety of different scientific objectives.

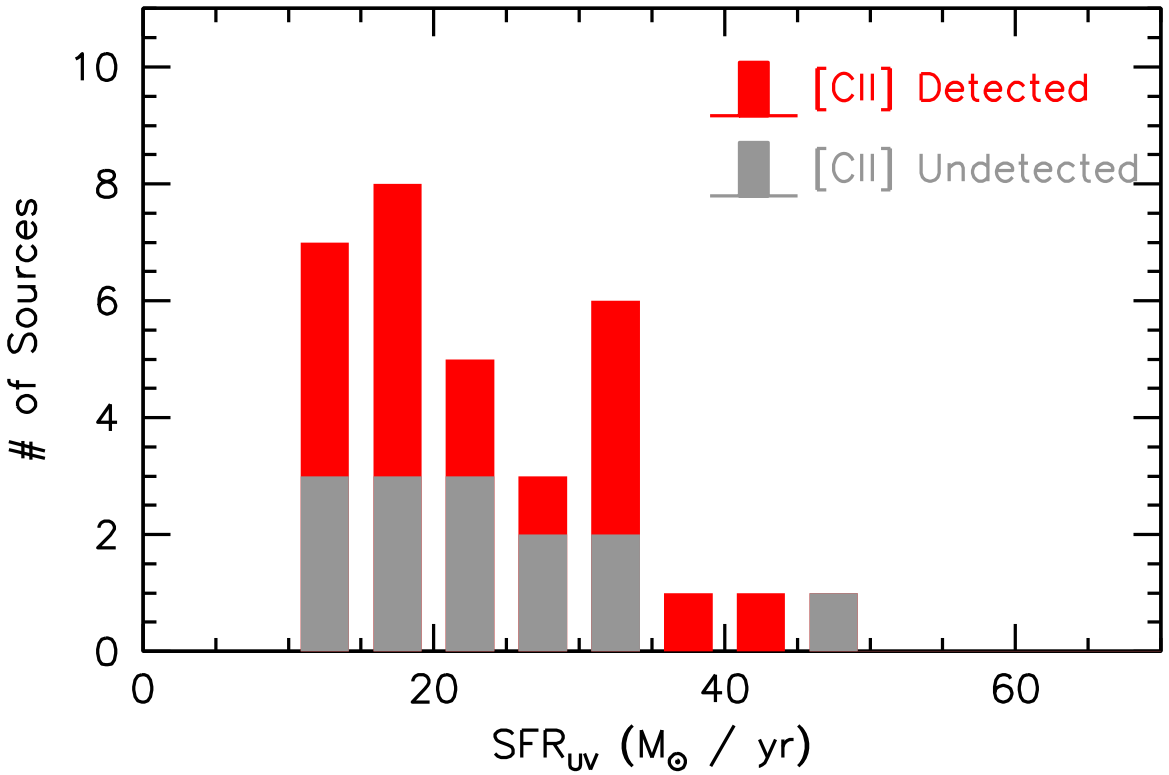

Figure 14. Similar to Figure 13, but as a function of the unobscured SFR_{UV}. While the $[C\,II]_{158\ \mu m}$-detected fraction of sources in REBELS does show some dependence on SFR_{UV}, the dependence is significantly weaker than on SFR_{UV+IR} (Figure 13). This demonstrates the essential value that ALMA observations have in helping us to characterize the ISM of star-forming galaxies at $z > 6.5$.

These include the following:

Significantly expand the overall number of sources in current spectroscopic samples at $z \gtrsim 7$: Based on the success rate of observations from various pilot programs (Hashimoto et al. 2018; Smit et al. 2018; Schouws et al. 2022b), REBELS is providing new redshift measurements for 25–30 galaxies at $z \sim 7$–9 in the reionization epoch, almost tripling the number of such measurements available now with ALMA at $z > 7$. See histograms in the lower two panels of Figure 11. In addition to the increase in numbers, the new spectroscopic redshifts we are obtaining with ALMA sample much more massive sources than have generally been identified thus far with rest-UV lines like Lyα.

Probe the emergence of dust in bright, massive $z > 6.5$ *galaxies:* REBELS is providing a sensitive probe of dust-continuum emission in $z > 6$ galaxies, due to our scan strategy for finding $[C\,II]_{158\ \mu m}$+$[O\,III]_{88\ \mu m}$ line emission. As Figure 9 shows, our scan strategy allows us to observe faint enough in the far-IR continuum to probe dust growth over most of the reionization era, effectively providing the community with a $z = 6$–10 extension to $z = 4$–6 results from ALPINE (Béthermin et al. 2020; Faisst et al. 2020; Le Fevre et al. 2020). Probing dust emission in $z > 7$ galaxies is very interesting, given the huge uncertainties that exist regarding the origin and production of early dust in the universe. In particular, both the relative contribution of dust creation from high-z supernovae (SNe) or Asymptotic Giant-branch (AGB) stars, as well as grain growth and dust destruction, are poorly constrained and continue to be actively debated (e.g., Mancini et al. 2015; Michaowski 2015; Popping et al. 2017; Graziani et al. 2020). Of considerable interest to such discussions has been the detection and IR luminosities of $z > 6$ galaxies like A1689-zD1 ($z \sim 7.5$: Watson et al. 2015; Knudsen et al. 2017) and A2744 YD4 ($z = 8.38$: Laporte et al. 2017), which have been argued to show too much dust mass/emission to match most models (e.g., Mancini et al. 2015; Michaowski 2015). One exception is Behrens et al. (2018), who reproduced the observed SED from their simulations (Pallottini et al. 2017), finding an SFR ≈ 4 higher than deduced from SED fitting by Laporte et al. (2017), as well as a low dust-to-metal ratio (implying inefficient early dust formation) and higher dust temperatures (as high as Td ~ 91 K; see, e.g., Ferrara et al. 2016, 2022; Sommovigo et al. 2020, 2021). Whatever the resolution of this issue, REBELS is allowing for a characterization of the build-up of dust in galaxies, based on comparisons it allows from galaxies at $z \sim 8.5$–9.5 to $z \sim 6$, 7, and 8 (Dayal et al. 2022; Inami et al. 2022; R. Schneider et al. 2022, in preparation).

Follow-up of bright sources from our sample should allow for a definitive measurement of the dust temperature, the emissivity, as well as evolution in the IRX-β relation, and the evolution of these quantities with cosmic time. This will be valuable for determining whether the dust temperatures of galaxies evolve strongly in the first two billion years of the universe (Béthermin et al. 2015; Bouwens et al. 2020; Schreiber et al. 2018) or whether the evolution is relatively mild (Faisst et al. 2020). The REBELS probe of the dust content in galaxies is also allowing for a definitive determination of the obscured SFR density in UV bright galaxies in the Epoch of Reionization as well as a search for highly dust

obscured galaxies in the immediate neighborhood of the UV-bright population, as was recently reported in Fudamoto et al. (2021) using the REBELS data set. This will allow for an investigation into whether the cosmic star formation rate density flattens, as found in FIR and radio observations dusty UV-obscured systems (Novak et al. 2017; Gruppioni et al. 2020; Talia et al. 2021).

Provide first significant probe of the high-luminosity End of the IR and [C II]$_{158\,\mu m}$ luminosity functions in the reionization epoch: Using the luminosities of the [C II]$_{158\,\mu m}$ lines we detect in REBELS and volume densities of the UV samples from which our targets are drawn, we have derived the first significant [C II]$_{158\,\mu m}$ and IR luminosity functions at $z > 6$ at the high-luminosity end, which provide a valuable constraint for theoretical models that look at [C II]$_{158\,\mu m}$ emission from galaxies (e.g., Vallini et al. 2015, 2017, 2020; Katz et al. 2017; Olsen et al. 2017; Pallottini et al. 2017, 2019; Popping et al. 2017; Lagache et al. 2018; Kohandel et al. 2019; Arata et al. 2020). Having constraints on the IR luminosity function provides us with a direct pathway to compute the SFR function itself ($= \mathrm{SFR_{UV}} + \mathrm{SFR_{IR}}$) at $z > 6.5$.

Rest-optical emission line EWs, stellar masses, specific star formation rates, and the galaxy stellar-mass function at $z \sim 7$: Our estimates on the stellar masses of $z > 6$ galaxies are poor due to the impact of very strong optical nebular line emission, which has a huge (factor of $\sim$1.7) impact on observed 3–5 μm fluxes of galaxies at $z > 6$ (e.g., Schaerer & de Barros 2009; Raiter et al. 2010; Stark et al. 2013; Smit et al. 2014; Roberts-Borsani et al. 2016). Our ALMA scans give us the precise redshift of sources, enabling us to model the impact of line emission on the Spitzer/IRAC fluxes much more precisely. These data are thus allowing us to dramatically improve the robustness of the high-mass end of the galaxy stellar mass function at $z \sim 7$.

Dynamical mass estimates: To reveal the physics behind early massive galaxy build-up, we have derived dynamical mass estimates from the emission-line widths of our sample (following, e.g., Capak et al. 2015). These estimates can then be related to the stellar mass estimates that we can uniquely derive for this sample, allowing us to investigate if the stellar mass in these early galaxies builds up smoothly as their gas reservoirs grow or if feedback processes plays a significant role in the conversion from gas to stars, based on the scatter in the stellar-to-dynamical mass ratio.

Major mergers and rotation-dominated systems: Our observations also provide robust detections of the [C II]$_{158\,\mu m}$ or [O III]$_{88\,\mu m}$ lines in our galaxies, which reveal if major mergers are ongoing in our sources by fitting for double-peaked line profiles (such as observed by Willott et al. 2015 and Matthee et al. 2017). We compare the major merger rate found in our program with recent HST imaging analyses of major merger rates between redshift $1 < z < 7$ (e.g., Duncan et al. 2019), which suggest a steady increase in the major merger rate with redshift, such that at $z > 6$ roughly $\sim$50% of galaxy growth is contributed by merger activity (however, see also Dayal et al. 2013). We test these claims in a statistically significant sample at $z \gtrsim 7$, using the first such analysis from spectroscopy.

Furthermore, we have performed a Briggs-weighted analysis of the data to investigate the low-resolution kinematics of our sources and derive velocity gradients (following, e.g., Smit et al. 2018). Förster Schreiber et al. (2009) estimate the level of rotational support in a galaxy based on the observed velocity gradient and the integrated velocity dispersion of the source, defining $v_{\rm obs}/2\sigma_{\rm int} > 0.4$ as rotation-dominated systems. Using sources with single-peaked line profiles and monotonically rising velocity gradients (i.e., sources without major mergers), we aim to obtain a census of the rotation-dominated fraction of the $z \gtrsim 7$ galaxy population.

Outflows and [C II]$_{158\,\mu m}$ halos: We have performed a stacking analysis of [C II]$_{158\,\mu m}$ (in the *uv* plane) to reveal the low surface brightness components of [C II]$_{158\,\mu m}$ and search for broad line emission in the stacked spectra. By comparing the outflow velocities to SFRs, dynamical, and stellar masses, we are investigating if outflow velocities increase with redshift to $z \sim 7$, as has been found at $z \sim 0$–2 (e.g., Sugahara et al. 2019). Recent observations furthermore suggest that diffuse and extended "[C II]$_{158\,\mu m}$ halos" might be present in $z \sim 3$–7 star-forming galaxies (Fujimoto et al. 2019; Rybak et al. 2019; Herrera-Camus et al. 2021). Our stacking analysis can reveal if such diffuse components are ubiquitous in the earliest galaxies, providing the first insight into the physical properties of the circumgalactic medium at $z \gtrsim 7$.

Legacy value: REBELS is explicitly designed to deliver a large sample of very high-luminosity [C II]$_{158\,\mu m}$ and [O III]$_{88\,\mu m}$-emitting galaxies at $z \gtrsim 7$, at a modest cost. The REBELS line emitters are prime targets for deep spectroscopic follow-up with JWST, given the clear value of these galaxies for understanding the early build-up of luminous ISM reservoirs, and in fact, one such program has been approved for execution in cycle 1 (Stefanon et al. 2021). Additionally, the identification of such line emitters is absolutely essential for future work probing the kinematics of $z \gtrsim 7$ galaxies at high resolution. This will be essential for robustly discriminating between rotation-dominated galaxies and those undergoing mergers—which can be degenerate for some choices of parameters at the REBELS spatial resolution.

Furthermore, the characterization of the physical conditions of the gas in high-redshift galaxies through observations of [N II]$_{205\mu m}$, [N II]$_{122\,\mu m}$, [C I]/CO, [O III]$_{52\,\mu m}$, or [O I]$_{63\mu m}$/[O I]$_{146\,\mu m}$ is only feasible for the brightest galaxies in the Epoch of Reionization. New systemic redshift measurements from REBELS would have great value for studies of low-S/N rest-UV lines in these bright galaxies (including constraints on the neutral hydrogen fraction of the IGM, based on the declining prevalence of Lyα as a function of redshift), as is presented, e.g., in Endsley et al. (2022). After shifting to a common rest-frame wavelength, archival/future spectra of these galaxies can be immediately stacked.

6. Summary

The purpose of this paper is to summarize the scientific motivation, observational strategy, and sample selection of the 70 hr Reionization Era Bright Emission Line Survey (REBELS) ALMA Large Program (2019.1.01634.L), while showcasing some of the most exciting initial results from the program.

The motivation for the REBELS program has been to construct and to perform a first characterization of a significant sample of especially luminous ISM reservoirs in the $z > 6.5$ universe. To achieve this, REBELS has been systematically scanning 40 of the brightest $z > 6.5$ galaxies identified over 7 deg^2 for bright ISM-cooling lines, while probing dust-continuum emission from the same sources.

The utility of targeting UV-bright galaxies with ALMA has become increasingly clear from work over the past few years, with many of the brightest ISM-cooling lines at $z > 4$ being present among the bright population (Capak et al. 2015; Willott et al. 2015; Smit et al. 2018; Matthee et al. 2019; Béthermin et al. 2020; Harikane et al. 2020; Schouws et al. 2022b). In fact, 79% of the sources with SFRs of >28 $M_\odot$ yr^{-1} show $\geqslant 7\sigma$ [C II]$_{158\ \mu m}$ lines, which, given the typical sensitivities of the REBELS spectral scans, would give the sources [C II]$_{158\ \mu m}$ luminosities in excess of 2.8×10^8 $L_\odot$ (Figure 1).

To maximize the impact of the REBELS program, considerable effort was thus devoted toward targeting the brightest and most robust selection of $z > 6.5$ galaxies visible to ALMA (Section 2). The use of targets from at least eight different high-redshift selections (e.g., Bowler et al. 2014, 2017, 2020; Stefanon et al. 2017b, 2019a, Endsley et al. 2021a, 2022; M. Stefanon et al. 2022, in preparation) was considered. For each potential target, photometry was done independently by at least three different members of the REBELS team, and redshift likelihood distributions were derived from three independent codes. Targets were then ranked according to their brightness and robustness, and ultimately the likelihood of detecting an ISM-cooling line in a spectral scan. Only the highest ranked sources were included in our final set of 40 targets.

Consideration was given both to spectral scans targeting the 157.74 μm [C II] line and 88.36 μm [O III] line for the REBELS program. We computed the limiting luminosity to which we could probe each line as a function of redshift to assess the relative efficiency. After considering the line ratios observed for $z > 6$ galaxies in the literature (Figure 6), we decided that the [C II]$_{158\ \mu m}$ line would be the best choice for executing line scans out to $z \sim 8.5$ and that the [O III]$_{88\ \mu m}$ line would be the best choice for sources with likely redshifts above $z \sim 8.5$ (Section 3.1).

For each target in our sample, we set up the tunings for our spectral scans to cover the bulk of the redshift likelihood distribution for each source (typically >80%–90%). Results obtained from three independent sets of photometry were used in deriving this likelihood distribution (Section 3.2). With one, two, or three tunings, we can cover contiguous frequency ranges of 5.375 GHz, 10.75 GHz, or 20.375 GHz, respectively, if the spectral scan is in band 6. We have arranged the tunings for sources to optimize the number of ISM-cooling lines we can detect for a ~70 hr ALMA allocation. Appendix A illustrates in detail the layout of the tunings that make up the spectral scans for the 40 targets in our program.

The integration time for each tuning is set by the requirement that we detect a 3×10^8 $L_\odot$ [C II]$_{158\ \mu m}$ line at 5σ when executing our band-6/5 scans and a 1.1×10^9 $L_\odot$ [O III]$_{88\ \mu m}$ line at 5σ when executing our band-7 scans. Those sensitivity requirements translated into ~20 minute integration times for REBELS [C II]$_{158\ \mu m}$ searches to $z \sim 7.2$, ~30–40 minute integration times for [C II]$_{158\ \mu m}$ searches to $z \sim 8.5$, and ~20–40 minute integration times in searches for the [O III]$_{88\ \mu m}$ line at $z > 8.2$.

Simultaneous with the REBELS scans for [C II]$_{158\ \mu m}$ and [O III]$_{88\ \mu m}$, REBELS probes the IR luminosities of our targets based on their dust-continuum emission. Given the poorer sensitivity of REBELS for dust continuum (Figure 8), our use of multiple spectral scan tunings to search for ISM-cooling lines really does provide an advantage in allowing us to probe the dust continuum. As shown in Figure 9, REBELS probes to 3×10^{11} $L_\odot$ in galaxies out to $z \sim 7.2$. At $z > 7.2$, it probes even deeper to 2×10^{11} $L_\odot$. This is equivalent to probing to obscured SFRs of 36 $M_\odot$ yr^{-1} and 24 $M_\odot$ yr^{-1}, respectively.

During the first year of observations from the REBELS program (2019 November–2020 January), 60.6 out of the total 69.6 hr allocated to REBELS have been executed. A search for prominent cooling lines in the data revealed 18 prominent $\geqslant 7\sigma$ [C II]$_{158\ \mu m}$ lines (Figure 10 and Table 2). No especially significant $\geqslant 7\sigma$ [O III]$_{88\ \mu m}$ lines have been identified in the existing data from the REBELS program, but observations are complete for only one of four sources using [O III]$_{88\ \mu m}$ scans. The majority of the sources showing $\geqslant 7\sigma$ detections of [C II]$_{158\ \mu m}$ (13/18) also show $\geqslant 3.3\sigma$ dust-continuum emission (Figure 12). Remarkably, adding the newly identified [C II]$_{158\ \mu m}$ lines to those from the literature and pilot programs to REBELS (Smit et al. 2018; Schouws et al. 2022b), the number of redshift determinations from ALMA is already starting to be comparable to the number of Lyα-derived redshifts at $z > 7$ (Figure 11).

It is interesting to already be able to make use of the prominent 7σ [C II]$_{158\ \mu m}$ line detections to quantify the efficiency of spectral scans with ALMA. Looking specifically at the fraction of [C II]$_{158\ \mu m}$ -detected galaxies as a function of their total SFR, we find a dramatic increase in the fraction above a SFR of 28 $M_\odot$ yr^{-1} (Figure 13). Fifteen of the 19 sources with SFRs in excess of 28 $M_\odot$ yr^{-1}, i.e., 79%, show prominent 7σ [C II]$_{158\ \mu m}$ -cooling lines in the observations taken to date. Meanwhile, below an SFR of 28 $M_\odot$ yr^{-1}, only three of 13 sources show a prominent [C II]$_{158\ \mu m}$ detection. We note that an SFR threshold of 28 $M_\odot$ yr^{-1} corresponds to a [C II]$_{158\ \mu m}$ luminosity of 2.8×10^8 $L_\odot$ using the $z \sim 0$ De Looze et al. (2014) relation. Since 2.8×10^8 $L_\odot$ is also the approximate 7σ limit for our [C II]$_{158\ \mu m}$ scans in the REBELS program (Figure 7), this is suggestive of minimal evolution in the [C II]$_{158\ \mu m}$–SFR relation from $z \sim 8$ to $z \sim 0$, as Schaerer et al. (2020) also conclude on the basis of the ALPINE program (see also Matthee et al. 2017, 2019; Carniani et al. 2018, 2020; Harikane et al. 2020).

In this paper, we have presented the motivation, observational strategy, and some initial observational results from a cycle-7 ALMA large program known as REBELS. In the future, we look forward to the completion of spectral scans for the final six targets in the program, the bulk of which probe galaxies at $z \geqslant 8$. Also of considerable importance will be an exciting array of follow-up observations being acquired on targets from our program, including from JWST, JVLA, ALMA, Keck, and the VLT.

We would like to acknowledge our collaborators on the BoRG project, Joanna Bridge, Benne Holwerda, and Michele Trenti, for the collective work done on the identification and characterization of sources from pure parallel HST programs. This allowed for the inclusion of Super8-1 in the present selection. We would like to thank Jorryt Matthee for useful conversations related to the redshift scan range for 1–2 sources from the REBELS selection. This paper is based on data obtained with the ALMA Observatory, under the Large Program 2019.1.01634.L. ALMA is a partnership of ESO (representing its member states), NSF (USA), and NINS (Japan), together with NRC (Canada), MOST and ASIAA (Taiwan), and KASI (Republic of Korea), in cooperation with

the Republic of Chile. The Joint ALMA Observatory is operated by ESO, AUI/NRAO and NAOJ. R.J.B. and M.S. acknowledge support from TOP grant TOP1.16.057. S.S. acknowledges support from the Nederlandse Onderzoekschool voor Astronomie (NOVA). R.S. and R.A.B. acknowledge support from STFC Ernest Rutherford Fellowships [grant numbers ST/S004831/1 and ST/T003596/1]. R.E. acknowledges funding from JWST/NIRCam contract to the University of Arizona, NAS5-02015. P.A.O., L.B., and Y.F. acknowledge support from the Swiss National Science Foundation through the SNSF Professorship grant 190079 "Galaxy Build-up at Cosmic Dawn." H.I. and H.S.B.A. acknowledge support from the NAOJ ALMA Scientific Research Grant Code 2021-19A. H.I. acknowledges support from the JSPS KAKENHI grant No. JP19K23462. J.H. gratefully acknowledges support of the VIDI research program with project number 639.042.611, which is (partly) financed by the Netherlands Organisation for Scientific Research (NWO). M.A. acknowledges support from FONDECYT grant 1211951, "CONICYT + PCI + INSTITUTO MAX PLANCK DE ASTRONOMIA MPG190030" and "CONICYT +PCI+REDES 190194". P.D. acknowledges support from the European Research Council's starting grant ERC StG-717001 ("DELPHI"), from the NWO grant 016.VIDI.189.162 ("ODIN"), and the European Commission's and University of Groningen's CO-FUND Rosalind Franklin program. L.G. and R.S. acknowledge support from the Amaldi Research Center funded by the MIUR program "Dipartimento di Eccellenza" (CUP:B81I18001170001). Y.F. further acknowledges support from NAOJ ALMA Scientific Research grant no. 2020-16B "ALMA HzFINEST: High-z Far-Infrared Nebular Emission STudies." A.F. acknowledges support from the ERC Advanced Grant INTERSTELLAR H2020/740120. Any dissemination of results must indicate that it reflects only the authors' views and that the Commission is not responsible for any use that may be made of the information it contains. Partial support from the Carl Friedrich von Siemens-Forschungspreis der Alexander von Humboldt-Stiftung Research Award is kindly acknowledged (A.F.). I.D.L. acknowledges support from ERC starting grant 851622 DustOrigin. J.W. acknowledges support from the ERC Advanced grant 695671, "QUENCH", and from the Fondation MERAC. This paper utilizes observations obtained with the NASA/ESA Hubble Space Telescope, retrieved from the Mikulski Archive for Space Telescopes (MAST) at the Space Telescope Science Institute (STScI). STScI is operated by the Association of Universities for Research in Astronomy, Inc. under NASA contract NAS 5-26555. This work is based [in part] on observations made with the Spitzer Space Telescope, which was operated by the Jet Propulsion Laboratory, California Institute of Technology under a contract with NASA. Support for this work was provided by NASA through an award issued by JPL/Caltech.

Software: lephare (Arnouts et al. 1999; Ilbert et al. 2006), CASA (v5.6.1; McMullin et al. 2007), eazy (Brammer et al. 2008), beagle (Chevallard & Charlot 2016).

Appendix A
Spectral Scan Windows

The purpose of this appendix is to summarize the tunings utilized by REBELS in scanning for $[\mathrm{C\,II}]_{158\,\mu\mathrm{m}}$ and $[\mathrm{O\,III}]_{88\,\mu\mathrm{m}}$ in the 40 $z > 6.5$ galaxies the LP targeted.

Figures 15 and 16 show the complete set of tunings used in scanning for the $[\mathrm{C\,II}]_{158\,\mu\mathrm{m}}$ and $[\mathrm{O\,III}]_{88\,\mu\mathrm{m}}$ ISM-cooling lines. Also shown are the redshift likelihood distributions derived for each target, which are identical to those presented earlier in Figure 2 with the thick black lines.

Also shown in Figure 15 are the redshift likelihood distributions for two sources REBELS-04 and REBELS-37 derived including one-orbit HST F105W, 3/4 orbit F125W, and 5/4 orbit F160W observations from a two-orbit program led by Rebecca Bowler (GO 15931) and a four-orbit program led by Mauro Stefanon (GO 16879).

With the exception of four targets in our program (REBELS-04, REBELS-11, REBELS-13, and REBELS-37) where the bulk of the redshift likelihood distribution is $z > 8$, the $[\mathrm{C\,II}]_{158\,\mu\mathrm{m}}$ line is targeted with the REBELS spectral scans. For REBELS-04, REBELS-11, and REBELS-13, the $[\mathrm{O\,III}]_{88\,\mu\mathrm{m}}$ line is targeted. For REBELS-37, both the $[\mathrm{C\,II}]_{158\,\mu\mathrm{m}}$ line (at $z < 8$) and $[\mathrm{O\,III}]_{88\,\mu\mathrm{m}}$ line (at $z > 8$) are targeted as part of the spectral scans.

Following the first year of observations from the REBELS program and successful detection of the $[\mathrm{C\,II}]_{158\,\mu\mathrm{m}}$ ISM-cooling line in REBELS-18 and REBELS-36, several tunings from REBELS-18 and REBELS-36 were shifted to REBELS-06, REBELS-16, and REBELS-37 to extend the redshift range of spectral scans for $[\mathrm{C\,II}]_{158\,\mu\mathrm{m}}$ in these sources.

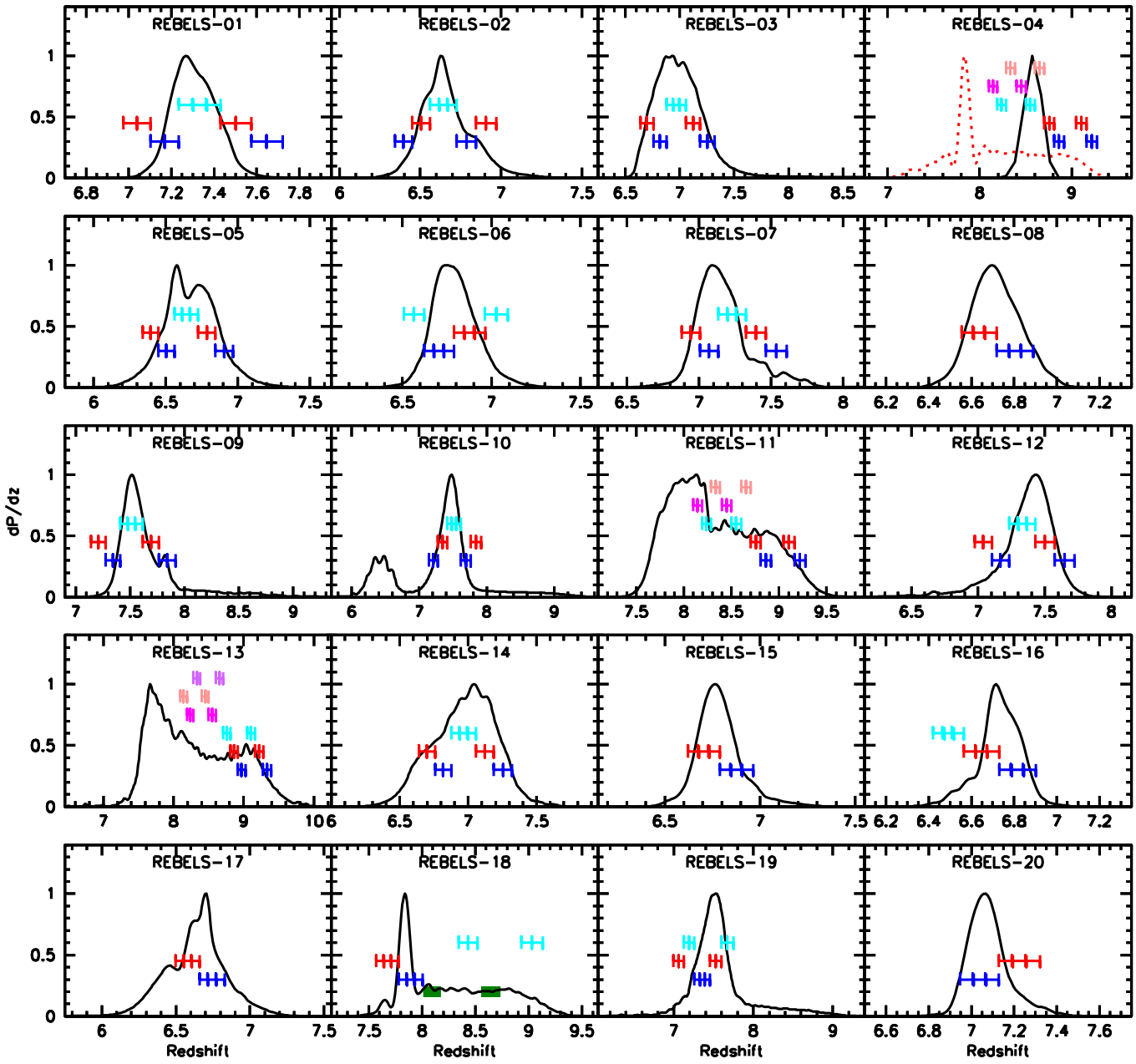

Figure 15. Spectral scan windows used to search $[\mathrm{C\,II}]_{158\,\mu\mathrm{m}}$ and $[\mathrm{O\,III}]_{88\,\mu\mathrm{m}}$ in REBELS sources 1 through 20. The black lines show the redshift likelihood distributions we derive combining the six separate redshift likelihood distributions we derived for each source (e.g., see Figure 2). The dotted red lines show the redshift likelihood distributions derived before including the HST F105W, F125W, and F160W observations from GO 15931 (PI: Bowler) and GO 16879 (PI: Stefanon). Scans are for $[\mathrm{C\,II}]_{158\,\mu\mathrm{m}}$ except in the case of REBELS-04, REBELS-11, and REBELS-13, where the scans are for $[\mathrm{O\,III}]_{88\,\mu\mathrm{m}}$. The green horizontal bars indicate the redshift range probed by previous ALMA observations (Bowler et al. 2018; Schouws et al. 2022a, 2022b).

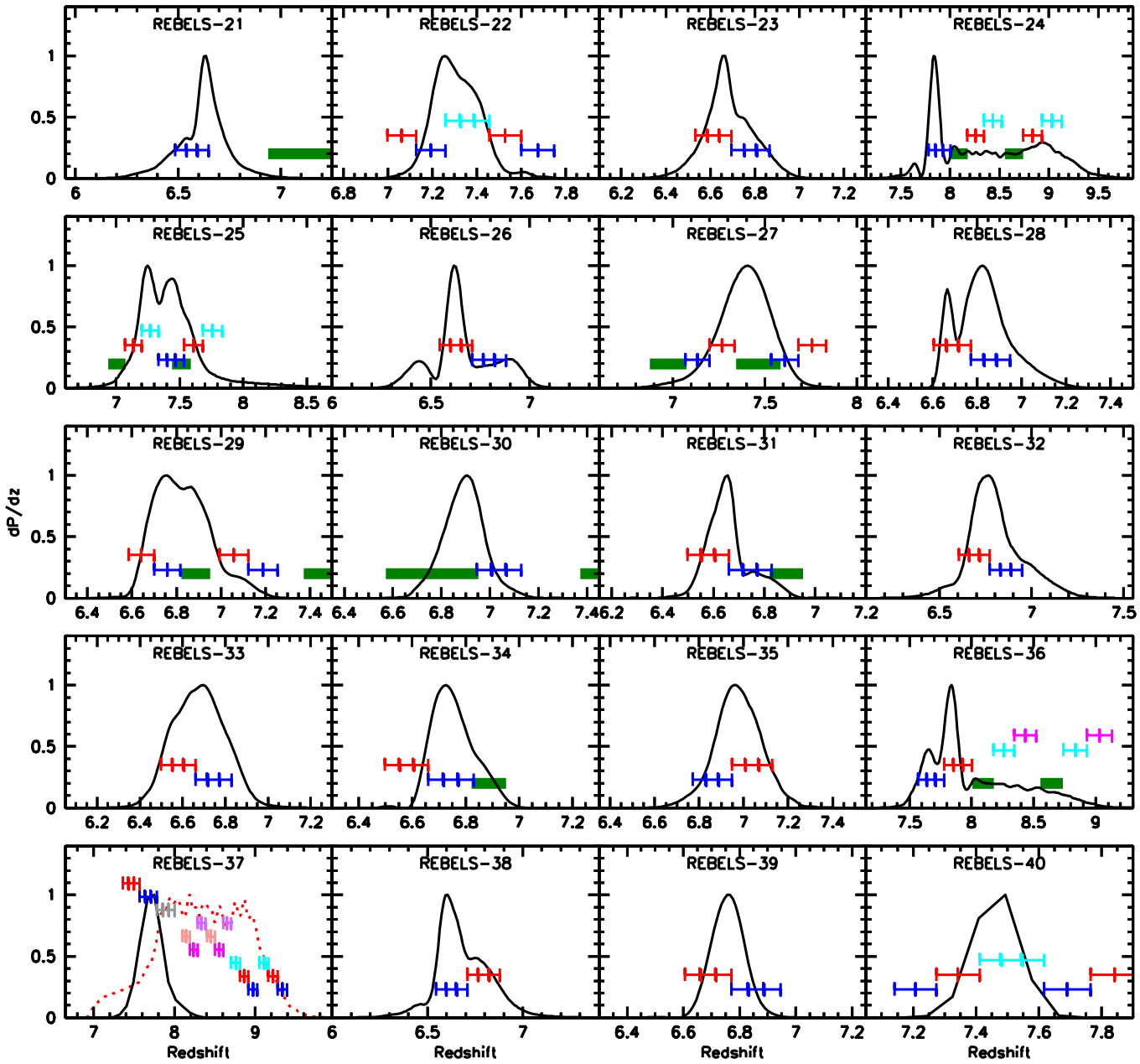

Figure 16. As in Figure 15, but for REBELS sources 21 through 40. Scans are for [C II]$_{158\ \mu m}$ except in the case of REBELS-37 where the scan is for [O III]$_{88\ \mu m}$ at z>8, but for [C II]$_{158\ \mu m}$ at z<8.

Appendix B
Distribution of the REBELS Sample in Parameter Space

The purpose of Appendix B is to illustrate the distribution of REBELS targets in parameter space. Figure 17 shows the stellar mass distribution of sources in the REBELS sample inferred using BEAGLE, and compares it against the stellar mass distribution inferred for ALPINE (Faisst et al. 2020). Overall, the two distributions span a fairly similar mass range.

The median stellar mass we estimate for the REBELS sample from BEAGLE is $10^{9.25}$ $M_{\odot}$ (shown in Figure 17 as a filled downward-pointing orange triangle) assuming a constant star formation rate, while using PROSPECTOR (M. Stefanon et al. 2022, in preparation), the median stellar mass we estimate is $10^{9.8}$ $M_{\odot}$ (shown in Figure 17 as an open downward-pointing orange triangle). These masses are ∼0.4 dex lower and ∼0.1 dex higher, respectively, than those inferred by Faisst et al. (2020) for ALPINE.

Figure 18 shows the distribution of galaxies in redshift, UV luminosity, UV-continuum slope β, and [O III]$_{4959,5007}$+Hβ EW. The EW distribution shown in the lower right panel is derived using a procedure similar to that used by Endsley et al. (2021a) to derive [O III]$_{4959,5007}$+Hβ EWs in their paper, i.e., assuming a delayed star formation history (SFR $\propto te^{-t/\tau}$) and an SMC extinction curve (Pei 1992). This is to ensure the comparison with Endsley et al. (2021a) is done in the most fair

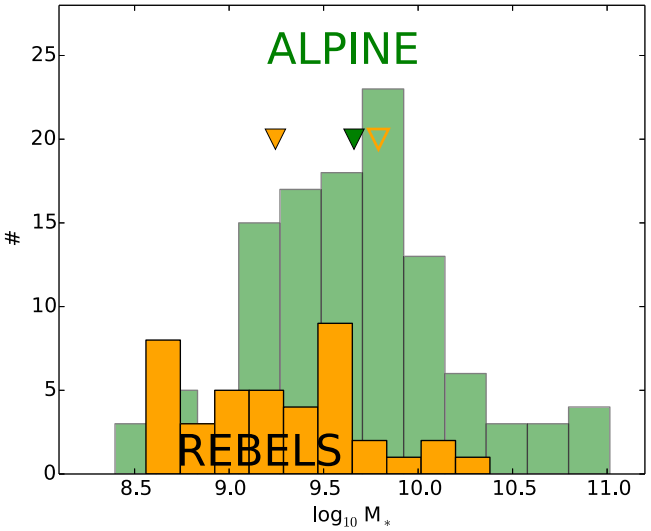

Figure 17. Distribution of stellar masses (orange histogram) inferred using BEAGLE for the 40 targets in the REBELS LP assuming a constant star formation history. For context, the green histogram shows the stellar mass distribution for $z = 4$–6 targets in the ALPINE program (Faisst et al. 2020). The median stellar masses inferred using BEAGLE and using PROSPECTOR (Leja et al. 2017), assuming constant and nonparametric star formation histories, respectively, are shown as downward-pointing filled and open orange triangles. Given the overall similarity of the two distributions and similar medians, the ALPINE program provides us with a convenient lower-redshift sample to characterize evolution in galaxies from $z > 6.5$ to $z = 4$–6. A similar presentation of the REBELS sample in redshift, UV luminosity, UV-continuum slope β, and the [O III]$_{4959,5007}$+Hβ EW is provided in Figure 18.

way possible. For completeness, we include the EWs derived both assuming a constant star formation history, as shown in Table 2, and assuming a delayed star formation history in Table 4. The median photometric redshift, UV luminosity, β, and [O III]$_{4959,5007}$+Hβ EW of the REBELS sources are 6.99, −22.2, −1.98, and 638 Å, respectively.

The median UV-continuum slope β is consistent with the mean β, i.e., -1.98 ± 0.07, for the Bowler et al. (2017) $z \sim 7$ sample. It is also consistent with the biweight mean $-1.75 \pm 0.18 \pm 0.13$ derived by Bouwens et al. (2014) in their highest-luminosity $z \sim 7$ bin.

Meanwhile, the median [O III]$_{4959,5007}$+Hβ EW is consistent with the median EW 759^{+112}_{-113}Åderived by Endsley et al. (2021a) at $z \sim 6.75$ using an analogous procedure. The similarity of the UV-continuum slope β and [O III]$_{4959,5007}$+Hβ EW distributions seen in REBELS to the $z \sim 7$ population suggest that the results derived from REBELS should be reasonably representative of the overall galaxy population at $z \sim 7$.

Table 4
Various Inferences of the [O III]$_{4959,5007}$+Hβ EWs for Sources in the REBELS Sample

REBELS IDs	$\log_{10}$ EW([O III]+Hβ)(Å)[a]	
	CSFH	Delayed SFH
REBELS-01	$2.90^{+0.28}_{-0.12}$	$2.97^{+0.20}_{-0.24}$
REBELS-02	$3.07^{+0.14}_{-0.16}$	$2.73^{+0.29}_{-0.36}$
REBELS-03	$3.05^{+0.33}_{-0.22}$	$2.78^{+0.36}_{-0.47}$
REBELS-04	$3.25^{+0.33}_{-0.31}$	$3.15^{+0.26}_{-0.29}$
REBELS-05	$3.12^{+0.30}_{-0.32}$	$3.02^{+0.30}_{-0.34}$
REBELS-06	$2.96^{+0.27}_{-0.18}$	$2.80^{+0.31}_{-0.27}$
REBELS-07	$3.18^{+0.33}_{-0.17}$	$2.82^{+0.42}_{-0.50}$
REBELS-08	$3.07^{+0.23}_{-0.22}$	$2.90^{+0.26}_{-0.35}$
REBELS-09	$3.77^{+0.05}_{-0.02}$	$1.39^{+1.03}_{-0.59}$
REBELS-10	$2.95^{+0.10}_{-0.09}$	$2.16^{+0.50}_{-0.64}$
REBELS-11	$3.08^{+0.21}_{-0.19}$	$2.74^{+0.36}_{-0.39}$
REBELS-12	$3.26^{+0.29}_{-0.25}$	$3.27^{+0.20}_{-0.25}$
REBELS-13	$2.98^{+0.13}_{-0.09}$	$2.35^{+0.37}_{-0.54}$
REBELS-14	$3.21^{+0.35}_{-0.20}$	$3.10^{+0.31}_{-0.44}$
REBELS-15	$3.73^{+0.10}_{-0.54}$	$3.64^{+0.22}_{-0.59}$
REBELS-16	$3.02^{+0.10}_{-0.10}$	$2.61^{+0.25}_{-0.55}$
REBELS-17	$3.04^{+0.21}_{-0.19}$	$2.74^{+0.41}_{-0.59}$
REBELS-18	$3.00^{+0.22}_{-0.17}$	$2.79^{+0.26}_{-0.25}$
REBELS-19	$3.11^{+0.21}_{-0.22}$	$2.82^{+0.33}_{-0.34}$
REBELS-20	$3.17^{+0.15}_{-0.11}$	$3.18^{+0.22}_{-0.47}$
REBELS-21	$2.84^{+0.28}_{-0.12}$	$2.39^{+0.58}_{-0.61}$
REBELS-22	$2.91^{+0.31}_{-0.14}$	$2.75^{+0.36}_{-0.47}$
REBELS-23	$3.03^{+0.19}_{-0.16}$	$2.97^{+0.21}_{-0.28}$
REBELS-24	$3.13^{+0.19}_{-0.21}$	$2.86^{+0.30}_{-0.36}$
REBELS-25	$2.79^{+0.21}_{-0.06}$	$2.53^{+0.29}_{-0.35}$
REBELS-26	$2.98^{+0.27}_{-0.21}$	$2.97^{+0.26}_{-0.29}$
REBELS-27	$2.89^{+0.27}_{-0.11}$	$2.57^{+0.34}_{-0.44}$
REBELS-28	$3.26^{+0.49}_{-0.20}$	$2.98^{+0.21}_{-0.27}$
REBELS-29	$2.90^{+0.12}_{-0.08}$	$2.20^{+0.40}_{-0.43}$
REBELS-30	$3.06^{+0.20}_{-0.13}$	$2.80^{+0.30}_{-0.33}$
REBELS-31	$3.05^{+0.06}_{-0.06}$	$2.55^{+0.26}_{-0.38}$
REBELS-32	$3.01^{+0.11}_{-0.11}$	$2.81^{+0.20}_{-0.21}$
REBELS-33	$2.90^{+0.27}_{-0.11}$	$2.72^{+0.23}_{-0.28}$
REBELS-34	$3.03^{+0.07}_{-0.06}$	$2.56^{+0.35}_{-0.35}$
REBELS-35	$3.18^{+0.30}_{-0.18}$	$2.89^{+0.35}_{-0.33}$
REBELS-36	$2.99^{+0.25}_{-0.16}$	$3.04^{+0.22}_{-0.28}$
REBELS-37	$3.25^{+0.32}_{-0.17}$	$3.05^{+0.18}_{-0.24}$
REBELS-38	$3.01^{+0.35}_{-0.25}$	$3.05^{+0.23}_{-0.33}$
REBELS-39	$3.58^{+0.17}_{-0.37}$	$3.52^{+0.15}_{-0.35}$
REBELS-40	$2.98^{+0.32}_{-0.20}$	$2.73^{+0.36}_{-0.40}$

Note.
[a] Derived using BEAGLE (M. Stefanon et al. 2022, in preparation).

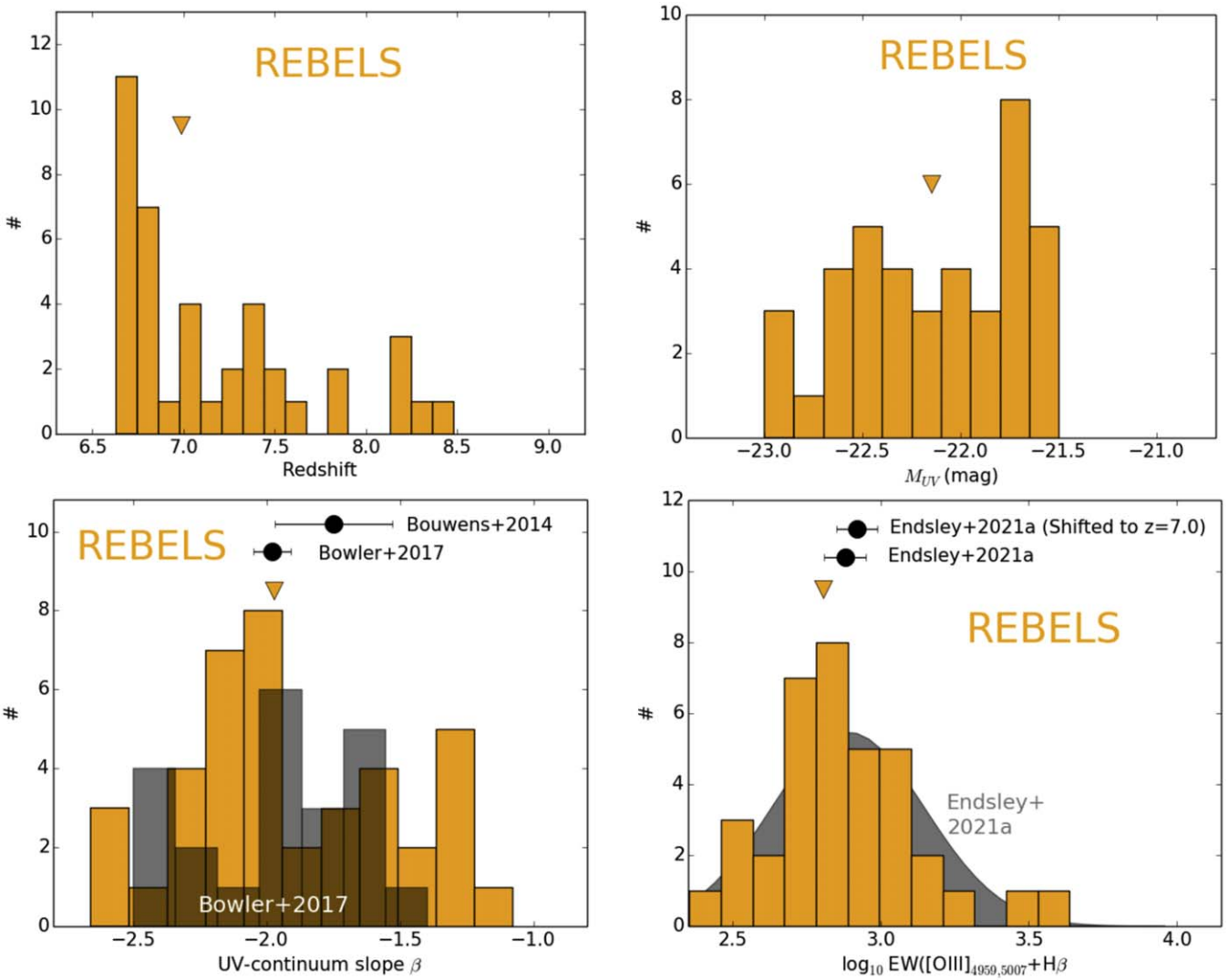

Figure 18. Distribution of the 40 REBELS targets in redshift (upper left), UV luminosity (upper right), UV-continuum slope β (lower left), and [O III]$_{4959,5007}$+Hβ EW (lower right). The shaded histogram shown in the lower left panel is the UV-continuum slope β distribution derived by Bowler et al. (2017) for a similar-luminosity sample of $z \sim 7$ galaxies identified over the COSMOS and UKIDSS/UDS regions, while the shaded region shown in the lower right region is the [O III]$_{4959,5007}$+Hβ EW distribution derived by Endsley et al. (2021a) at $z \sim 6.75$. The median photometric redshift and UV luminosity are 6.99 and −22.2 mag, respectively, and indicated by the orange downward-pointing triangles. The median UV-continuum slope β is −1.98 (indicated by the orange downward-pointing triangle) and is consistent with the mean β, i.e., -1.98 ± 0.07, for the Bowler et al. (2017) $z \sim 7$ sample as well as the biweight mean β, i.e., $-1.75 \pm 0.18 \pm 0.13$, derived by Bouwens et al. (2014) in their highest-luminosity $z \sim 7$ bin (black circle with 1σ uncertainties). The median [O III]$_{4959,5007}$+Hβ EW for targets in the REBELS program using a delayed star formation history is 638 Å(indicated by the orange downward-pointing triangle) and is consistent with the median EW 759^{+112}_{-113}Å (lower black circle with 1σ uncertainties) derived by Endsley et al. (2021a) at $z \sim 6.75$ using a similar fitting procedure, as well as an sSFR-evolution-corrected EW of 820^{+119}_{-120}Å(upper black circle with 1σ uncertainties) at $z \sim 6.99$. The similarity of the UV-continuum slopes β and the [O III]$_{4959,5007}$+$H\beta$ distribution to the population averages at $z \sim 7$ suggest that the results derived from REBELS should be reasonably representative of the general galaxy population at $z \sim 7$.

ORCID iDs

R. J. Bouwens https://orcid.org/0000-0002-4989-2471
R. Smit https://orcid.org/0000-0001-8034-7802
S. Schouws https://orcid.org/0000-0001-9746-0924
M. Stefanon https://orcid.org/0000-0001-7768-5309
R. Bowler https://orcid.org/0000-0003-3917-1678
H. Inami https://orcid.org/0000-0003-4268-0393
P. Oesch https://orcid.org/0000-0001-5851-6649
J. Hodge https://orcid.org/0000-0001-6586-8845
M. Aravena https://orcid.org/0000-0002-6290-3198
E. da Cunha https://orcid.org/0000-0001-9759-4797
P. Dayal https://orcid.org/0000-0001-8460-1564
A. Ferrara https://orcid.org/0000-0002-9400-7312
T. Nanayakkara https://orcid.org/0000-0003-2804-0648
P. van der Werf https://orcid.org/0000-0001-5434-5942
D. Riechers https://orcid.org/0000-0001-9585-1462

References

Aihara, H., Arimoto, N., Armstrong, R., et al. 2018a, PASJ, 70, S4
Aihara, H., Armstrong, R., Bickerton, S., et al. 2018b, PASJ, 70, S8
Anders, P., & Fritze-v. Alvensleben, U. 2003, A&A, 401, 1063
Arata, S., Yajima, H., Nagamine, K., et al. 2020, MNRAS, 498, 5541
Aravena, M., Boogaard, L., Gnzalez-Lpez, J., et al. 2020, ApJ, 901, 79
Arnouts, S., Cristiani, S., Moscardini, L., et al. 1999, MNRAS, 310, 540
Ashby, M. L. N., Caputi, K. I., Cowley, W., et al. 2018, ApJS, 237, 39
Bakx, T. J. L. C., Tamura, Y., Hashimoto, T., et al. 2020, MNRAS, 493, 4294
Bañados, E., Venemans, B. P., Mazzucchelli, C., et al. 2018, Natur, 553, 473
Behrens, C., Pallottini, A., Ferrara, A., et al. 2018, MNRAS, 477, 552
Behroozi, P. S., Wechsler, R. H., & Conroy, C. 2013, ApJ, 770, 57

Béthermin, M., Daddi, E., Magdis, G., et al. 2015, A&A, 573, A113
Bthermin, M., Fudamoto, Y., Ginolfi, M., et al. 2020, A&A, 643, A2
Bouwens, R. J., Illingworth, G. D., Oesch, P. A., et al. 2011, ApJ, 737, 90
Bouwens, R. J., Illingworth, G. D., Oesch, P. A., et al. 2014, ApJ, 793, 115
Bouwens, R. J., Illingworth, G. D., Oesch, P. A., et al. 2015, ApJ, 803, 34
Bouwens, R. J., Oesch, P. A., Labbé, I., et al. 2016, ApJ, 830, 67
Bouwens, R. J., Stefanon, M., Oesch, P. A., et al. 2019, ApJ, 880, 25
Bouwens, R., Gonzlez-Lpez, J., Aravena, M., et al. 2020, ApJ, 902, 112
Bouwens, R. J., Oesch, P. A., Stefanon, M., et al. 2021, ApJ, 162, 47
Bowler, R. A. A., Dunlop, J. S., McLure, R. J., et al. 2014, MNRAS, 440, 2810
Bowler, R. A. A., Dunlop, J. S., McLure, R. J., et al. 2015, MNRAS, 452, 1817
Bowler, R. A. A., Dunlop, J. S., McLure, R. J., et al. 2017, MNRAS, 466, 3612
Bowler, R. A. A., Bourne, N., Dunlop, J. S., et al. 2018, MNRAS, 481, 1631
Bowler, R. A. A., Jarvis, M. J., Dunlop, J. S., et al. 2020, MNRAS, 493, 2059
Bradač, M., Garcia-Appadoo, D., Huang, K.-H., et al. 2017, ApJL, 836, L2
Bradley, L. D., Trenti, M., Oesch, P. A., et al. 2012, ApJ, 760, 108
Brammer, G. B., van Dokkum, P. G., & Coppi, P. 2008, ApJ, 686, 1503
Bridge, J. S., Holwerda, B. W., Stefanon, M., et al. 2019, ApJ, 882, 42
Bromm, V., & Yoshida, N. 2011, ARA&A, 49, 373
Bruzual, G., & Charlot, S. 2003, MNRAS, 344, 1000
Burgasser, A. J. 2014, in Int. Workshop on Stellar Spectral Libraries ASI Conf. Ser. 11, ed. H. P. Singh, P. Prugniel, & I. Vauglin, 7
Calzetti, D., Armus, L., Bohlin, R. C., et al. 2000, ApJ, 533, 682
Capak, P. L., Carilli, C., Jones, G., et al. 2015, Natur, 522, 455
Caputi, K. I., Deshmukh, S., Ashby, M. L. N., et al. 2017, ApJ, 849, 45
Carniani, S., Maiolino, R., Pallottini, A., et al. 2017, A&A, 605, A42
Carniani, S., Maiolino, R., Smit, R., et al. 2018, ApJL, 854, L7
Carniani, S., Ferrara, A., Maiolino, R., et al. 2020, MNRAS, 499, 5136
Chabrier, G. 2003, PASP, 115, 763
Chevallard, J., & Charlot, S. 2016, MNRAS, 462, 1415
Coe, D., Zitrin, A., Carrasco, M., et al. 2013, ApJ, 762, 32
Coe, D., Salmon, B., Bradač, M., et al. 2019, ApJ, 884, 85
Cortes, P. C., Remijan, A., Biggs, A., et al. 2020, ALMA Technical Handbook, ALMADoc. 8.4, ver. 1.0, https://arc.iram.fr/documents/cycle8/ALMA_Cycle8_Technical_Handbook.pdf
Dayal, P., Dunlop, J. S., Maio, U., et al. 2013, MNRAS, 434, 1486
Dayal, P., & Ferrara, A. 2018, PhR, 780, 1
Dayal, P., Ferrara, A., Sommovigo, L., et al. 2022, MNRAS, 512, 989
Decarli, R., Walter, F., Venemans, B. P., et al. 2017, Natur, 545, 457
Decarli, R., Aravena, M., Boogaard, L., et al. 2020, ApJ, 902, 110
De Looze, I., Cormier, D., Lebouteiller, V., et al. 2014, A&A, 568, A62
Daz-Santos, T., Assef, R. J., Blain, A. W., et al. 2016, ApJL, 816, L6
Duncan, K., Conselice, C. J., Mundy, C., et al. 2019, ApJ, 876, 110
Dye, S., Warren, S. J., Hambly, N. C., et al. 2006, MNRAS, 372, 1227
Eldridge, J. J., Stanway, E. R., Xiao, L., et al. 2017, PASA, 34, e058
Ellis, R. S., McLure, R. J., Dunlop, J. S., et al. 2013, ApJL, 763, L7
Endsley, R., Stark, D. P., Chevallard, J., et al. 2021a, MNRAS, 500, 5229
Endsley, R., Stark, D. P., Charlot, S., et al. 2021b, MNRAS, 502, 6044
Endsley, R., Stark, D. P., Bouwens, R. J., et al. 2022, MNRAS, submitted, arXiv:2202.01219
Erben, T., Hildebrandt, H., Lerchster, M., et al. 2009, A&A, 493, 1197
Faisst, A. L., Schaerer, D., Lemaux, B. C., et al. 2020, ApJS, 247, 61
Ferland, G. J., Chatzikos, M., Guzmn, F., et al. 2017, RMxAA, 53, 385
Ferrara, A., Viti, S., & Ceccarelli, C. 2016, MNRAS, 463, L112
Ferrara, A., Sommovigo, L., Dayal, P., et al. 2022, MNRAS, 512, 58
Finkelstein, S. L., Ryan, R. E., Jr., Papovich, C., et al. 2015, ApJ, 810, 71
Förster Schreiber, N. M., Genzel, R., Bouché, N., et al. 2009, ApJ, 706, 1364
Fudamoto, Y., Oesch, P. A., Faisst, A., et al. 2020, A&A, 643, A4
Fudamoto, Y., Oesch, P. A., Schouws, S., et al. 2021, Natur, 597, 489
Fujimoto, S., Ouchi, M., Ferrara, A., et al. 2019, ApJ, 887, 107
Fuller, S., Lemaux, B. C., Bradač, M., et al. 2020, ApJ, 896, 156
Glazebrook, K., Schreiber, C., Labbé, I., et al. 2017, Natur, 544, 71
Gonzlez-Lpez, J., Novak, M., Decarli, R., et al. 2020, ApJ, 897, 91
Graziani, L., Schneider, R., Ginolfi, M., et al. 2020, MNRAS, 494, 1071
Grogin, N. A., Kocevski, D. D., Faber, S. M., et al. 2011, ApJS, 197, 35
Gruppioni, C., Bthermin, M., Loiacono, F., et al. 2020, A&A, 643, A8
Harikane, Y., Ouchi, M., Inoue, A. K., et al. 2020, ApJ, 896, 93
Hashimoto, T., Laporte, N., Mawatari, K., et al. 2018, Natur, 557, 392
Hashimoto, T., Inoue, A. K., Mawatari, K., et al. 2019, PASJ, 71, 71
Herrera-Camus, R., Frster Schreiber, N., Genzel, R., et al. 2021, A&A, 649, A31
Hildebrandt, H., Pielorz, J., Erben, T., et al. 2009, A&A, 498, 725
Hoag, A., Bradač, M., Trenti, M., et al. 2017, NatAs, 1, 0091
Hodge, J. A., & da Cunha, E. 2020, RSOS, 7, 200556
Holwerda, B., Bouwens, R., Trenti, M., et al. 2018, Spitzer Proposal, ID #14049
Hutchison, T. A., Papovich, C., Finkelstein, S. L., et al. 2019, ApJ, 879, 70
Ilbert, O., Arnouts, S., McCracken, H. J., et al. 2006, A&A, 457, 841
Inami, H., Algera, H. S. B., Schouws, S., et al. 2022, MNRAS, submitted (arXiv:2203.15136)
Inoue, A. K., Tamura, Y., Matsuo, H., et al. 2016, Sci, 352, 1559
Jarvis, M. J., Bonfield, D. G., Bruce, V. A., et al. 2013, MNRAS, 428, 1281
Jiang, L., Egami, E., Mechtley, M., et al. 2013, ApJ, 772, 99
Jiang, L., Kashikawa, N., Wang, S., et al. 2021, NatAs, 5, 256
Jones, G. C., Vergani, D., Romano, M., et al. 2021, MNRAS, 507, 3540
Jung, I., Finkelstein, S. L., Dickinson, M., et al. 2020, ApJ, 904, 144
Katz, H., Kimm, T., Sijacki, D., et al. 2017, MNRAS, 468, 4831
Kartaltepe, J., Casey, C. M., Bagley, M., et al. 2021, JWST Proposal Cycle 1, ID #1727
Koekemoer, A. M., Faber, S. M., Ferguson, H. C., et al. 2011, ApJS, 197, 36
Kohandel, M., Pallottini, A., Ferrara, A., et al. 2019, MNRAS, 487, 3007
Kohandel, M., Pallottini, A., Ferrara, A., et al. 2020, MNRAS, 499, 1250
Kotulla, R., Fritze, U., Weilbacher, P., et al. 2009, MNRAS, 396, 462
Knudsen, K. K., Watson, D., Frayer, D., et al. 2017, MNRAS, 466, 138
Labbé, I., Bouwens, R., Illingworth, G. D., et al. 2006, ApJL, 649, L67
Labb, I., Oesch, P. A., Bouwens, R. J., et al. 2013, ApJL, 777, L19
Labbé, I., Oesch, P. A., Illingworth, G. D., et al. 2015, ApJS, 221, 23
Labbé, I., Caputi, K., McLeod, D., et al. 2016, Spitzer Proposal, ID #13094
Lagache, G., Cousin, M., & Chatzikos, M. 2018, A&A, 609, A130
Laporte, N., Ellis, R. S., Boone, F., et al. 2017, ApJL, 837, L21
Laporte, N., Katz, H., Ellis, R. S., et al. 2019, MNRAS, 487, L81
Laporte, N., Meyer, R. A., Ellis, R. S., et al. 2021, MNRAS, 505, 3336
Larson, R. L., Finkelstein, S. L., Pirzkal, N., et al. 2018, ApJ, 858, 94
Lawrence, A., Warren, S. J., Almaini, O., et al. 2007, MNRAS, 379, 1599
Le Fevre, O., Bthermin, M., Faisst, A., et al. 2020, A&A, 643, A1
Leja, J., Johnson, B. D., Conroy, C., et al. 2017, ApJ, 837, 170
Madau, P. 1995, ApJ, 441, 18
Maiolino, R., Carniani, S., Fontana, A., et al. 2015, MNRAS, 452, 54
Mainali, R., Kollmeier, J. A., Stark, D. P., et al. 2017, ApJL, 836, L14
Mainali, R., Zitrin, A., Stark, D. P., et al. 2018, MNRAS, 479, 1180
Mancini, M., Schneider, R., Graziani, L., et al. 2015, MNRAS, 451, L70
Marrone, D. P., Spilker, J. S., Hayward, C. C., et al. 2018, Natur, 553, 51
Matthee, J., Sobral, D., Boone, F., et al. 2017, ApJ, 851, 145
Matthee, J., Sobral, D., Boogaard, L. A., et al. 2019, ApJ, 881, 124
Mauduit, J.-C., Lacy, M., Farrah, D., et al. 2012, PASP, 124, 714
McCracken, H. J., Milvang-Jensen, B., Dunlop, J., et al. 2012, A&A, 544, A156
McMullin, J. P., Waters, B., Schiebel, D., Young, W., & Golap, K. 2007, in ASP Conf. Ser. 376, Astronomical Data Analysis Software and Systems XVI, ed. R. A. Shaw, F. Hill, & D. J. Bell (San Francisco, CA: ASP), 127
Merlin, E., Fontana, A., Ferguson, H. C., et al. 2015, A&A, 582, A15
Michaowski, M. J. 2015, A&A, 577, A80
Morishita, T., Trenti, M., Stiavelli, M., et al. 2018, ApJ, 867, 150
Morishita, T., Stiavelli, M., Trenti, M., et al. 2020, ApJ, 904, 50
Novak, M., Smolčić, V., Delhaize, J., et al. 2017, A&A, 602, A5
Oesch, P. A., Bouwens, R. J., Illingworth, G. D., et al. 2014, ApJ, 786, 108
Oesch, P. A., Brammer, G., van Dokkum, P. G., et al. 2016, ApJ, 819, 129
Oesch, P. A., van Dokkum, P. G., Illingworth, G. D., et al. 2015, ApJL, 804, L30
Oke, J. B., & Gunn, J. E. 1983, ApJ, 266, 713
Olsen, K., Greve, T. R., Narayanan, D., et al. 2017, ApJ, 846, 105
Ono, Y., Ouchi, M., Mobasher, B., et al. 2012, ApJ, 744, 83
Ono, Y., Ouchi, M., Harikane, Y., et al. 2018, PASJ, 70, S10
Ota, K., Walter, F., Ohta, K., et al. 2014, ApJ, 792, 34
Ouchi, M., Ellis, R., Ono, Y., et al. 2013, ApJ, 778, 102
Pallottini, A., Ferrara, A., Gallerani, S., et al. 2017, MNRAS, 465, 2540
Pallottini, A., Ferrara, A., Decataldo, D., et al. 2019, MNRAS, 487, 1689
Pei, Y. C. 1992, ApJ, 395, 130
Pelliccia, D., Strait, V., Lemaux, B. C., et al. 2021, ApJL, 908, L30
Pentericci, L., Fontana, A., Vanzella, E., et al. 2011, ApJ, 743, 132
Pentericci, L., Carniani, S., Castellano, M., et al. 2016, ApJL, 829, L11
Pentericci, L., Vanzella, E., Castellano, M., et al. 2018, A&A, 619, A147
Popping, G., Somerville, R. S., & Galametz, M. 2017, MNRAS, 471, 3152
Postman, M., Coe, D., Bentez, N., et al. 2012, ApJS, 199, 25
Raiter, A., Schaerer, D., & Fosbury, R. A. E. 2010, A&A, 523, A64
Roberts-Borsani, G. W., Bouwens, R. J., Oesch, P. A., et al. 2016, ApJ, 823, 143
Roberts-Borsani, G. W., Ellis, R. S., & Laporte, N. 2020, MNRAS, 497, 3440
Roberts-Borsani, G., Morishita, T., Treu, T., et al. 2022, ApJ, 927, 236
Rybak, M., Calistro Rivera, G., Hodge, J. A., et al. 2019, ApJ, 876, 112
Salmon, B., Coe, D., Bradley, L., et al. 2020, ApJ, 889, 189
Sanders, D. B., Salvato, M., Aussel, H., et al. 2007, ApJS, 172, 86

Schaerer, D., & de Barros, S. 2009, A&A, 502, 423
Schaerer, D., Ginolfi, M., Bthermin, M., et al. 2020, A&A, 643, A3
Schenker, M. A., Stark, D. P., Ellis, R. S., et al. 2012, ApJ, 744, 179
Schenker, M. A., Ellis, R. S., Konidaris, N. P., et al. 2014, ApJ, 795, 20
Schmidt, K. B., Treu, T., Trenti, M., et al. 2014, ApJ, 786, 57
Schmidt, K. B., Huang, K.-H., Treu, T., et al. 2017, ApJ, 839, 17
Schouws, S., Stefanon, M., Bouwens, R. J., et al. 2022a, ApJ, 928, 31
Schouws, S., Bouwens, R. J., Smit, R., et al. 2022b, ApJ, in press (arXiv:2202.04080)
Schreiber, C., Elbaz, D., Pannella, M., et al. 2018, A&A, 609, A30
Scoville, N., Aussel, H., Brusa, M., et al. 2007, ApJS, 172, 1
Shibuya, T., Kashikawa, N., Ota, K., et al. 2012, ApJ, 752, 114
Smit, R., Bouwens, R. J., Labb, I., et al. 2014, ApJ, 784, 58
Smit, R., Bouwens, R. J., Franx, M., et al. 2015, ApJ, 801, 122
Smit, R., Bouwens, R. J., Carniani, S., et al. 2018, Natur, 553, 178
Sobral, D., Matthee, J., Darvish, B., et al. 2015, ApJ, 808, 139
Sommovigo, L., Ferrara, A., Carniani, S., et al. 2021, MNRAS, 503, 4878
Sommovigo, L., Ferrara, A., Pallottini, A., et al. 2020, MNRAS, 497, 956
Sommovigo, L., Ferrara, A., Pallottini, A., et al. 2022, MNRAS, in press
Song, M., Finkelstein, S. L., Livermore, R. C., et al. 2016, ApJ, 826, 113
Stark, D. P., Ellis, R. S., Chiu, K., et al. 2010, MNRAS, 408, 1628
Stark, D. P., Schenker, M. A., Ellis, R., et al. 2013, ApJ, 763, 129
Stark, D. P., Walth, G., Charlot, S., et al. 2015, MNRAS, 454, 1393
Stark, D. P., Ellis, R. S., Charlot, S., et al. 2017, MNRAS, 464, 469
Stefanon, M., Bouwens, R. J., Labb, I., et al. 2017a, ApJ, 843, 36
Stefanon, M., Labbé, I., Bouwens, R. J., et al. 2017b, ApJ, 851, 43
Stefanon, M., Labbé, I., Caputi, K., et al. 2018, Spitzer Proposal ID, #14045
Stefanon, M., Labbé, I., Bouwens, R. J., et al. 2019a, ApJ, 883, 99
Stefanon, M., & Bouwens, R. 2019b, Spitzer Proposal, ID #14305
Stefanon, M., Aravena, M., Bouwens, R., et al. 2021, JWST Proposal Cycle 1, ID #1626
Stefanon, M., Bouwens, R. J., Labbé, I., et al. 2022, ApJ, 927, 48
Steinhardt, C. L., Speagle, J. S., Capak, P., et al. 2014, ApJL, 791, L25
Speagle, J. S., Steinhardt, C. L., Capak, P. L., et al. 2014, ApJS, 214, 15
Strandet, M. L., Weiss, A., De Breuck, C., et al. 2017, ApJL, 842, L15
Sugahara, Y., Ouchi, M., Harikane, Y., et al. 2019, ApJ, 886, 29
Szalay, A. S., Connolly, A. J., & Szokoly, G. P. 1999, AJ, 117, 68
Talia, M., Cimatti, A., Giulietti, M., et al. 2021, ApJ, 909, 23
Tamura, Y., Mawatari, K., Hashimoto, T., et al. 2019, ApJ, 874, 27
Tanaka, M., Valentino, F., Toft, S., et al. 2019, ApJL, 885, L34
Taniguchi, Y., Ajiki, M., Nagao, T., et al. 2005, PASJ, 57, 165
Topping, M. W., Stark, D. P., Endsley, R., et al. 2022, MNRAS, submitted (arXiv:2203.07392)
Trenti, M., Bradley, L. D., Stiavelli, M., et al. 2011, ApJL, 727, L39
Vallini, L., Gallerani, S., Ferrara, A., et al. 2015, ApJ, 813, 36
Vallini, L., Ferrara, A., Pallottini, A., et al. 2017, MNRAS, 467, 1300
Vallini, L., Ferrara, A., Pallottini, A., et al. 2020, MNRAS, 495, L22
Vanzella, E., Pentericci, L., Fontana, A., et al. 2011, ApJL, 730, L35
Venemans, B. P., Neeleman, M., Walter, F., et al. 2019, ApJL, 874, L30
Venemans, B. P., Walter, F., Neeleman, M., et al. 2020, ApJ, 904, 130
Walter, F., Carilli, C., Neeleman, M., et al. 2020, ApJ, 902, 111
Warren, S., Lawrence, A., Almaini, O., et al. 2006, Msngr, 126, 7
Watson, D., Christensen, L., Knudsen, K. K., et al. 2015, Natur, 519, 327
Willott, C. J., Carilli, C. L., Wagg, J., et al. 2015, ApJ, 807, 180
Wise, J. H., Turk, M. J., Norman, M. L., et al. 2012, ApJ, 745, 50
Yan, H., Yan, L., Zamojski, M. A., et al. 2011, ApJL, 728, L22
Zheng, W., Postman, M., Zitrin, A., et al. 2012, Natur, 489, 406
Zitrin, A., Labb, I., Belli, S., et al. 2015, ApJL, 810, L12